July 2018

Reduced Models of Point Vortex Systems in Quasigeostrophic Fluid Dynamics

Jonathan Maack

Recommended Citation

Maack, Jonathan, "Reduced Models of Point Vortex Systems in Quasigeostrophic Fluid Dynamics" (2018). *Doctoral Dissertations*. 1258.
https://scholarworks.umass.edu/dissertations_2/1258

REDUCED MODELS OF POINT VORTEX SYSTEMS IN QUASIGEOSTROPHIC FLUID DYNAMICS

A Dissertation Presented

by

JONATHAN MAACK

Submitted to the Graduate School of the

University of Massachusetts Amherst in partial fulfillment

of the requirements for the degree of

DOCTOR OF PHILOSOPHY

May 2018

Mathematics and Statistics

REDUCED MODELS OF POINT VORTEX SYSTEMS IN QUASIGEOSTROPHIC FLUID DYNAMICS

A Dissertation Presented

By

JONATHAN MAACK

Approved as to style and content by:

Bruce Turkington, Chair

Markos Katsoulakis, Member

Qian-Yong Chen, Member

Stephen de Bruyn Kops, Member

Nathaniel Whitaker, Department Head

Mathematics and Statistics

DEDICATION

To my amazing wife Kristina. Thanks for the patience, love and support.

ACKNOWLEDGEMENTS

I would like to thank all of the following people:

The members of my committee for agreeing to read this work before they knew how long it would be. I appreciate your time and questions.

The various instructors I have had here at Umass from whom I have learned so much. Especially, Luc Rey-Bellet and Markos Katsoulakis who have encouraged my broad mathematical interests through numerous classes and discussions.

The Mathematics and Statistics Department staff who enable so much activity within the department. In particular Jacob Lagerstrom and Ilona Trousdale, who have patiently answered many questions I have asked when it was probably someone else's job to do so.

E.J. Rivet who instructed me in math through much of elementary school. You were the first person who showed me how fascinating and enjoyable math could be.

Bruce Turkington. Your patience, insight and encouragement were vital to the completion of this work. Through our conversations you have helped me to be a better writer, teacher and mathematician.

And finally my wife Kristina. You not only agreed to me leaving a stable job and income to follow me across the country but encouraged me to do it because you believed it would make me happy. Throughout my studies, you have continually surprised me with your patience when I am distracted by a math problem, with your understanding when I do not have time for a date because I want to study, and most recently, with the energy you have found to care for our newborn son so that I can finish my degree.

ABSTRACT

REDUCED MODELS OF POINT VORTEX SYSTEMS IN QUASIGEOSTROPHIC FLUID DYNAMICS

MAY 2018

JONATHAN MAACK, B.S., COLORADO SCHOOL OF MINES
M.S., COLORADO SCHOOL OF MINES
Ph.D., UNIVERSITY OF MASSACHUSETTS AMHERST

Directed by: Professor Bruce Turkington

We develop a nonequilibrium statistical mechanical description of the evolution of point vortex systems governed by either the Euler, single-layer quasigeostrophic or two-layer quasigeostrophic equations. Our approach is based on a recently proposed optimal closure procedure for deriving reduced models of Hamiltonian systems. In this theory the statistical evolution is kept within a parametric family of distributions based on the resolved variables chosen to describe the macrostate of the system. The approximate evolution is matched as closely as possible to the true evolution by minimizing the mean-squared residual in the Liouville equation, a metric which quantifies the information loss rate due to model reduction.

The point vortex approximation of the fluid dynamics allows the optimal closure, which is formulated on phase space, to be transferred to physical space resulting in an exact mean-field theory for the continuum limit. The near-equilibrium linearization of this theory is used to model the intrinsic relaxation rates for isolated coherent vorticity structures. The equilibration of initially disturbed vorticity fields is captured by a reduced model that has few resolved variables and no adjustable parameters.

For the Euler and single-layer quasigeostrophic equations, the theory is used to model the axisymmetrization of a deformed vorticity patch. In particular, the reduced model exhibits how the rate of symmetrization depends upon the energy and the Rossby deformation radius. For the two-layer equations the study focuses on the relaxation of baroclinic perturbations of stable barotropic structures and the transfer of available potential energy to kinetic energy. The model predicts the dependence of the barotropization rate on the energy and the internal Rossby deformation radius. Both axisymmetrization and barotropization are prominent features of the coherent vortex structures observed in direct numerical simulations of two-dimensional and quasigeostrophic turbulence. The reduced model is tested against the evolution of an ensemble of point vortex systems to validate its predictions. Therefore, the reduced model furnishes a mathematical theory of these fluid dynamical phenomena.

CONTENTS

APPENDICES

LIST OF TABLES

LIST OF FIGURES

CHAPTER 1

INTRODUCTION

Two-dimensional large Reynolds number turbulence theory changed with an important discovery by McWilliams. He noted that in long time simulations of the Euler equation as well as the single-layer and continuously stratified quasigeostrophic equations that large scale coherent vorticity structures emerged as the dominant dynamical phenomena [40, 39]. McWilliams observations were duplicated by Babiano et al. [3] and is still a topic of great interest [33, 50]. Prior to the observation of coherent structures, two-dimensional turbulence theory focused on the cascade theory of Kraichnan [32] and Batchelor [4]. It was argued that energy cascades toward the low Fourier modes while enstropy cascades toward high Fourier modes so that the energy and enstrophy scale with the wave number. However, these persistent vorticity patches were found to disrupt the cascade scalings ([33] and [50] discuss this and the interaction of the cascade and the coherent structures). Thus, the persistent vorticity patches became another important object of study in two-dimensional turbulence.

In particular, these coherent structures created an application of statistical mechanics to turbulence theory and attempts were made to predict the long time vorticity distributions of these coherent structures as equilibrium states. Onsager anticipated both the coherent structures and use of statistical mechanics when he first used the point vortex idealization in a statistical approach to understanding turbulence [44]. Apart from the attempt itself, perhaps the most important part of the paper was his argument for the existence of negative temperature states as a result of the bounded phase space of the point vortex system (see chapter 3 for the details of this argument). He further argued that these negative temperature states correspond to tightly clustered groups of point vortices to store excess energy. These are precisely those states that survive and dominate at long time and, hence, are the most interesting. Onsager's work was continued by Lundgren and Pointin and by Joyce and Montgomery. The former used kinetic methods on a collection of like signed vortices in an unbounded region [47] and different signed vortices in a bounded region [36] to derive a mean-field equation governing the most probable state. Joyce and Montgomery also obtained a mean-field equation for the most probable distribution of equal number of positive and negative vortices in a bounded region using a maximum entropy argument [42], where they specifically focused on the negative temperature regime. Since these results, much work has been done to rigorously support their conclusions [8, 9, 29].

The point vortex system was a natural starting ground for the equilibrium statistical mechanics of vorticity structures. It is an old approximation of the Euler equation having been formulated by Helmholtz and further studied by Kirchoff [43]. It has several problems including infinite self energy and failure to model vortex mergers [57]. In spite of these criticisms, it has remained a relevant technique even as a method of approximating fluid flow where it has evolved into the "vortex blob" methods as described in [16, 24]. All of these methods provably approximate the flow as governed by the Euler equation. That is, the point vortex and vortex blob methods can be shown to converge in an appropriate weak sense to the solution of the Euler equation [37, 16, 24]. Furthermore, as a basis for statistical mechanics, the point vortex idealization remains useful due to its similarity to classical mechanics—a point vortex resembles a molecule and the theory results in a probability distribution over real space. These reasons also position the point vortex system well as a mechanism for developing a nonequilibrium theory of fluids.

The goal of nonequilibrium statistical mechanics is to predict the evolution of certain desired quantities without explicitly computing the microscopic or fine scale dynamics. This form of model reduction is very ambitious and leads to the closure problem. In this problem, we seek to write equations for the evolution of some interesting quantities where the equations depend only upon those quantities. From another perspective, this problem is one of how to account for the interactions of the resolved quantities with the unresolved quantities, or those fine scales that we do not want to track, in the evolution of the resolved quantities.

The optimal closure theory advocated by Turkington in [55] is a systematic approach to building reduced equations for Hamiltonian systems without making use of any adjustable parameters. This method has been used to formulate theories for the two-dimensional Euler equation [58], the shell model [52] and the truncated Burgers equation [31, 51]. The optimal closure methodology departs from the traditional methods of nonequilibrium statistical mechanics. The key idea of this theory is to choose a parametric family of distributions and require the predicted evolution to remain within this family. The theory then introduces an information theoretic error, called the Liouville residual, which quantifies how this predicted evolution departs from the true evolution. This residual is based on the relative entropy and can be interpreted as the rate of information loss. The closed equations are derived by minimizing this residual over all paths through parameter space. Equivalently, the closure is achieved by taking the evolution within the parametric family that most closely follows the true evolution in an appropriate sense.

In this work, we use the point vortex idealization together with the optimal closure to form a nonequilibrium extension of the equilibrium mean-field equations for the Euler equation, the single-layer quasigeostrophic equation and the two-layer quasigeostrophic equation. This is done by using the point vortex idealization for the continuum equation, giving a finite dimensional Hamiltonian system. The optimal closure theory is then applied to this system. Then by taking the continuum limit, we reduce the Liouville residual to a residual upon the original continuum equation. As such, we use the point vortex approximation to transfer the optimal closure from phase space to real space. The result is a nonequilibrium mean-field theory for the Euler, single-layer quasigeostrophic and two-layer quasigeostrophic equations with no adjustable parameters.

For each equation, we will more thoroughly develop the theory using a near-equilibrium assumption. There are a couple of reasons for this. First, the minimization of the residual over a time path is a difficult problem requiring the solution of the Euler-Lagrange equation or the Hamilton-Jacobi equation. Reducing to the near-equilibrium regime gives us a more computationally tractable problem. Second, the computation of the mean-field trial densities for our nonequilibrium theory require solving a nonlinear partial differential equation subject to several constraints. When near an equilibrium solution, this nonlinear problem is replaced by a linear one. Finally, this assumption allows us to construct a modified resolved vector that necessarily respects the conservation of energy, angular impulse and vorticity. In turn, this modification further simplifies the necessary minimization problem as we do not have to externally impose the constraints on the system.

We then use our near-equilibrium theory to study two different problems. The first is to predict the symmetrization of a distorted vorticity patch. In [40], one of the dynamical processes present in the long time numerical simulations of the Euler and single-layer quasigeostrophic equations was that of axisymmetrization. When two coherent like-signed vortices become sufficiently close, they are stretched and strained away from the normal axisymmetric shape. This could be the result of merging or of the shearing flow from the other vortex. Once merging is complete or the two have drifted far enough apart, the vortices relax back to axisymmetric form. We seek to model this axisymmetrization process and predict its rate. Furthermore, for the Euler equation we predict how the rate of symmetrization depends on the energy of the system, and for the single-layer equation we predict how this rate depends on both the energy and the external Rossby deformation radius.

The second problem we investigate is that of the "barotropization" of vorticity structures in stratified fluids. Long time simulations of the continuously stratified quasigeostrophic equation revealed that the coherent vorticity patches tended to have a uniform vertical structure [39]. In the language of geophysical fluid dynamics, the isolated vorticity patches tended to be purely barotropic. This problem can be viewed as a three-dimensional analog of the symmetrization problem just described. The two-layer quasigeostrophic equation is a simple model of a stratified rotating fluid. As such, it provides a good testbed for studying the barotropization process. Using our two-layer closure, we model the relaxation to these purely barotropic states, and we also quantify the conversion of available potential energy into kinetic energy throughout this process. Finally, we predict how the barotropization rate and the available potential energy conversion rate depends on the energy of the system and the internal Rossby deformation radius.

While studying these two problems, we also investigate the range of validity of our reduced model. To do so, we compare the predicted evolution to direct numerical simulations of an ensemble of point vortex systems. In particular, we compare the magnitude of departure from equilibrium due to the asymmetric and baroclinic perturbations as well as the time scale to return to equilibrium. We also look at the classic relative error of the predicted and numerical evolutions.

The outlined tasks require a significant amount of background knowledge and we have sought to provide the necessary material. Chapter 2 provides the required background of the Euler equation and discusses the point vortex idealization as well as derives the resulting dynamical system. In chapter 3, we summarize the theory of equilbrium statistical mechanics for the point vortex system and derive the mean-field equation for an ensemble of like signed point vortices. Chapter 4 outlines the optimal closure theory for the nonequilibrium statistical mechanics of a general Hamiltonian system. Particular attention is paid to the near-equilibrium formulation. In chapter 5, we derive our nonequilibirum theory for the Euler equation. The first result is a general mean-field theory. We then specialize to the near-equilibrium regime. Chapter 6 applies the near-equilibrium theory to the symmetrization problem and predicts the symmetrization rate dependence on the energy of the system. Chapter 7 provides the necessary background material for the single-layer quasigeostrophic equation, including its derivation from the rotating shallow-water equations. We also describe the point vortex dynamics in this context. The chapter concludes with generalization of the equilibrium theory of point vortices to the single-layer equation. In chapter 8, we derive our nonequlibrium theory for the single-layer case. We then describe the results for the symmetrization problem and conclude with our prediction of the symmetrization rate dependence on the energy and external deformation radius. Chapter 9 derives the two-layer quasigeostrophic model. We discuss the barotropic and baroclinic modes and the division of energy according to the model before walking through the theory of baroclinic instability. This theory is one of the major developments of geophysical fluids and is fundamentally a mechanism for the transference of available potential energy into kinetic energy [60]. This motivates our interest in quantifying the energetics in our two-layer theory. Finally, the chapter concludes with the two-layer point vortex idealization and the corresponding equilibrium statistical theory. In chapter 10, we derive our two-layer nonequlibrium theory generally and then reduce to the near-equilibrium case. In this regime, we examine the rate at which available potential energy becomes kinetic energy as predicted by our theory. Finally, we conclude the chapter with our analysis of the barotropization problem and our predictions of the dependence of the barotropization rate and potential energy flow rate on the energy of the system and the internal deformation radius. Appendix A contains the technical justification of our mean-field approximation used to reduce the residual on the Liouville equation to a residual on the associated continuum equations. Appendix B describes the various numerical methods we have used in this work.

Throughout this work, we have chosen to emphasize application and interpretation over mathematical rigor. This is especially true of chapters 7-10 where we discuss the more physically relevant single-layer and two-layer quasigeostrophic equations. This choice was motivated largely by a desire to make the work more approachable.

CHAPTER 2

POINT VORTEX DYNAMICS

The evolution of an incompressible ideal fluid under the Euler equations is quite complex, even in two dimensions where the evolution is completely determined by the vorticity. One of the earliest approximations of the evolution of the vorticity was the point vortex idealization where the vorticity is assumed to be concentrated at a finite number of points in what amounts to the turbulence equivalent of the point mass. The problem of the evolution of point vortices was investigated by Helmholtz in 1858 and Kirchoff in 1883 [43] and has remained important into the present as it is the foundation of the vortex blob methods for numerically simulating the Euler equation [16, 24]. The key idea of the approximation is that it reduces the Euler equation into a system of $2N$ ordinary differential equations for N point vortices. In doing so, the Euler equation moves from an infinite dimensional Hamiltonian system to a finite dimensional Hamiltonian system.

In this section, we provide the necessary background for the Euler equations in two-dimensions and the point vortex idealization. We do not provide a derivation of the Euler equation or proofs that the stated quantities are conserved as we assume the reader is familiar with them. We refer the reader to [15, 37] for a mathematical treatment of these or [48, 60] for a more physically oriented perspective. The point vortex idealization, on the other hand, is discussed more thoroughly as the concept of the point vortex is critical to all that follows. This approximation is also discussed in [37]. The basics and more of the modern research can be found in [43].

2.1 Euler Equations

The incompressible Euler equation on the plane is given by

$$\partial_t \mathbf{u} + (\mathbf{u} \cdot \nabla)\mathbf{u} = -\nabla p \tag{2.1a}$$

$$\nabla \cdot \mathbf{u} = 0 \tag{2.1b}$$

where $\mathbf{u}$ is the velocity field and p is the pressure field. We also require that $|\mathbf{u}| \to 0$ as $|\mathbf{x}| \to \infty$. This is equivalent to taking the potential flow to be zero.

The incompressibility condition (2.1b) allows us to define the stream function ψ such that

$$\mathbf{u} = \nabla^{\perp}\psi \tag{2.2}$$

where

$$\nabla^{\perp} = (\partial_y, -\partial_x). \tag{2.3}$$

Now we define the vorticity $\zeta = \nabla \times \mathbf{u}$. Because the flow is two-dimensional, only the z-component of ζ does not vanish so that we can regard it as a scalar quantity. Combining the vorticity definition and (2.2), we arrive at the relation

$$-\Delta\psi = \zeta.$$

Taking the curl of (2.1a), using (2.1b) and (2.2) together with the above relation, we arrive at the stream function-vorticity formulation of the incompressible two-dimensional Euler equation on the plane

$$\partial_t \zeta + [\zeta, \psi] = 0, \tag{2.4a}$$

$$-\Delta\psi = \zeta, \tag{2.4b}$$

where

$$[A, B] = \frac{\partial A}{\partial x}\frac{\partial B}{\partial y} - \frac{\partial A}{\partial y}\frac{\partial B}{\partial x}.$$

Equation (2.4a) tells us that the material derivative of the vorticity field is always zero. Taking a Lagrangian viewpoint, we see that the vorticity of a fluid particle is constant in time. This insight drives the point vortex idealization we discuss later.

It can be shown that this equation conserves the total vorticity

$$\Gamma = \int_{\mathbb{R}^2} \zeta \, d\mathbf{x}, \tag{2.5}$$

and the energy

$$E = \frac{1}{2} \int_{\mathbb{R}^2} \psi \cdot \zeta \, d\mathbf{x}. \tag{2.6}$$

Furthermore, the translational and rotational symmetries of the domain give us three more invariants: the center of vorticity

$$\mathbf{B} = \int_{\mathbb{R}^2} \mathbf{x} \cdot \zeta \, d\mathbf{x}, \tag{2.7}$$

and the angular impulse

$$L^2 = \int_{\mathbb{R}^2} |\mathbf{x} - \mathbf{B}|^2 \zeta \, d\mathbf{x}. \tag{2.8}$$

Since we are considering the problem in the entire $\mathbb{R}^2$-plane, we may always translate the vorticity distribution so that the origin is the center of vorticity (that is, $\mathbf{B} = \mathbf{0}$). This allows us to simplify the expression for the angular impulse and, more importantly, ignore the center of vorticity conservation in the statistical mechanics calculations later.

These are not the only conserved quantities of the 2D Euler equation. Any quantity of the form

$$\int_{\mathbb{R}^2} f(\zeta) d\mathbf{x}$$

is conserved provided f is sufficiently smooth. This is called the generalized enstropy. The most notable such quantity is the enstrophy (hence the name) which we get by taking $f(\zeta) = \frac{1}{2}\zeta^2$.

2.2 Point Vortex Idealization

Now we assume that the initial vorticity distribution is sharply concentrated at N points:

$$\zeta^N(\mathbf{x},0) = \sum_{i=1}^{N} \gamma_i \delta_{\mathbf{x}_i}(\mathbf{x}) \tag{2.9}$$

where γ_i is the vorticity at the point $\mathbf{x}_i$. We call the isolated vorticity concentration at $\mathbf{x}_i$ a point vortex and ζ^N a point vortex distribution. As previously discussed, (2.4a) implies that the vorticity γ_i of the fluid parcel located at $\mathbf{x}_i$ is constant in time. Therefore, the vorticity distribution at time t is given by

$$\zeta^N(\mathbf{x},t) = \sum_{i=1}^{N} \gamma_i \delta_{\mathbf{x}_i(t)}(\mathbf{x}) \tag{2.10}$$

where $\mathbf{x}_i(t) = (x_i(t), y_i(t))$ is the position of the i^{th} point vortex at time t. Furthermore, the quantity

$$\Gamma = \sum_{i=1}^{N} \gamma_i \tag{2.11}$$

(called the total circulation or total vorticity) is a constant of the dynamics. So we see that the flow is completely determined by the paths of the fluid particles with the vorticity.

Our goal now is to find a dynamical system that describes the paths $\mathbf{x}(t)$ which we do using the stream function. The Green's function for (2.4b) is

$$G(\mathbf{x},\mathbf{x}') = -\frac{1}{2\pi}\log|\mathbf{x}-\mathbf{x}'|.$$

Therefore, the stream function at time t corresponding to the vorticity distribution (2.10) is given by

$$\begin{aligned}\psi^N(\mathbf{x},t) &= -\frac{1}{2\pi}\int_{\mathbb{R}^2} \log|\mathbf{x}-\mathbf{x}'|\zeta_N(\mathbf{x}',t)\,d\mathbf{x}' \\ &= -\frac{1}{2\pi}\sum_{i=1}^{N} \gamma_i \log|\mathbf{x}-\mathbf{x}_i(t)|. \end{aligned} \tag{2.12}$$

Using the definition of the stream function (2.2), the velocity field is

$$\mathbf{u}(\mathbf{x}, t) = -\frac{1}{2\pi} \sum_{i=1}^{N} \gamma_i \left(\frac{y - y_i(t)}{|\mathbf{x} - \mathbf{x}_i(t)|^2}, -\frac{x - x_i(t)}{|\mathbf{x} - \mathbf{x}_i(t)|^2} \right). \tag{2.13}$$

This formulation gives an infinite velocity at the position of any point vortex. However, this is only due to the self advection of the point vortex. Physically, we expect a lone point vortex in the plane to remain stationary–that is, we expect a point vortex to have no effect on itself. It follows that we may neglect the self-flow term (for a mathematical justification see [37] chapter 4). Dropping this term and using the fact that

$$\frac{d}{dt}\mathbf{x}_i(t) = \mathbf{u}(\mathbf{x}_i, t),$$

we arrive at the system of $2N$ ordinary differential equations

$$\dot{x}_i = -\frac{1}{2\pi} \sum_{j \neq i} \gamma_j \frac{y_i - y_j}{r_{ij}^2}, \qquad \dot{y}_i = \frac{1}{2\pi} \sum_{j \neq i} \gamma_j \frac{x_i - x_j}{r_{ij}^2}, \qquad i = 1, \ldots, N, \tag{2.14}$$

where $\dot{x} = dx/dt$ and $r_{ij}^2 = (x_i - x_j)^2 + (y_i - y_j)^2 = |\mathbf{x}_i - \mathbf{x}_j|^2$.

This system can be written as a canonical Hamiltonian system with the conjugate variables $q_i = \sqrt{\gamma_i} x_i$ and $p_i = \sqrt{\gamma_i} y_i$ and the Hamiltonian

$$H^N(\mathbf{x}_1, \ldots, \mathbf{x}_N) = -\frac{1}{4\pi} \sum_{i=1}^{N} \sum_{i \neq j} \gamma_i \gamma_j \log |\mathbf{x}_i - \mathbf{x}_j|. \tag{2.15}$$

Since H^N is time invariant, it is a conserved quantity of the motion. The translational and rotational symmetries also result in the three conserved quantities

$$\mathbf{B} = \sum_i \gamma_i \mathbf{x}_i, \tag{2.16}$$

$$L_N^2 = \sum_i \gamma_i |\mathbf{x}_i - \mathbf{B}|^2. \tag{2.17}$$

The five quantities (2.11), (2.15), (2.16) and (2.17) are the point vortex counterparts of (2.5), (2.6), (2.7) and (2.8). They result immediately from the Euler equation when plugging in the point vortex distribution (2.10). In the case of the Hamiltonian, we must remove the infinite terms arising from the singularity of the log at the origin. Physically, this is again removing the self-interaction terms.

It can be shown that by using the quantities (2.16) and (2.17), the system (2.14) is integrable for $N \leq 3$ (see [43] chapter 2). For large N, the system is (generally) chaotic.

The question arises whether or not the point vortex idealization can be used to approximated solutions of the Euler equation. There is significant literature on this question: [37] provides a basic discussion. The short answer is that the point vortex approximation will converge in the weak sense of convergence of measures but to prove the convergence one must introduce a smoothing parameter into the Green's function. The value of this smoothing parameter depends on N and goes to zero very slowly. As this contributes directly to the error of the method, the pure vortex method converges rather slowly.

A better approximation is achieved by using vortex "blobs". Mathematically, these are point vortices that have been smoothed to remove the logarithmic singularity at its location. Physically, they can be thought of as a small, intense vorticity patch with nonzero width. The idea of this is linked to the proof of the convergence result discussed above–by smoothing out the point vortices, the convergence rate of the method is increased. The fundamental problem is the large velocities that occur when two vortices are close together. These are removed when the point vortices are exchanged for vortex blobs. See [16, 24] for details on these methods.

The slow convergence rate of the point vortex method is one of the limitations of this model. It has physical problems as well. The most obvious of these is the infinite self energy of a point vortex. This is a general problem even when the point vortex is in a finite domain. Since the kinetic energy is given by

$$KE = \frac{1}{2}\int_D |\mathbf{u}|^2 d\mathbf{x},$$

in the case of a point vortex (at the origin)

$$KE \propto \int_D \frac{1}{r^2} d\mathbf{x}$$

which is not integrable. This is actually the convergence problem again as it is the direct result of the logarithmic singularity of the stream function at the location of a point vortex.

The point vortex model also completely fails to model the process of vortex merger. Numerical studies of the Euler equations have revealed that when two patches of vorticity merge they collapse together and shed a small fraction of the total vorticity which is lost [40, 48]. Given the strength of a point vortex is conserved, the point vortex idealization cannot possibly model this phenomena.

The final problem is that the point vortex system does not preserve the conservation of the generalized enstrophies. In particular, the enstrophy itself is not conserved (indeed, the enstrophy does not even defined in the point vortex case). Since much of the theory of two dimensional turbulence has to do with energy cascading to large scales and while the enstrophy cascades to small scales [15, 48], this is a particularly large problem.

CHAPTER 3

EQUILIBRIUM STATISTICAL MECHANICS OF POINT VORTEX SYSTEMS

Equilibrium statistical mechanics methods are an attempt to model and understand coherent vorticity patches. Combining the point vortex idealization with statistical mechanics was one of the first attempts. It was first considered by Onsager [44] and the first major results came from Montgomergy and Joyce [42] and Pointin and Lundgren [47, 36]. As discussed last chapter, there are several limitations of the point vortex model—infinite self energy, failure to conserve generalized enstrophies and failure to model vortex merger.

Despite these failings, the point vortex formulation makes a useful model. The most attractive aspect is its resemblance to classical statistical mechanics—we can think of a point vortex much like a particle and the resulting equilibrium formulation is in real space. For these we reason, we pursue the point vortex model. The following discussion gives the basic equilibrium statistical mechanics theory of point vortices. These results may also be found in [37] and [43].

3.1 Derivation of Mean-Field Equations

The main result of equilibrium statistical mechanic theory is a meanfield equation for the single point probability distribution ρ or, equivalently, for $\zeta = \Gamma\rho$. We focus on the case of like signed vortices in the plane. In this case, the angular impulse constraint acts to confine the point vortices to a region so that a coherent structure can form. This is also the reason for requiring the point vortices to be like signed: two equal strength point vortices of opposite sign can pair up in such a way as to advect each other off to infinity while satisfying the angular impulse constraint. This behavior precludes the type of coherent structure we are interested in.

3.1.1 Microcanonical Distribution

Consider a number N of identical point vortices in the plane with total vorticity $\Gamma = 1$. The interactions are given by the Hamiltonian (2.15) (and move according to system (2.14)) where $\gamma_i = \gamma = 1/N$ is constant. Assume that the value of the Hamiltonian is E and the system has angular momentum L^2. Recall that we have already fixed the center of vorticity at the origin. We further assume that any point in phase space $\Lambda_N = \mathbb{R}^{2N}$ is equally probable and define the classical microcanonical distribution

$$\frac{1}{\Omega(E, L^2)}\delta(H^N - E)\delta(L_N^2 - L^2)d\mathbf{x}_1 \ldots d\mathbf{x}_N, \tag{3.1}$$

where $\Omega(E, L^2)$ is the normalizing constant

$$\Omega(E, L^2) = \int_{\Lambda_N} \delta(H^N - E)\delta(L_N^2 - L^2)d\mathbf{x}_1 \ldots d\mathbf{x}_N. \tag{3.2}$$

We make no effort to prove this. We simply assume it to be true. This is a standard practice in statistical mechanics as actually proving a system is ergodic is usually quite difficult.

We seek the most probable distribution in the limit $N \to \infty$ and $\gamma \to 0$ where $\Gamma = \gamma N$ remains constant. To this end, we introduce the entropy defined by

$$S(E, L^2) = \log \Omega(E, L^2). \tag{3.3}$$

We expect the most probable distribution to maximize the entropy.

It is usual at this point to also define the canonical Gibbs distribution

$$\frac{1}{Z}\exp\{-\beta H^N - \alpha|\mathbf{x}|^2\}d\mathbf{x}_1 \ldots d\mathbf{x}_N, \tag{3.4}$$

where the normalization constant Z is called the partition function and given by

$$Z = \int_{\mathbb{R}^2} \exp\{-\beta H^N - \alpha|\mathbf{x}|^2\}.$$

The Gibbs distribution fixes the temperature by fixing the coefficient β where as the microcanonical distribution fixes the energy. (The way we have written it here, the Gibbs distribution also fixes the constant α. This is somewhat unusual as the angular impulse constraint is almost always treated microcanonically.)

Many of the calculation are significantly easier using the Gibbs distribution (as opposed to the microcanonical distribution) and in classical statistical mechanics the two ensembles are equivalent in standard thermodynamic limits. However, in the point vortex case, the equivalence of ensembles does not hold [57]. It is inconvenient that this range of nonequivalence occurs in the negative temperature regime where the states of most interest reside. For this simple reason, we will use the microcanonical distribution in what follows.

3.1.2 Asymptotic Expression for the Entropy

In order to maximize the entropy, we first need an expression for the entropy of a particular distribution and in the light of our limit

$$N \to \infty, \quad \gamma \to 0, \quad \Gamma \text{ constant},$$

we only need an asymptotic expression for the entropy. To determine this expression, fix a disc of radius η and say that the vortices are confined to this disc which we denote A. We partition this disc into M regions of equal area. Call these regions $B_1, \ldots, B_M$ (where the i^{th} region has area $|B_i| = |B| = \frac{\pi\eta^2}{M}$). In the following, we assume that $N >> M >> 1$.

Now further assume that the positions of the point vortices are N independent samples from some distribution. Let n_i denote the number of vortices in region B_i. From combinatorics we know that there are

$$\frac{N!}{n_1!n_2!\ldots n_M!}$$

ways to arrange N objects into M bins so that the probability of observing a given configuration is

$$W = \left(\frac{N!}{n_1!n_2!\dots n_M!}\right)|B_1|^{n_1}|B_2|^{n_2}\dots|B_M|^{n_M} = \left(\frac{N!}{n_1!n_2!\dots n_M!}\right)|B|^N$$

where we have used $\sum_i n_i = N$ and that all the region have equal area [15]. Using Stirling's formula, we have

$$W \sim \frac{N^N}{n_1^{n_1}n_2^{n_2}\dots n_M^{n_M}}|B|^N = \prod_{i=1}^{M}\left(\frac{N\cdot|B_i|}{n_i}\right)^{n_i}$$

where $\sim$ means asymptotically equivalent. Since W also gives the volume of phase space [15], we have $S \sim \log W$. Taking the logarithm of the above yields

$$S \sim -\sum_{i=1}^{M} n_i \log\left(\frac{n_i}{N|B_i|}\right) = -N\sum_{i=1}^{M}\frac{n_i}{N|B_i|}\log\left(\frac{n_i}{N|B_i|}\right)|B_i|.$$

Now, if our system is drawn from the distribution ρ, we expect that

$$\rho(\mathbf{y}_i) \approx \frac{n_i}{N|B_i|}.$$

where $\mathbf{y}_i$ is some point in B_i. Using this in the above expression, we have

$$S \sim -N\sum_{i=1}^{M}\rho(\mathbf{y}_i)\log\rho(\mathbf{y}_i)|B_i|$$

In the limit of $N \to \infty$, $M \to \infty$ with $N >> M$, we recognize the right hand side as a Riemann sum and conclude that the entropy for a distribution is given by

$$-\int_A \rho(\mathbf{x})\log\rho(\mathbf{x})d\mathbf{x}.$$

Since η is arbitrary, it follows that the entropy over the entire plane of a distribution is given by

$$-\int_{\mathbb{R}^2}\rho(\mathbf{x})\log\rho(\mathbf{x})d\mathbf{x}.$$

It follows that maximizing the entropy S is equivalent to maximizing this integral.

Therefore, the probability density describing the most probable macrostate with given energy E and angular impulse L^2 satisfies the variational principle

$$\text{minimize} \int_{\mathbb{R}^2} \rho(\mathbf{x}) \log \rho(\mathbf{x}) d\mathbf{x} \quad \text{subject to} \tag{3.5a}$$

$$\frac{\Gamma}{2} \int_{\mathbb{R}^2} \psi(\mathbf{x}) \rho(\mathbf{x}) d\mathbf{x} = E, \tag{3.5b}$$

$$\Gamma \int_{\mathbb{R}^2} |\mathbf{x}|^2 \rho(\mathbf{x}) d\mathbf{x} = L^2, \tag{3.5c}$$

$$\int_{\mathbb{R}^2} \rho(\mathbf{x}) d\mathbf{x} = 1, \tag{3.5d}$$

where ψ solves

$$-\Delta\psi = \zeta = \Gamma\rho.$$

Note that there is actually a fourth constraint that must be satisfied: The total vorticity constraint given by

$$\int_{\mathbb{R}^2} \zeta(\mathbf{x}) d\mathbf{x} = \Gamma.$$

However, since $\zeta = \Gamma\rho$, it is obvious that this is equivalent to the constraint (3.5d). In fact, from here we assume that $\Gamma = 1$ so that we have $\zeta = \rho$.

Here we have given an outline of the proof. It is possible to make these arguments mathematically rigorous through the use of the theory of large deviations—particularly Sanov's Theorem [57]. In doing so, one must show that the Hamiltonian given by (2.15) converges to the continuum energy (2.6) as $N \to \infty$. This turns out to be a little delicate since one must deal with the infinite self energy of a point vortex.

3.1.3 Solution of Variational Problem

To complete our derivation of the meanfield equations, we need to solve the above variational problem. Calculus of variations tells us that to solve the constrained optimization problem (3.5), we solve the unconstrained optimization problem

$$\text{minimize} \int_{\mathbb{R}^2} \rho(\mathbf{x}) \log \rho(\mathbf{x}) + \frac{\beta}{2} \psi(\mathbf{x}) \rho(\mathbf{x}) + \alpha |\mathbf{x}|^2 \rho(\mathbf{x}) + \mu \rho(\mathbf{x}) \, d\mathbf{x}, \tag{3.6}$$

where we have introduced the Lagrange multipliers β, α and μ. The Euler-Lagrange equation for this is

$$\log\rho + 1 + \beta\psi + \alpha|\mathbf{x}|^2 + \mu = 0.$$

After solving for ρ (and redefining μ), we get the nonlinear system

$$\rho = \exp\{-\beta\psi - \alpha|\mathbf{x}|^2 - \mu\}, \tag{3.7a}$$

$$\rho = -\Delta\psi, \tag{3.7b}$$

where β, α and μ are constants such that constraints (3.5b), (3.5c) and (3.5d) are satisfied. The system (3.7) describes the most probable distribution. Here we have used a maximum entropy argument to derive these mean-field equations. In [43], a derivation of these same equations is given using kinetic arugments.

Comparing (3.7a) to the canonical Gibbs distribution, we see that μ is the log of the partition function and so is given by

$$\mu = \log\int_{\mathbb{R}^2} \exp\{-\beta\psi - \alpha|\mathbf{x}|^2\}d\mathbf{x}$$

Furthermore, β is the "inverse temperature" and satisfies

$$\beta = \frac{\partial S}{\partial E}.$$

However, unlike standard statistical mechanics, there is no reason to suppose that β takes only positive values. Indeed, in the case of the point vortex system in a bounded domain, Onsager argued for the existence of negative temperature states (that is, negative values of β). We recount that argument here as presented in [37, 43].

Consider N point vortices confined to the area D. We assume that there is no translational or radial symmetries so that the Hamiltonian is the only invariant. Define

$$\Theta(E) = \int_{D^N} \chi(H < E)d\mathbf{x}_1 \ldots d\mathbf{x}_N \tag{3.8}$$

where $\chi(H < E)$ denotes the characteristic function of the set of arrangements for which $H < E$. Then

$$\begin{aligned}\Theta(E) &= \int_{\mathbb{R}} \int_{D^N} \chi(E' < E)\delta(H - E')d\mathbf{x}_1 \dots d\mathbf{x}_N dE' \\ &= \int_{-\infty}^{E} \Omega(E')dE'\end{aligned}$$

It follows that

$$\Omega(E) = \Theta'(E)$$

which in turn implies

$$\beta = \frac{d}{dE} \log \Omega = \frac{1}{\Omega}\Omega' = \frac{\Theta''}{\Theta'}$$

We also know from the definition of Θ that Θ is an increasing function and has the limiting behaviors $\Theta \to 0$ as $E \to -\infty$ and $\Theta \to |D|^N$ as $E \to \infty$. Therefore, there must exist a point E_c where Θ changes concavity, that is, where $\Theta''(E_c) = 0$. At this energy, $\Omega = \Theta'$ attains its maximum and for $E > E_c$ we have

$$\beta = \frac{\Theta''}{\Theta'} < 0$$

so that we expect to have negative temperature states.

From this argument, we also see that the existence of negative temperature states is the result of the bounded phase space. For the point vortex system in the plane, the angular impulse constraint enforces a bounded phase space as argued above so we expect to see negative temperature states in this case as well.

Since Onsager first made this argument, the existence of negative β states has been proven [43] and the nature of the states has made them an important part of two-dimensional turbulence theory (as we shall see later).

3.2 Solutions of the Mean-Field Equations

We saw that the most probable distribution gives rise to a set of nonlinear mean-field equations. As these are meant to describe coherent vorticity structures, it is worth exploring the solutions and whether they give us the desired behavior. If we want to find the actual vorticity distribution we need to solve the system. In this section, we first describe and categorize the solutions of the mean-field equations (3.7) before moving on to a special case that can be explicitly solved.

3.2.1 Behavior of Solutions

Our first step is to fix the space scale by fixing the angular impulse at any value we desire, say $L^2 = 2$. Having done this, the system (3.7) results in a family of coherent, radially symmetric vorticity distributions ζ depending on a single parameter–the value of the energy [43]. We first discuss the qualitative aspects of the distribution with $\beta = 0$. This allows us to break up the range of energy values.

For $\beta = 0$, the system (3.7) decouples and ζ is given by a bivariate Gaussian distribution with zero mean and covariance matrix

$$\begin{pmatrix} L^2/2 & 0 \\ 0 & L^2/2 \end{pmatrix}$$

We fixed $L^2 = 2$ so that the covariance matrix is the identity matrix. In this case we may also write the stream function in closed form (see subsection 3.2.2). From this, we may calculate the energy corresponding to the case $\beta = 0$ simply by computing

$$E_g = \int_{\mathbb{R}^2} \psi \cdot \zeta \, d\mathbf{x}.$$

Numerical approximation of this integral gave $E_g \approx -0.03219$. For $E < E_g$ (and $\beta > 0$), the distribution flattens near the center and decays to zero at infinity [43]. In a bounded domain, the vorticity congregates near the boundary [57]. Generally, this is not studied since the Euler equations are poor approximations of fluid flow near a boundary (due to phenomena like boundary layers).

For $E > E_g$ (and $\beta < 0$), the distribution concentrates toward the center and decays at infinity. It is this concentration that makes this regime of interest as it resembles the coherent structures observed in direct numerical simulations of the Euler equation and quasigeostrophic equation [40, 39]. Considering the vorticity as a function of the radial variable r, for large r we have

$$\zeta \sim C \exp\left\{-\left(1+\frac{\beta}{8\pi}\right)\frac{r^2}{L^2}\right\}\left(\frac{r}{L}\right)^{\beta/2\pi}$$

where $L = \sqrt{L^2}$ [43]. Because Γ is finite, we must have $\beta > -8\pi$.

3.2.2 Solution at "Infinite Temperature"

In order to get an explicit formula for the stream function in the $\beta = 0$ case, first note we may write the vorticity distribution as

$$\rho = \frac{1}{\pi L^2}\exp(-r^2/L^2)$$

where $r^2 = x^2 + y^2$. In this case ψ satisfies

$$-\Delta\psi = \frac{1}{\pi L^2}\exp(-r^2/L^2).$$

Since the stream function ψ must itself be radially symmetric, this reduces to the ordinary differential equation

$$\psi''(r) + \frac{1}{r}\psi'(r) = -\frac{1}{\pi L^2}e^{-r^2/L^2}.$$

We define $\phi(r) = \psi'(r)$ and solve the resulting first order linear equation to get

$$\phi(r) = \frac{1}{2\pi r}(e^{-r^2/L^2} - 1)$$

where we have chosen the constant so that $\phi(r)$ is finite in the limit $r \to 0$. Using the fact that

$$\psi(\mathbf{x}) = \int_{\mathbb{R}^2} \log|\mathbf{x}' - \mathbf{x}|\zeta(\mathbf{x}')d\mathbf{x}'$$

we can compute

$$\psi(0) = -\frac{1}{2\pi}\int_{\mathbb{R}^2} \log|\mathbf{x}'|\zeta(\mathbf{x}')d\mathbf{x}' = \gamma_e - \frac{\log L^2}{4\pi}$$

where γ_e is the Euler-Masheroni constant. Using this, we can now write

$$\psi(r) = \gamma_e - \frac{\log L^2}{4\pi} + \int_0^r \phi(s) ds$$

which is fairly easily evaluated numerically.

3.3 Computing Equilibrium States

In general, to compute the solutions of the system (3.7), one must resort to numerics. Even in the $\beta = 0$ case, we still need numerics to compute the stream function. The Whitaker-Turkington algorithm is a particularly useful method for computing both ζ and ψ as well as the coefficients β, α and μ. It is described generally in [59] and [63]. Here we outline the algorithm for our application.

The basic idea of the algorithm is to break the problem into two parts: For a given ζ and ψ, find the appropriate β, α and μ so that the angular impulse constraint (3.5c), the probability constraint (3.5d) and a modified version of the energy constraint (3.5b) are satisfied. Then use these parameters to update ζ and ψ using (3.7). We repeat this process until the iterates have sufficiently converged.

The energy constraint is modified by linearizing around the current vorticity distribution, call it ζ_n. The linearized constraint is

$$H_n + \int_{\mathbb{R}^2} \psi_n(\zeta - \zeta_n) d\mathbf{x} = E$$

where ψ_n is the stream function corresponding to ζ_n and

$$H_n = \frac{1}{2} \int_{\mathbb{R}^2} \psi_n \zeta_n d\mathbf{x}.$$

With this modified constraint in hand, we now have the following algorithm: For a given

ψ_n, find β, α and μ such that

$$\begin{aligned}\int_{\mathbb{R}^2} \psi_n \exp\{-\beta\psi_n - \alpha|\mathbf{x}|^2 - \mu\} d\mathbf{x} &= E + H_n,\\ \int_{\mathbb{R}^2} |\mathbf{x}|^2 \exp\{-\beta\psi_n - \alpha|\mathbf{x}|^2 - \mu\} d\mathbf{x} &= L^2,\\ \int_{\mathbb{R}^2} \exp\{-\beta\psi_n - \alpha|\mathbf{x}|^2 - \mu\} d\mathbf{x} &= 1.\end{aligned}$$

This can be done with any root finding algorithm. Call the solutions of this problem β_n, α_n and μ_n.

We now form ζ_{n+1} as suggested by (3.7a). That is, we set

$$\zeta_{n+1} = \exp\{-\beta_n\psi_n - \alpha_n|\mathbf{x}|^2 - \mu_n\}$$

From ζ_{n+1}, we find ψ_{n+1} by solving

$$-\Delta\psi_{n+1} = \zeta_{n+1}.$$

This requires a Poisson solver for the plane. Having ζ_{n+1} and ψ_{n+1} in hand, we return to the root finding problem.

This iterative process is repeated until some appropriate convergence criterion is met. We required that

$$\frac{|H_{n+1} - E_0|}{|E_0|} < 10^{-10} \quad \text{and} \quad \frac{\max\limits_{\mathbf{x}\in\mathbb{R}^2}|\zeta_{n+1} - \zeta_n|}{\max\limits_{\mathbf{x}\in\mathbb{R}^2}|\zeta_n|} < 10^{-10}.$$

Despite (or perhaps because of) the simplistic structure, the algorithm is extremely robust. It can be shown that the algorithm will converge to any equilibrium state with $\beta \leq 0$ and any initial guess ζ_0 with $H_0 \geq E$ and angular impulse L^2 and total vorticity Γ [59]. In practice, we have found the algorithm to be globally convergent. For a discussion of our root finder and Poisson solver, see Appendix B.

CHAPTER 4

OPTIMAL CLOSURE THEORY

Equilibrium statistical mechanics is clean and elegant and is one of the more profound accomplishments of mathematical physics. Perhaps its only failing is that it predicts only the final state of a system after a long time and says nothing of how the system gets to that state. This is the purpose of nonequilibrium statistical mechanics—to predict the time evolution of some, usually chosen, bulk statistical quantities. While the equilibrium theory has found a cohesive framework with the theory of Gibbs measures [54], there is currently no equivalent unifying construct for nonequilibrium statistical mechanics. It is a patchwork of ad hoc approximations and assumptions. To some extent this is unavoidable as the evolution inevitably depends on the choice of the macroscopic quantities; however, some form of consistent methodology is highly desirable.

The following discussion gives the general theory of the optimal closure as described in [55] as well as [30]. The optimal closure theory departs from the standard methodologies of nonequilibrium statistical mechanics. It seeks to establish a systematic method for deriving evolution equations for a chosen set of observables by applying a statistical model reduction procedure determined by the underlying microdynamics. The fundamental idea is to choose a parametric family of distributions and force the evolution to remain in this family. Then we quantify the failure of this evolution to follow the true evolution with an information theoretic residual. We achieve a set of reduced equations by minimizing this residual over the entire time path of the evolution. The resulting equations are completely determined and there are no adjustable parameters.

In the following chapter, we will apply the general optimal closure to the point vortex idealization of the Euler equation and ultimately derive a nonequilibrium statistical theory that extends the equilibrium theory described in the previous chapter. In this mean-field context, we will find that the optimal closure results in an information theoretic residual on the Euler equation itself that quantifies the failure of our chosen parametric vorticity distribution to follow the true distribution. A unique path for the macroscopic evolution is determined by minimizing this residual. Again, these evolution equations are determined completely and uniquely by the optimal closure theory without resorting to adjustable parameters.

In what follows, it is assumed that the reader is familiar with the theory of Hamiltonian systems. Both [43] and [54] have brief summaries of the theory.

4.1 Liouville Equation and the Closure Problem

Consider a Hamiltonian system with canonical positions $\mathbf{q} = (q_1, \ldots, q_N)$ and canonical momenta $\mathbf{p} = (p_1, \ldots, p_N)$ and Hamiltonian H. We denote phase space by Λ_N and a point in phase space by $\mathbf{z} = (\mathbf{q}, \mathbf{p})$. The system evolves according to the equations

$$\dot{q}_i = \frac{\partial H}{\partial p_i}, \qquad \dot{p}_i = -\frac{\partial H}{\partial q_i}, \qquad i = 1, \ldots, N \tag{4.1}$$

where $\dot{x} = \frac{dx}{dt}$.

For this system, we are interested in predicting the evolution of m observables $\mathbf{A}(\mathbf{z}) = (A_1(\mathbf{z}), A_2(\mathbf{z}), \ldots, A_m(\mathbf{z}))$ where (most of the time) $m << N$. These are called the resolved variables. For any observable F, Hamiltonian theory tells us that

$$\frac{dF}{dt} = \{F, H\}$$

where $\{F, H\}$ denotes the Poisson bracket

$$\{F, H\} = \sum_{i=1}^{N} \frac{\partial F}{\partial q_i}\frac{\partial H}{\partial p_i} - \frac{\partial F}{\partial p_i}\frac{\partial F}{\partial q_i}.$$

Obviously, computing this for our resolved variables $\mathbf{A}$ requires (except in special circumstances) the exact integration of the system (4.1). For large N, this can be quite computationally expensive. As a result, we turn to a statistical description of the evolution of our resolved variables. Because Hamiltonian systems for large N are almost always chaotic, we may assume some sort of ergodicity and therefore expect that a statistical description will be a good approximation of the actual evolution.

Say we have a density $\rho(\mathbf{z}, t)$ which gives the probability that the system is in state $\mathbf{z}$ at time t. The evolution of this probability density on phase space, is given by the Liouville equation [54]

$$\partial_t \rho + \{\rho, H\} = 0. \tag{4.2}$$

It is convenient here to introduce the differential operators

$$T = \partial_t, \qquad L = \{\cdot, H\}$$

In this notation, the Liouville equation is given by

$$(T + L)\rho = 0$$

and we may formally write solutions of (4.2) as

$$\rho(\cdot, t) = e^{-(t-t_0)L} \rho(\cdot, t_0).$$

The Liouville equation is equivalently stated in the following way: for any time independent observable $F(\mathbf{z})$, the time evolution of the mean is given by

$$\frac{d}{dt} \langle F | \rho \rangle = \langle \{F, H\} | \rho \rangle \tag{4.3}$$

where $\langle F|\rho\rangle$ denotes the expectation of F with respect to the density ρ and is given by

$$\langle F | \rho \rangle = \int_{\Lambda_N} F(\mathbf{z}) \rho(\mathbf{z}, t) d\mathbf{z}.$$

To see this equivalence, we compute

$$
\begin{aligned}
\frac{d}{dt}\langle F|\rho\rangle &= \frac{d}{dt}\int_{\Lambda_N} F(\mathbf{z})\rho(\mathbf{z},t)d\mathbf{z} \\
&= \int_{\Lambda_N} F(\mathbf{z})\partial_t\rho(\mathbf{z},t)d\mathbf{z}.
\end{aligned}
$$

Then upon using the Liouville equation and the integration by parts identity

$$
\int_{\Lambda_N} A\{B,C\}d\mathbf{z} = -\int_{\Lambda_N} \{A,C\}Bd\mathbf{z},
$$

we find that

$$
\begin{aligned}
\frac{d}{dt}\langle F|\rho\rangle &= -\int_{\Lambda_N} F\left\{\rho,H\right\}d\mathbf{z} \\
&= \int_{\Lambda_N} \left\{F,H\right\}\rho d\mathbf{z}
\end{aligned}
$$

as desired.

The obvious way to compute the time evolution of the resolved vector is to compute the evolution of the density ρ using (4.2) and taking the appropriate average. However, it is extremely expensive to compute the evolution of ρ under the Liouville equation. Furthermore, assuming all we care about is the evolution of our mean resolved variables, this carries much more information forward then is required.

This suggests our goal should be the following: Write a system of differential equations for the time evolution of the mean resolved variables $\mathbf{a} = \langle A|\rho\rangle$ in terms of only these resolved variables. That is, we seek equations of the form

$$
\frac{d\mathbf{a}}{dt} = \mathbf{f}(\mathbf{a},t). \tag{4.4}
$$

This is, of course, the closure problem. It is in general quite difficult.

4.2 Liouville Residual

A standard approach to this is kinetic theory [64] in which the microscopic dynamics are used to construct a hierarchy of reduced distribution functions where the single point distribution is dependent on the two point distribution and so on. (An example of this method is discussed in slightly more detail in the introductory remarks of the next chapter.) This hierarchy in full is equivalent to the Liouville equation and so closure may only be achieved with some additional assumption. This assumption must be justified for each separate application.

We will achieve closure in a wholly new manner. Our first step is to impose a constraint upon the evolution of the density. Instead of the exact evolution $\rho(\mathbf{z}, t)$, we force the evolution to remain within a parametric family of distributions $\tilde{\rho}(\mathbf{z}, \lambda)$ where $\lambda = (\lambda_1, \lambda_2, \ldots, \lambda_m)$. We call this family of distributions the trial density. In this light, our approach resembles galerkin spectral or finite element methods where the solution of a differential equation is constrained to lay within a family by truncation of an infinite series. Of course, unlike these numerical methods, there is no guarantee that the true evolution may be recovered in some suitable infinite limit.

We choose the distribution family so that $\mathbf{A}$ is a sufficient statistic for the parameter vector λ [11, 61]. This means that for any sample, the statistic $\mathbf{A}$ contains all the information for the parameter λ. We further assume that the family is regular so that the score variables

$$\mathbf{U}(\lambda) = \frac{\partial \log \tilde{\rho}}{\partial \lambda}$$

are defined and that the Fisher information matrix

$$C(\lambda) = \left\langle U(\lambda) U(\lambda)^T | \tilde{\rho} \right\rangle$$

is nonsingular [11, 61]. These assumptions guarantee that there is a one-to-one correspondence between the mean resolved vector $\mathbf{a}$ and the parameter vector λ.

We now want to choose a path $\lambda(t)$ through parameter space so that $\langle \mathbf{A} | \tilde{\rho}(\lambda(t)) \rangle$ approximates $\langle \mathbf{A} | \rho(t) \rangle$. To get the best approximation, we want to match the true evolution as closely as possible. That is we want to minimize the distance between the true distribution $\rho(\mathbf{z}, t)$ and the approximate distribution $\tilde{\rho}(\mathbf{z}, t)$ is some suitable sense. A natural choice for a distance measure here is provided by the relative entropy or Kullback-Leibler divergence [17] which is given by

$$D_{KL}(\rho||\tilde{\rho}) = \int_{\Lambda_N} \rho \log \frac{\rho}{\tilde{\rho}} d\mathbf{z}. \tag{4.5}$$

This is not a true distance in the sense that it is not a metric, however, it is nonnegative and zero if and only if $\rho = \tilde{\rho}$. In statistics, the relative entropy arises as the expectation of the likelihood ratio and can be interpreted as a measure of the inefficiency of assuming the distribution $\tilde{\rho}$ when the true distribution is ρ.

As given, the computation of the relative entropy requires the true density ρ. We get around this difficulty in the following way: Assume that at some moment of time t the true density ρ and the trial density $\tilde{\rho}$ agree and consider the true evolution and trial density evolution through some small time Δt. The true evolution follows the Liouville equation and is given by

$$\rho(\cdot, t + \Delta t) = e^{-\Delta t L} \rho(\cdot, t). \tag{4.6}$$

whereas the trial density evolution is given by

$$\tilde{\rho}(\cdot, t + \Delta t) = e^{\Delta t T} \rho(\cdot, t). \tag{4.7}$$

The relative entropy between these two at time $t + \Delta t$ is given by

$$D_{KL}(\rho||\tilde{\rho}) = \int_{\Lambda_N} e^{-\Delta t L} \rho \cdot (\log e^{-\Delta t L} \rho - \log e^{\Delta t T} \rho) d\mathbf{z}$$

Using the fact that any function of ρ is also a solution of the Liouville equation we have

$$D_{KL}(\rho||\tilde{\rho}) = \int_{\Lambda_N} e^{-\Delta t L} \rho \cdot (e^{-\Delta t L} - e^{\Delta t T}) \log \rho d\mathbf{z}$$

Then since L is an anti-Hermitian operator, we find that

$$D_{KL}(\rho||\tilde{\rho}) = \left\langle e^{\Delta t L} (e^{-\Delta t L} - e^{\Delta t T}) \log \rho | \rho \right\rangle = \left\langle (I - e^{\Delta t (T+L)}) \log \rho | \rho \right\rangle$$

If we compute the Taylor expansion of the operator $e^{\Delta t(T+L)}$ we have

$$e^{\Delta t(T+L)} = I + \Delta t(T+L) + \frac{\Delta t^2}{2}(T+L)^2 + O(\Delta t^3) \tag{4.8}$$

so that

$$\begin{aligned} D_{KL}(\rho||\tilde{\rho}) &= \left\langle (I - e^{\Delta t(T+L)}) \log \rho | \rho \right\rangle \\ &= -\left\langle \left(\Delta t(T+L) + \frac{\Delta t^2}{2}(T+L)^2 \right) \log \rho | \rho \right\rangle + O(\Delta t^3). \end{aligned} \tag{4.9}$$

This motivates the definition of the Liouville residual:

$$R = (\partial_t + L) \log \tilde{\rho}. \tag{4.10}$$

From the definition, we see that the true distribution ρ has zero residual because it satisfies the Liouville equation. For a general distribution, this is nonzero so that it measures the lack of fit of the true evolution. This is even more apparent since the definition implies

$$R = \frac{1}{\tilde{\rho}}(\partial_t + L)\tilde{\rho}. \tag{4.11}$$

In this perspective, we can view the Liouville residual as a normalized lack of fit of the true dynamics.

We now note several additional properties of R. First, consider a time-dependent observable $F = F(\mathbf{z}, t)$. Then using (4.11) and the fact that

$$\int_{\Lambda_N} F \cdot L\rho \, d\mathbf{z} = -\int_{\Lambda_N} LF \cdot \rho \, d\mathbf{z},$$

we get

$$\begin{aligned}\frac{d}{dt}\langle F|\tilde{\rho}\rangle &= \langle \partial_t F|\tilde{\rho}\rangle + \int_{\Lambda_N} F\cdot \partial_t\tilde{\rho}\, d\mathbf{z}\\ &= \langle \partial_t F|\tilde{\rho}\rangle + \int_{\Lambda_N} F\cdot(-L\tilde{\rho}+\tilde{\rho}R)d\mathbf{z}\\ &= \langle \partial_t F|\tilde{\rho}\rangle + \langle LF|\tilde{\rho}\rangle + \langle FR|\tilde{\rho}\rangle\end{aligned}$$

Therefore, we have

$$\frac{d}{dt}\langle F|\tilde{\rho}\rangle - \langle LF|\tilde{\rho}\rangle = \langle \partial_t F + FR|\tilde{\rho}\rangle\,. \tag{4.12}$$

If F is time independent and we compare (4.12) to (4.3), we see that the extra term is the covariance of F and R with respect to the trial density $\tilde{\rho}$. We may interpret this term as quantifying the failure of the evolution of F under $\tilde{\rho}$ to follow the Liouville equation.

Second, taking $F = 1$ in (4.12) gives us

$$\langle R|\tilde{\rho}\rangle = 0. \tag{4.13}$$

Similarly, taking $F = R$ in (4.12) gives us

$$\langle(\partial_t + L)R|\tilde{\rho}\rangle = -\left\langle R^2|\tilde{\rho}\right\rangle. \tag{4.14}$$

Using (4.10), (4.13) and (4.14) in (4.9) results in

$$\begin{aligned}D_{KL}(\rho||\tilde{\rho}) &= -\Delta t\,\langle R|\tilde{\rho}\rangle + \frac{\Delta t^2}{2}\left\langle R^2|\tilde{\rho}\right\rangle + O(\Delta t^3)\\ &= \frac{\Delta t^2}{2}\left\langle R^2|\tilde{\rho}\right\rangle + O(\Delta t^3).\end{aligned} \tag{4.15}$$

This tells us that for a small time step Δt, the error in assuming $\tilde{\rho}(t+\Delta t)$ instead of $\rho(t+\Delta t)$ is determined to leading order by the variance of the Liouville residual with respect to the trial density.

The procedure used to derive the Liouville residual is analogous to the computation of the local truncation error of a numerical method. However, instead of expanding the absolute error and looking at the leading order term, we have expanded the relative entropy.

What results is an information theoretic version of local truncation error. In this light, the Liouville residual measures the information lost by forcing the evolution to remain a member of the family of trial densities.

4.3 Closure

Having forced the evolution to remain in the parametrized family $\tilde{\rho}$ and found a suitable measure of the lack of fit in the Liouville residual, we now look to form our closed equations.

The above discussion of the Liouville residual suggests that we select the path $\lambda(t)$ through the parameterized family $\tilde{\rho}$ which minimizes the quantity

$$\int_0^\tau \left\langle R^2 | \tilde{\rho}(\lambda(t)) \right\rangle dt$$

where τ is some chosen end time.

In order to solve this problem, we first introduce the Lagrangian

$$\mathcal{L}(\lambda, \dot{\lambda}) = \frac{1}{2} \left\langle R^2 | \tilde{\rho}(\lambda) \right\rangle \tag{4.16}$$

where $\dot{\lambda} = d\lambda/dt$. Note that the only time dependence of $\tilde{\rho}$ (and therefore of R) is through the parameter path $\lambda(t)$. Therefore we can consider $\mathcal{L}$ to be a function of λ and $\dot{\lambda}$ only.

Before looking to solve the minimization problem, it is helpful to decompose the Lagrangian into resolved and unresolved components. Using the operator

$$P_\lambda F = \left\langle F \mathbf{U}(\lambda)^T | \tilde{\rho} \right\rangle C(\lambda)^{-1} \mathbf{U}(\lambda),$$

which projects any element F of the Hilbert space $L^2(\Lambda_N, \tilde{\rho}(\lambda))$ onto the subspace spanned by the score functions, and the complementary projection operator $Q_\lambda = I - P_\lambda$, we can write the Lagrangian as

$$\mathcal{L}(\lambda, \dot{\lambda}) = \frac{1}{2} \left\langle (P_\lambda R)^2 | \tilde{\rho}(\lambda) \right\rangle + \frac{1}{2} \left\langle (Q_\lambda R)^2 | \tilde{\rho}(\lambda) \right\rangle, \tag{4.17}$$

where the first term represents the resolved components and the second the unresolved.

Using the fact that

$$\begin{aligned}\langle [L\log\tilde{\rho}(\lambda)]\mathbf{U}(\lambda)|\tilde{\rho}(\lambda)\rangle &= \int_{\Lambda_N} \{\tilde{\rho}(\lambda), H\}\,\mathbf{U}(\lambda)d\mathbf{z}\\ &= -\int_{\Lambda_N} \{\mathbf{U}(\lambda), H\}\,\tilde{\rho}(\lambda)d\mathbf{z}\\ &= -\langle L\mathbf{U}(\lambda)|\tilde{\rho}(\lambda)\rangle\,,\end{aligned}$$

we find that

$$P_\lambda R = [\dot{\lambda} - C(\lambda)^{-1}f(\lambda)]^T\mathbf{U}(\lambda), \tag{4.18}$$

$$Q_\lambda R = Q_\lambda L\log\tilde{\rho}(\lambda). \tag{4.19}$$

Plugging these two into (4.17), the Lagrangian becomes

$$\mathcal{L}(\lambda,\dot{\lambda}) = \frac{1}{2}[\dot{\lambda} - C(\lambda)^{-1}f(\lambda)]^T C(\lambda)[\dot{\lambda} - C(\lambda)^{-1}f(\lambda)] + d(\lambda) \tag{4.20}$$

where

$$d(\lambda) = \frac{1}{2}\left\langle (Q_\lambda L\log\tilde{\rho}(\lambda))^2|\tilde{\rho}(\lambda)\right\rangle.$$

Tracing the terms in (4.20) back to (4.17) tells us that the first term is the projection of the Liouville residual onto the score functions and are, therefore, related to the resolved vector **A**. The second term, $d(\lambda)$, arose from the projection of the Liouville residual by the operator Q onto the unresolved variables. Hence, (4.20) is the decomposition of the Liouville residual into resolved and unresolved components.

We now want to solve the variational problem

$$\min_{\lambda(0)=\lambda_0}\int_0^\tau \mathcal{L}(\lambda,\dot{\lambda})dt.$$

At this point, several theories provide us with possible paths to a solution. In particular, we could use the calculus of variations and the Euler-Lagrange equations or the Pontryagin maximum principle [34]. However, these methods lead to less (obviously) useful results than the theory of dynamic programming. This theory is based on the Hamilton-Jacobi-

Bellman equation [21, 34]. Both calculus of variations and the maximum principle provide the same theoretical result but, through the use of Hamiliton-Jacobi theory, we will be able to write our closed equations explicitly and obtain a particularly elegant interpretation of the resulting equations.

Our first step down the dynamic programming path is to define the value function

$$v(\lambda_0, \tau) = \min_{\lambda(0)=\lambda_0} \int_0^\tau \mathcal{L}(\lambda, \dot{\lambda}) dt, \tag{4.21}$$

where we have fixed the initial value $\lambda(0) = \lambda_0$ and the time horizon τ and the endpoint $\lambda(\tau)$ is free to take any value. However, for the general value function u, defined to be the minimal cost for some cost functional, the Hamilton-Jacobi-Bellman equation is given by

$$\frac{\partial u}{\partial t} + \mathcal{H}\left(\lambda, \frac{\partial u}{\partial \lambda}\right) = 0, \qquad t \in (0, \tau), \tag{4.22}$$

$$u(\tau) = g(\lambda), \tag{4.23}$$

where $\mathcal{H}$ is the Legendre transform of the kernel of the cost functional. This is a terminal-value problem, that is, the value function is specified at the end time.

To fit our problem into dynamic programming theory, we need to reformulate our cost functional to change the initial value problem to a terminal value problem. In order to do this, we introduce the reversed time $s = \tau - t$. Written in this variable, our value function now has the form

$$v(\lambda_0, \tau) = \min_{\lambda(\tau)=\lambda_0} \int_0^\tau \mathcal{L}\left(\lambda, -\frac{d\lambda}{ds}\right) ds$$

which, according to dynamic programming theory, solves the time-dependent Hamilton-Jacobi equation

$$\frac{\partial v}{\partial s} - \mathcal{H}\left(\lambda, -\frac{\partial v}{\partial \lambda}\right) = 0, \qquad s \in (0, \tau), \tag{4.24}$$

$$v(\lambda, \tau) = 0, \tag{4.25}$$

where $\mathcal{H}$ is again the Legendre transform of $\mathcal{L}$ given by

$$\mathcal{H}(\lambda, \nu) = -\frac{d\lambda}{ds}^T \nu - \mathcal{L}\left(\lambda, -\frac{d\lambda}{ds}\right). \tag{4.26}$$

We have introduced a negative on the first term to account for the time reversal. The conjugate variable ν is given by the partial derivative of $\mathcal{L}$ with respect to $d\lambda/ds$. We can compute this explicitly from (4.20) after adjusting for the time reversal to find that

$$\nu = -C(\lambda)\frac{d\lambda}{ds} - f(\lambda), \tag{4.27}$$

where $C(\lambda)$ is the Fisher information matrix and

$$f(\lambda) = \langle L\mathbf{U}(\lambda)|\tilde{\rho}\rangle .$$

Reformulating this in the forward time variable $t = \tau - s$, we find that the value function must satisfy the Hamilton-Jacobi equation

$$\frac{\partial v}{\partial t} + \mathcal{H}\left(\lambda, -\frac{\partial v}{\partial \lambda}\right) = 0, \qquad t \in (0, \tau) \tag{4.28a}$$

$$v(\lambda, 0) = 0 \tag{4.28b}$$

and the conjugate variable ν is given by

$$\nu = C(\lambda)\dot{\lambda} - f(\lambda). \tag{4.29}$$

Furthermore, we know that the optimal path $\hat{\nu}(t)$ along an optimal path $\hat{\lambda}(t)$ is given by the relation

$$\hat{\nu} = -\frac{\partial v}{\partial \lambda}(\hat{\lambda}, t). \tag{4.30}$$

Combining (4.29) and (4.30) gives us the desired closure

$$C(\hat{\lambda})\frac{d\hat{\lambda}}{dt} = f(\hat{\lambda}) - \frac{\partial v}{\partial \lambda}(\hat{\lambda}, t). \tag{4.31}$$

Moreover, according to the theory of viscosity solutions for the Hamilton-Jacobi equation [21], the value function is the unique viscosity solution of (4.28). It follows that the optimal trajectory $\hat{\lambda}(t)$ and, therefore, the resulting closed equations (4.31) are complete and uniquely determined.

From the definition of $f(\lambda)$, it is apparent that this term captures how the resolved vector, through the score variables, evolves directly according to the Liouville equation. Indeed, if we neglect the term with the value function in our closure equations, we get a system that resembles (4.3) and is time reversible. It follows that the value function is responsible for the irreversible nature of the reduced equations. Equivalently, the value function is responsible for entropy production of our system.

With this in mind, it is enlightening to return to look at the Hamiltonian corresponding to the decomposed Lagrangian given by (4.20) as well as the resulting Hamilton-Jacobi equation. Taking the Legendre transform of (4.20) gives us the Hamiltonian

$$\mathcal{H}(\lambda, \nu) = \frac{1}{2}\nu^T C(\lambda)^{-1}\nu + f(\lambda)^T C(\lambda)^{-1}\nu - d(\lambda).$$

Substituting this into (4.28) reveals that the function $d(\lambda)$ is a forcing function that drives the value function $v(\lambda, t)$ away from zero. Equivalently, if $d(\lambda) = 0$, then in light of the initial condition (4.28b), the solution of (4.28) is the trivial solution $v(\lambda, t) = 0$.

Returning to the decomposition (4.20), we see that the funciton $d(\lambda)$ arose from the unresolved component of the Liouville residual as it is the mean square of (4.19). Therefore, all irreversible effects in the closure are the result of the unresolved component of the Liouville residual. Recalling that our Lagrangian is a local truncation error version of the relative entropy, we see that this irreversibility is an information loss or an entropy production and so is completely analogous to the irreversibility of thermodynamics and equilibrium statistical mechanics.

4.4 Near Equilibrium Formulation

In general, computing the value function is quite difficult even numerically. This is simplified greatly if we are near an equilibrium. In this case, the Hamilton-Jacobi equation (4.28) reduces to a Riccati differential equation and the resulting closure is a linear system.

To see this, assume that $\lambda = 0$ corresponds to an equilibrium state given by ρ_{eq}, then the near equilibrium assumption corresponds to $|\lambda|$ being small. In this regime, we expect the quasi-equilibrium densities

$$\tilde{\rho} = \exp\{\lambda^T \mathbf{A} - \mu(\lambda)\}\rho_{eq}, \tag{4.32}$$

where

$$\mu(\lambda) = \log \left\langle \exp\{\lambda^T \mathbf{A}\} | \rho_{eq} \right\rangle, \tag{4.33}$$

to be a good approximation of the real density ρ. This family of densities minimizes the relative entropy $D_{KL}(\rho || \rho_{eq})$ under the constraint $\mathbf{a} = \langle \mathbf{A} | \rho \rangle$. Using this family of trial densities, the score variables are given by the resolved vector $\mathbf{A}$ and the Liouville residual is given by $R = \dot{\lambda}^T \mathbf{A} + \lambda^T L \mathbf{A}$.

Expanding about the equilibrium, our Lagrangian becomes

$$\mathcal{L}(\lambda, \dot{\lambda}) = \frac{1}{2}\dot{\lambda}^T C \dot{\lambda} + \lambda^T J \dot{\lambda} + \frac{1}{2}\lambda^T K \lambda \tag{4.34}$$

where

$$\begin{aligned} C &= C(0) = \left\langle \mathbf{A}\mathbf{A}^T | \rho_{eq} \right\rangle, \\ J &= \frac{\partial f}{\partial \lambda}(0) = \left\langle (L\mathbf{A})\mathbf{A}^T | \rho_{eq} \right\rangle, \\ K &= \left\langle (L\mathbf{A})(L\mathbf{A})^T | \rho_{eq} \right\rangle. \end{aligned}$$

From the definitions, we see that C and K are Gram matrices and, hence, symmetric and positive definite. J is anti-symmetric because L is an anti-Hermitian operator. Employing the form (4.20), we can write

$$\mathcal{L}(\lambda, \dot{\lambda}) = \frac{1}{2}[\dot{\lambda} - C^{-1}J\lambda]^T C [\dot{\lambda} - C^{-1}J\lambda] + \frac{1}{2}\lambda^T D \lambda, \tag{4.35}$$

where $D = \left\langle Q_\lambda(LA) Q_\lambda(LA)^T \right\rangle$. In terms of the above matrices, D is given by $D = K +$

$JC^{-1}J$. Again from the definition, we see that D must be symmetric positive-semidefinite.

The Legendre transform of the Lagrangian then gives us the Hamiltonian

$$\begin{aligned}\mathcal{H}(\lambda, \nu) &= \max_{\dot{\lambda} \in \mathbb{R}^m} \dot{\lambda}^T \nu - \mathcal{L}(\lambda, \dot{\lambda}) \\ &= \frac{1}{2}\nu^T C^{-1} \nu - \lambda^T J C^{-1} \nu + \frac{1}{2}\lambda^T D \lambda \end{aligned} \tag{4.36}$$

and explicitly computing the above maximum gives us the relation

$$\nu = \frac{\partial \mathcal{L}}{\partial \dot{\lambda}} = C\dot{\lambda} - J\lambda. \tag{4.37}$$

Since the Lagrangian (4.35) is a quadratic form, the value function which solves (4.28) must also be a quadratic form. Furthermore, it must satisfy the conditions

$$v(\lambda, 0) = 0, \tag{4.38}$$

$$v(0, t) = 0. \tag{4.39}$$

The first from the initial conditions and the second from the fact that $\lambda = 0$ is an equilibrium value. Combining (4.39) and (4.28) gives us the additional condition

$$\frac{\partial v}{\partial \lambda}(0, t) = 0 \tag{4.40}$$

As v is a quadratic form that satisfies conditions (4.39) and (4.40), we find that it must have the form

$$v(\lambda, t) = \frac{1}{2}\lambda^T M(t) \lambda, \tag{4.41}$$

where $M(t)$ must satisfy the matrix Riccati initial value problem

$$\frac{dM}{dt} + MC^{-1}M + JC^{-1}M - MC^{-1}J = D, \qquad M(0) = 0. \tag{4.42}$$

The Hamilton-Jacobi equation (4.28) reduces to equation (4.42) after substituting the value function given by (4.41) and the initial condition is the result of condition (4.38). Along optimal paths, the relation (4.30) reduces to

$$\hat{\nu} = -M\lambda.$$

To achieve closure, we combine this with (4.37) to get

$$C\dot{\lambda} = (J - M(t))\lambda. \tag{4.43}$$

We see that in the near equilibrium regime, the optimal closure reduces to a linear system of equations. Furthermore, comparing this to (4.31), we see that J corresponds to the action of the Liouville operator L on the resolved vector $\mathbf{A}$ and is reversible. The M component arises from the value function and is driven by the resolved variables interacting with the unresolved variables and is irreversible. Therefore our linear system appears as the sum of reversible and irreversible components. Additionally, we have reduced the solution of the full Hamilton-Jacobi equation (4.28) to the solution of the matrix Riccati differential equation (4.42). This has the advantage of being much more computationally tractable. However, we pay the price of being restricted to near an equilibrium state.

As an alternative method to achieve the above closure, we may approach the problem using optimal control theory. To this end, we introduce the "control" variable $\nu = C\dot{\lambda} - J\lambda$ so that $\dot{\lambda} = C^{-1}\nu + C^{-1}J\lambda$. Then our Lagrangian given by (4.35) can be written in the form

$$\mathcal{L}(\lambda, \nu) = \frac{1}{2}\lambda^T D\lambda + \frac{1}{2}\nu^T C^{-1}\nu,$$

which is simply the linear quadratic regulator problem from control theory [34]. It follows that the value function is given by the quadratic form

$$v(\lambda, t) = \frac{1}{2}\lambda^T M(t)\lambda, \tag{4.44}$$

where M is the matrix determined by the Riccati differential equation

$$\frac{dM}{dt} + MC^{-1}M + JC^{-1}M - MC^{-1}J = D, \qquad M(0) = 0, \tag{4.45}$$

and the optimal control is given by $\hat{\nu}(t) = -M(t)\lambda$ which combines with the definition of ν to give the closure

$$C\dot{\lambda} = (J - M(t))\lambda.$$

This perspective produces exactly the same result as the Hamilton-Jacobi theory given previously but allows us another interpretation. Here the $\hat{\nu}$ represents the optimal input to the reduced equations and relation $\hat{\nu} = -M\lambda$ is the linear state feedback so that the matrix M dictates the optimal response $\hat{\nu}$ to the state λ.

Either way, we have a system that completely determines the path $\lambda(t)$ so that we can form the trial density $\tilde{\rho}(\lambda(t))$ and compute $\mathbf{a}(t) = \langle \mathbf{A} | \tilde{\rho}(\lambda(t)) \rangle$.

Our near equilibrium assumption also provides a useful short cut. Since $\tilde{\rho}$ is given by (4.32), we have

$$\mathbf{a}(t) = \left\langle \mathbf{A}\mathbf{A}^T | \rho_{eq} \right\rangle \cdot \lambda + O(|\lambda|^2) = C\lambda + O(|\lambda|^2).$$

Therefore, the evolution of the mean resolved vector is given by the system

$$\dot{\mathbf{a}} = (J - M(t))\lambda, \qquad \mathbf{a} = C\lambda. \tag{4.46}$$

In this form, there is no need to form the trial densities. For a given value of λ, we can use the given equation to step $\mathbf{a}$ forward in time. Then using the relation $\mathbf{a} = C\lambda$, we can compute the corresponding value of λ. We can repeat this process as necessary.

We now look to quantify the entropy production rate of the closure in the near equilibrium regime. If we assume that the equilibrium density ρ_{eq} is given by a Gibbs distribution then (4.32) takes the form

$$\tilde{\rho} = \exp\{\lambda^T \mathbf{A} - \beta H - \mu(\lambda, E)\}$$

where $E = \langle H | \tilde{\rho} \rangle$ is the fixed mean energy and

$$\mu(\lambda, E) = \log \int_{\Lambda_N} \exp\{\lambda^T \mathbf{A} - \beta H\} d\mathbf{z}.$$

Then the entropy function is the negative of the Legendre transform of μ and is given by

$$s(E, a) = -\lambda^T \mathbf{a} + \beta E + \mu(\lambda, E),$$

and we have the resulting identity

$$\frac{\partial s}{\partial \mathbf{a}} = -\lambda.$$

From here we may compute the entropy production along the optimal path given by the closure. From the chain rule, we have

$$\frac{d\hat{s}}{dt} = \frac{d\hat{s}}{d\hat{\mathbf{a}}} \cdot \frac{d\hat{\mathbf{a}}}{dt}.$$

Upon using the near equilibrium closure, we find that

$$\frac{d\hat{s}}{dt} = -\lambda^T (J - M)\lambda = \hat{\lambda}^T M \hat{\lambda} = 2v(\hat{\lambda}, t) \tag{4.47}$$

where we have used the fact that $\lambda^T J \lambda = 0$ for any antisymmetric matrix J and real vector λ and we have recognized the value function given by (4.44). Since M is semi-positive definite, this proves that the closure has nonnegative entropy production. Indeed, as the value function is positive away from the lines $t = 0$ and $\lambda = 0$, we find that the rate of change of entropy is necessarily positive away from the initial time and equilibrium.

It should be noted that the positive entropy production is not unique to the near equilibrium optimal closure. In the general case using the trial densities (4.32), it can by shown that

$$\frac{d\hat{s}}{dt} \geq v(\hat{\lambda}, t) \geq 0$$

provided that the value function is convex [55].

In the following two chapters, we will combine the equilibrium statistical mechanics of point vortices and this near equilibrium formulation of the closure to study nonequilibrium point vortex systems and the dynamical process of symmetrizing of coherent vortex structures. In doing so, we find that in an appropriate mean-field limit, the closure reduces to an information theoretic residual on the Euler equation itself.

CHAPTER 5

NONEQUILIBRIUM STATISTICAL MECHANICS OF POINT VORTEX SYSTEMS

Nonequilibrium statistical mechanics attempts to predict the evolution of the "coarse-grained" smooth vorticity profile when not at equilibrium. There has been relatively little work on this problem in the context of point vortices.

In [38], Marmanis uses the standard technique of constructing the BBGKY (Bogolubov, Born, Green, Kirkwood and Yvon) hierarchy from the Liouville equation to model the evolution of a cloud of N identical positive and N identical negative point vortices. In this technique, reduced distribution functions are computed from the full distribution by integrating over many of the variables. For instance, if the full distribution is given by $\mathcal{D}_{NN}$, then the reduced distribution function for m positive and n negative point vortices F_{mn} is given by

$$F_{mn} = A^{m+n} \int \mathcal{D}_{NN} \prod_{i=m+1}^{N} dq_i dp_i \prod_{j=N+n+1}^{2N} dq_j dp_j$$

where A is the area that encloses all the point vortices. Many of the interesting physical quantities such as the average velocity, average vorticity field and the interaction energy can be written in terms of these reduced distribution functions. The equations governing the evolution of these reduced distribution functions is derived from the Liouville equation describing the evolution of $\mathcal{D}_{NN}$.

However, the closure problem appears again. The evolution equation for F_{mn} requires knowledge of $F_{(m+1)n}$ and $F_{m(n+1)}$. This dependence on higher order reduced distribution functions stops only when $m = n = N$ at which point the evolution equation is equivalent to the Liouville equation. To achieve closure an additional assumption is needed. Marmanis uses the "vortex-dipole-chaos" assumption. This states that "colliding dipoles come from different regions of space and have met in their past history different dipoles". Mathematically, it can be stated as

$$F_{22}(\mathbf{x}_1, \mathbf{x}_2, \mathbf{x}_{N+1}, \mathbf{x}_{N+2}) = F_{11}(\mathbf{x}_1, \mathbf{x}_{N+1})F_{11}(\mathbf{x}_2, \mathbf{x}_{N+2}).$$

This assumption is similar to the closure assumption used by Lundgren and Pointin [43]. Newton argues this approach is overly restrictive since the dipole is not a stable structure in a cloud of vortices [43].

Chavanis also makes use of the BBGKY methodology to derive a kinetic equation for N like signed vortex cloud [14]. To achieve closure, Chavanis argues that the n^{th} order reduced distribution function F_n scales like $1/N^{n-1}$ and points out that this requires either the initial condition to have no correlation or to respect this scaling. This assumption is then used to derive a kinetic equation that is valid to order $1/N$. However, in the mean-field limit, this kinetic equation reduces back to the Euler equation.

In an earlier work [13], Chavanis advocated another approach—the maximum entropy production principle . This principle states that nonequilibrium evolution should follow the path which produces the maximum amount of entropy. This approach produces an additional diffusive term in the Euler equation with an unknown diffusive coefficient. The coefficient cannot be determined from the maximum entropy production principle. In the case of point vortices, he uses linear response theory to compute the diffusion coefficient from the systematic drift before arriving at a Fokker-Planck type equation which is the aforementioned Euler equation with an additional diffusive term.

The previously outlined optimal closure procedure provides us with an alternative approach. In particular, in this section we will use the general theory described in the last chapter and apply it to a system of like signed (positive) point vortices to derive our own nonequilibrium theory. We will develop a time dependent version of the mean-field system (3.7) that describes the evolution of the desired variables. Our approach will produce an information theoretic residual on the Euler equation that quantifies the failure of the trial distribution to describe the evolution of the true the coarse grained continuum distribution. Closure is then obtained by minimizing this residual. Just as in the general case, closure is achieved completely by the theory with no adjustable parameters.

5.1 Mean-Field Formulation

As a starting point, we again consider a cloud of N identical point vortices of strength $\gamma = 1/N$ so that $\Gamma = 1$. We take as the trial density

$$\tilde{\rho}_N(\mathbf{x}_1, \ldots, \mathbf{x}_N) = \exp\{N\lambda^T \tilde{\mathbf{A}} - 2N\beta H^N - N\alpha L_N^2 - N\mu\} \tag{5.1}$$

where $\tilde{A}$ is the resolved vector, H^N is the Hamiltonian (2.15),

$$L_N^2 = \frac{1}{N}\sum_{i=1}^{N} |\mathbf{x}_i|^2$$

and the normalizing constant μ is given by

$$\mu = \frac{1}{N}\log\left(\int_{\mathbb{R}^{2N}} \exp\left[N\lambda^T \tilde{\mathbf{A}} - 2N\beta H^N - N\alpha L_N^2\right] d\mathbf{x}_1 \ldots d\mathbf{x}_N\right).$$

We now rewrite the trial density in a form similar to the meanfield equations (3.7). To do this, we assume that the resolved vector can be written in the form

$$\tilde{\mathbf{A}}(\mathbf{x}_1, \ldots, \mathbf{x}_N) = \frac{1}{N}\sum_{i=1}^{N} \mathbf{A}(\mathbf{x}_i).$$

This assumption on the resolved vector amounts to not introducing any additional dependence between the phase space variables. Physically, we can look at this as the point vortices interacting only through the stream function. Other than this assumption, we leave the resolved vector as general functions so that we may choose appropriate quantities of interest later. For example, if we were interested in a "coarse graining" of the shape of the vortex cloud, we may choose to track the spatial moments.

Using the definition of the Hamiltonian, we see that we can decompose it into the sum of stream functions. In particularly, we have

$$H^N = \sum_{i=1}^{N} \frac{1}{2N} \psi_i^N \tag{5.2}$$

where

$$\psi_i^N(\mathbf{x}, t) = -\frac{1}{2\pi} \sum_{j \neq i} \log |\mathbf{x} - \mathbf{x}_j(t)|. \tag{5.3}$$

We can now rewrite the trial density in the form

$$\tilde{\rho}_N(\mathbf{x}_1, \ldots, \mathbf{x}_N) = \prod_{i=1}^{N} \exp\left[\lambda^T \mathbf{A}_i - \beta \psi_i^N - \alpha r_i^2 - \mu\right] \tag{5.4}$$

where $r_i^2 = |\mathbf{x}_i|^2$ and $\mathbf{A}_i = \mathbf{A}(\mathbf{x}_i)$.

The idea is that we force the position of each point vortex to take the probability distribution of a quasi-equilibrium form where β and α take values so that the Hamiltonian (2.15) and the angular impulse (2.17) are conserved.

Before continuing, we can simplify the calculations by noting that the angular impulse may be treated as another element of the resolved vector $\mathbf{A}$. From here, until otherwise noted, we assume that the resolved vector carries the angular impulse with it.

We cannot do the same with the stream function term since it is time dependent. Indeed, this time dependence will turn out to be extremely important in our calculations and is a departure from the general theory described last chapter.

For this choice of trial density, we compute the Liouville residual

$$\begin{aligned} R &= (\partial_t + \left\{\cdot, H^N\right\}) \left(\sum_{i=1}^{N} \lambda^T \mathbf{A}_i - \beta \psi_i^N - \mu \right) \\ &= \sum_{i=1}^{N} \dot{\lambda}^T (\mathbf{A}_i - \mathbf{a}_i) - \dot{\beta}(\psi_i^N - \langle \psi_i^N | \tilde{\rho} \rangle) - \beta \partial_t (\psi_i^N - \langle \psi_i^N | \tilde{\rho} \rangle) \\ &\qquad + \lambda^T \left\{\mathbf{A}_i, H^N\right\} - \beta \left\{\psi_i^N, H^N\right\}, \end{aligned} \tag{5.5}$$

where H^N is given by (2.15) with $\gamma_i = \gamma$ and $\mathbf{a}_i = \langle \mathbf{A}_i | \tilde{\rho} \rangle$.

We can simplify this equation by noting several things. First, using (5.2) we find that

$$\beta\left\{\sum_{i=1}^{N}\psi_i^N, H^N\right\} = 2\beta N\{H^N, H^N\} = 0. \tag{5.6}$$

Second, since $q_i = \sqrt{\gamma}x_i$ and $p_i = \sqrt{\gamma}y_i$, the chain rule tells us

$$\frac{\partial F}{\partial q_i} = \frac{1}{\sqrt{\gamma}}\frac{\partial F}{\partial x_i}, \qquad \frac{\partial F}{\partial p_i} = \frac{1}{\sqrt{\gamma}}\frac{\partial F}{\partial y_i}.$$

Combining this with the definition of the stream function and Hamilton's equations, we find that

$$\frac{\partial H^N}{\partial q_i} = \sqrt{\gamma}\cdot\frac{\partial \psi_i^N}{\partial x_i}, \qquad \frac{\partial H^N}{\partial p_i} = \sqrt{\gamma}\cdot\frac{\partial \psi_i^N}{\partial y_i}.$$

Therefore we can write

$$\{F, H^N\} = \sum_{j=1}^{N}[F, \psi_j^N]_{(x_j,y_j)}, \tag{5.7}$$

where we have used the notation

$$[F, B]_{(x_j,y_j)} = \frac{\partial F}{\partial x_j}\frac{\partial B}{\partial y_j} - \frac{\partial F}{\partial y_j}\frac{\partial B}{\partial x_j}.$$

Using (5.6) and (5.7) in (5.5) and the fact that $\mathbf{A}_i$ is a function of $\mathbf{x}_i$ only, the equation for R reduces to

$$R = \sum_{i=1}^{N}\left(\dot{\lambda}^T(\mathbf{A}_i - \mathbf{a}_i) - \dot{\beta}(\psi_i^N - \langle\psi_i^N|\tilde{\rho}\rangle) - \beta\partial_t(\psi_i^N - \langle\psi_i^N|\tilde{\rho}\rangle) + \lambda^T[\mathbf{A}_i, \psi_i^N]_{(x_i,y_i)}\right).$$

We now seek to reduce this equation for the Liouville residual to a continuous mean-field form. To do this, we assume that $\zeta^N \to \zeta$ weakly as $N \to \infty$. From this, it results that $\psi_i^N \to \psi$ where ψ is related to ζ by

$$-\Delta\psi = \zeta = \rho,$$

and $\psi \sim -\log|\mathbf{x}|/2\pi$ as $|\mathbf{x}| \to \infty$. The proof of this fact is given in Appendix A. Therefore, for N large, we have $\psi_i^N \approx \psi$ and $\langle \psi_i^N | \tilde{\rho} \rangle \approx 2E$. It follows that

$$R = N(\dot{\lambda}^T(\mathbf{A} - \mathbf{a}) - \dot{\beta}(\psi - 2E) + \lambda^T[\mathbf{A}, \psi] - \beta\partial_t\psi),$$

where all spatial functions are now functions of $\mathbf{x} \in \mathbb{R}^2$. We also rescale the parameters λ and β to account for the N dependence. That is, we replace βN by β and λN by λ. This is the standard scaling in point-vortex statistical mechanics. Therefore, we have

$$R = \dot{\lambda}^T(\mathbf{A} - \mathbf{a}) - \dot{\beta}(\psi - 2E) + \lambda^T[\mathbf{A}, \psi] - \beta\partial_t\psi. \tag{5.8}$$

Since we do not have the true stream function ψ, we replace it by $\tilde{\psi}$ the stream function associated with the mean-field trial density $\tilde{\rho}$. These two functions are determined by the nonlinear system, after detaching the angular impulse function from the resolved vector,

$$\tilde{\rho}(\mathbf{x}) = \tilde{\zeta}(\mathbf{x}) = \exp\left\{\lambda^T\mathbf{A}(\mathbf{x}) - \beta\tilde{\psi}(\mathbf{x}) - \alpha r^2 - \mu\right\}, \tag{5.9a}$$

$$-\Delta\tilde{\psi} = \tilde{\zeta}, \tag{5.9b}$$

$$\int_{\mathbb{R}^2} \tilde{\psi} \cdot \tilde{\zeta}\, d\mathbf{x} = 2E, \tag{5.9c}$$

$$\int_{\mathbb{R}^2} |\mathbf{x}|^2\tilde{\zeta}\, d\mathbf{x} = L^2, \tag{5.9d}$$

$$\int_{\mathbb{R}^2} \tilde{\rho}\, d\mathbf{x} = 1, \tag{5.9e}$$

where $r^2 = |\mathbf{x}|^2$ and E and L^2 are the energy and angular impulse of the initial distribution.

Similarly, replacing ψ with $\tilde{\psi}$ in the Liouville residual and again explicitly writing the angular impulse, gives us the mean-field formulation of the Liouville residual

$$R = \dot{\lambda}^T(\mathbf{A} - \mathbf{a}) - \dot{\beta}(\tilde{\psi} - 2E) - \dot{\alpha}(r^2 - L^2) + [\lambda^T\mathbf{A} - \alpha r^2, \tilde{\psi}] - \beta\partial_t\tilde{\psi}. \tag{5.10}$$

Recalling that $\tilde{\rho} = \tilde{\zeta}$, we see that we can write this mean-field version of the Liouville residual as

$$R = \left(\partial_t + \left[\cdot, \tilde{\psi}\right]\right)\log\tilde{\rho} = \left(\partial_t + \left[\cdot, \tilde{\psi}\right]\right)\log\tilde{\zeta}. \tag{5.11}$$

In this light, we can interpret the Liouville residual as an information theoretic residual on the Euler equations instead of the Liouville equation. Our optimal closure theory now takes the form of prescribing a family of vorticity distributions and asking that it evolves in a manner that is most consistent with the Euler equations while restricted to this family. From this perspective, we have done away with the point vortices. However, the point vortex idealization has given us the vehicle to derive the appropriate residual on the Euler equations.

5.2 Near-Equilibrium Formulation

We now assume that we are close to a known statistical equilibrium state corresponding to $\lambda = 0$ so that $|\lambda|$ is small. This assumption has several consequences. First, it allows us to use the near-equilibrium formulation of the optimal closure. This allows us to easily solve the Hamilton-Jacobi equation associated with the optimization problem and compute the value function. In the general case, this is extremely difficult. Second, the mean-field formulation of our trial density is implicit. For a given value of λ, we need to solve the system (5.9). In what follows, we will see that the near-equilibrium assumption allows us to write our trial densities explicitly to first order.

To simplify the notation, we will adopt a couple of conventions. First, all averages, unless specifically noted otherwise, are now taken with respect to the equilibrium density ρ_{eq} and denoted by $\langle \cdot \rangle$. Second, the equilibrium average of the resolved vector is taken to be zero. This can easily be accomplished for any observable by replacing $\mathbf{A}$ with $\mathbf{A} - \mathbf{a}$.

We also remind the reader that by taking the total circulation $\Gamma = 1$, that the trial vorticity distribution is equal to the trial density, that is,

$$\tilde{\rho} = \tilde{\zeta}.$$

As a result, we use the two interchangeably and choose one over the other depending on the context.

5.2.1 Explicit Trial Density

We can regard the trial density as a perturbation away from the equilibrium being driven by λ. From this perspective, the nonzero λ value forces the values of α, β and μ away from the equilibrium values. Therefore, we set $\alpha = \alpha_{eq} - \alpha'$, $\beta = \beta_{eq} - \beta'$ and $\mu = \mu_{eq} + \mu'$ where the *eq* subscript indicates the equilibrium value and all prime values are $O(\lambda)$. Furthermore we can expand $\tilde{\psi}$ as

$$\tilde{\psi} = \psi_{eq} + \psi' + O(\lambda^2).$$

Then the trial density (5.9a) can be expanded as

$$\begin{aligned}\tilde{\rho} &= \exp\{\lambda^T \mathbf{A} + \alpha' r^2 + \beta'\psi_{eq} - \beta_{eq}\psi' - \mu' - \alpha_{eq} r^2 - \beta_{eq}\psi_{eq} - \mu_{eq}\} + O(\lambda^2) \\ &= \exp\{\lambda^T \mathbf{A} + \alpha' r^2 + \beta'\psi_{eq} - \beta_{eq}\psi' - \mu'\}\rho_{eq} + O(\lambda^2) \\ &= (1 + \lambda^T \mathbf{A} + \alpha' r^2 + \beta'\psi_{eq} - \beta_{eq}\psi' - \mu')\rho_{eq} + O(\lambda^2).\end{aligned}$$

This means that we can write the perturbation vorticity distribution as

$$\zeta' = (\lambda^T \mathbf{A} + \alpha' r^2 + \beta'\psi_{eq} - \beta_{eq}\psi' - \mu')\zeta_{eq}. \tag{5.12}$$

Now, ζ' depends linearly on ψ', as opposed to exponentially. Of course, to be able to explicitly write $\tilde{\rho}$, up to first order, we still need values for β', α' and μ' as well as an expression for ψ' that does not involve ζ'.

To accomplish this goal, we look to the energy constraint (5.9c), the angular impulse constraint (5.9d) and the probability or circulation constraint (5.9e). The probability constraint is most easily addressed, so we start with it.

Expanding $\tilde{\rho}$ in (5.9e) gives us

$$\int_{\mathbb{R}^2} \rho_{eq} + \rho' \, d\mathbf{x} + O(\lambda^2) = 1.$$

Since $\int_{\mathbb{R}^2} \rho_{eq} d\mathbf{x} = 1$, we conclude, using expression (5.12) and dropping higher order terms, that

$$\int_{\mathbb{R}^2} \mu' \rho_{eq} d\mathbf{x} = \int_{\mathbb{R}^2} (\lambda^T \mathbf{A} + \alpha' r^2 + \beta' \psi_{eq} - \beta_{eq} \psi') \rho_{eq} d\mathbf{x} \tag{5.13}$$

Using once more that $\int_{\mathbb{R}^2} \rho_{eq} d\mathbf{x} = 1$ as well as$\langle \psi_{eq} \rangle = 2E$, $\left\langle r^2 \right\rangle = L^2$ and $\mathbf{a} = 0$, we can reduce this to an explicit expression for μ'

$$\mu' = \alpha' L^2 + \beta' \cdot 2E - \beta_{eq} \left\langle \psi' \right\rangle . \tag{5.14}$$

Having found this expression for μ', we now derive a linear system for the coefficients β' and α'. Expanding $\tilde{\zeta}$ in (5.9d), using the fact that ζ_{eq} satisfies the constraint and neglecting higher order terms gives us

$$\int_{\mathbb{R}^2} r^2 \zeta' \, d\mathbf{x} = 0. \tag{5.15}$$

Similarly, expanding $\tilde{\zeta}$ and $\tilde{\psi}$ in (5.9c), using $\langle \psi_{eq} \rangle = 2E$ and neglecting higher order terms, gives us

$$\int_{\mathbb{R}^2} \psi_{eq} \zeta' + \psi' \zeta_{eq} d\mathbf{x} = 0. \tag{5.16}$$

Green's second identity allows us to write

$$\int_{\mathbb{R}^2} \psi_{eq} \zeta' d\mathbf{x} = \int_{\mathbb{R}^2} \psi' \zeta_{eq} d\mathbf{x},$$

so that we find ζ' must satisfy

$$\int_{\mathbb{R}^2} \psi_{eq} \zeta' d\mathbf{x} = 0, \tag{5.17}$$

and ψ' must satisfy

$$\int_{\mathbb{R}^2} \psi' \zeta_{eq} d\mathbf{x} = 0. \tag{5.18}$$

Note that (5.18) is equivalently stated as $\langle \psi' \rangle = 0$. We can therefore neglect the β_{eq} term in (5.14).

Because Poisson's equation is linear, we also know that ψ' is related to ζ' by

$$-\Delta \psi' = \zeta'. \tag{5.19}$$

Replacing ζ' in (5.19), using (5.12) and eliminating μ' using (5.14), we get

$$-\Delta\psi' = [\lambda^T \mathbf{A} + \alpha'(r^2 - L^2) + \beta'(\psi_{eq} - 2E) - \beta_{eq}\psi']\zeta_{eq}.$$

Upon rearranging, we find that ψ' satisfies the linear partial differential equation

$$(-\Delta + \beta_{eq}\zeta_{eq})\psi' = [\lambda^T \mathbf{A} + \alpha'(r^2 - L^2) + \beta'(\psi_{eq} - 2E)]\zeta_{eq}. \tag{5.20}$$

Because the equilibrium stream function satisfies the condition $\psi_{eq} \sim -\log|\mathbf{x}|/2\pi$ as $|\mathbf{x}| \to \infty$, the far-field condition on ψ' is that $\psi' \to 0$ as $|\mathbf{x}| \to \infty$. Now if we let G_{eq} denote the appropriate inversion operator, we can write

$$\psi' = \lambda^T G_{eq}[\mathbf{A}\zeta_{eq}] + \alpha' \cdot G_{eq}[(r^2 - L^2)\zeta_{eq}] + \beta' \cdot G_{eq}[(\psi_{eq} - 2E)\zeta_{eq}]. \tag{5.21}$$

As a direct consequence of this, we have the equations

$$\frac{\partial\psi'}{\partial\lambda_i} = G_{eq}[A_i\zeta_{eq}], \quad \frac{\partial\psi'}{\partial\alpha'} = G_{eq}[(r^2 - L^2)\zeta_{eq}], \quad \frac{\partial\psi'}{\partial\beta'} = G_{eq}[(\psi_{eq} - 2E)\zeta_{eq}]. \tag{5.22}$$

Note that ψ' is given by (5.21) without any dependence on ζ'. Therefore we can find ψ' provided that λ, β' and α' are known. Furthermore, the only dependence on t in (5.21) is in the coefficients λ, α' and β'. It follows that we can easily build ψ' by computing the terms given in (5.22), all of which may be done once after finding the appropriate equilibrium distribution, and then multiplying by the appropriate coefficients.

It remains to determine α' and β' in terms of λ. To do this, we substitute (5.21) and (5.14) into (5.12) to get

$$\zeta' = (\lambda^T P[\mathbf{A}] + \alpha' P[r^2] + \beta' P[\psi_{eq}])\zeta_{eq}, \tag{5.23}$$

where we have used the notation

$$P[F] = F - \langle F\rangle - \beta_{eq}G_{eq}[(F - \langle F\rangle)\zeta_{eq}] = F - \langle F\rangle - \beta_{eq}G_{eq}[(F - \langle F\rangle)\rho_{eq}].$$

Substituting (5.23) into (5.15) and rearranging gives us

$$-\beta' \int r^2 P[\psi_{eq}]\rho_{eq} d\mathbf{x} - \alpha' \int r^2 P[r^2]\rho_{eq} d\mathbf{x} = \lambda^T \int r^2 P[\mathbf{A}]\rho_{eq} d\mathbf{x}. \tag{5.24}$$

Similarly, substitution of (5.23) into (5.17) gives us the equation

$$-\beta' \int \psi_{eq} P[\psi_{eq}]\rho_{eq} d\mathbf{x} - \alpha' \int \psi_{eq} P[r^2]\rho_{eq} d\mathbf{x} = \lambda^T \int \psi_{eq} P[\mathbf{A}]\rho_{eq} dx. \tag{5.25}$$

Combining equations (5.24) and (5.25) results in a linear system of equations for α' and β' in terms of the observable coefficients λ

$$D_1 \begin{pmatrix} \beta' \\ \alpha' \end{pmatrix} = D_2 \lambda, \tag{5.26}$$

where

$$D_1 = -\begin{pmatrix} \operatorname{Cov}(\psi_{eq}, P[\psi_{eq}]) & \operatorname{Cov}\left(\psi_{eq}, P[r^2]\right) \\ \operatorname{Cov}\left(r^2, P[\psi_{eq}]\right) & \operatorname{Cov}\left(r^2, P[r^2]\right) \end{pmatrix}, \qquad D_2 = \begin{pmatrix} \operatorname{Cov}\left(\psi_{eq}, P[\mathbf{A}^T]\right) \\ \operatorname{Cov}\left(r^2, P[\mathbf{A}^T]\right) \end{pmatrix}.$$

Assuming that the matrix D_1 is nonsingular, we may write α' and β' as

$$\alpha' = \sum_{i=1}^{m} \alpha_i \lambda_i, \qquad \beta' = \sum_{i=1}^{m} \beta_i \lambda_i, \tag{5.27}$$

where α_i and β_i are the appropriate entries of the matrix $D_1^{-1} D_2$. These matrices are time independent so that the computation of the α_i and β_i coefficients only needs to be done once. We also remark that this implies

$$\alpha_i = \frac{\partial \alpha'}{\partial \lambda_i}, \qquad \beta_i = \frac{\partial \beta'}{\partial \lambda_i}. \tag{5.28}$$

Returning to equation (5.21) and substituting (5.27) for α' and β', we get the equation

$$\psi' = \sum_{i=1}^{m} \lambda_i G_{eq}[(A_i + \alpha_i(r^2 - L^2) + \beta_i(\psi_{eq} - 2E))\rho_{eq}] \tag{5.29}$$

so that we have reduced ψ' to a function of λ alone. It is natural to define the quantity

$$\psi_i = G_{eq}[(A_i + \alpha_i(r^2 - L^2) + \beta_i(\psi_{eq} - 2E))\zeta_{eq}] \tag{5.30}$$

so we may write (5.29) as

$$\psi' = \sum_{i=1}^{m} \psi_i \lambda_i.$$

We have now achieved our goal of writing our trial densities explicitly. For a given λ, we can compute α' and β' using (5.27) and ψ' using (5.29). From these we may form ζ' from (5.12). Adding this to the equilibrium distribution ζ_{eq} gives us our trial density to leading order.

5.2.2 Liouville Residual and Closure

Now that we have an explicit form for the trial density, we seek to determine the corresponding form of the Liouville residual and formulate the closed equations.

Recall that for the mean-field trial density

$$\tilde{\rho} = \exp\{\lambda^T \mathbf{A} - \beta\tilde{\psi} - \alpha r^2 - \mu\},$$

the Liouville residual is given by

$$R = \dot{\lambda}^T \mathbf{A} - \dot{\beta}(\tilde{\psi} - 2E) - \dot{\alpha}(r^2 - L^2) - \beta\partial_t\tilde{\psi} + \lambda^T[\mathbf{A}, \tilde{\psi}] - \alpha[r^2, \tilde{\psi}].$$

Making use again of the expansions $\alpha = \alpha_{eq} - \alpha'$, $\beta = \beta_{eq} - \beta'$, $\mu = \mu_{eq} + \mu'$ and

$$\tilde{\psi} = \psi_{eq} + \psi' + O(\lambda^2),$$

we find that the leading order term of the Liouville residual is given by

$$R = \dot{\lambda}^T \mathbf{A} + \dot{\alpha}'(r^2 - L^2) + \dot{\beta}'(\psi_{eq} - 2E) - \beta_{eq}\partial_t\psi' + \lambda^T[\mathbf{A}, \psi_{eq}] - \alpha_{eq}[r^2, \psi']. \tag{5.31}$$

The chain rule tells us that

$$\partial_t\psi' = \sum_{i=1}^{m} \dot\lambda_i \left(\frac{\partial\psi'}{\partial\lambda_i} + \frac{\partial\psi'}{\partial\beta'}\frac{\partial\beta'}{\partial\lambda_i} + \frac{\partial\psi'}{\partial\alpha'}\frac{\partial\alpha'}{\partial\lambda_i} \right).$$

These partial derivatives are given by equations (5.22) and (5.28) so that we can write

$$\partial_t\psi' = \sum_{i=1}^{m} \dot\lambda_i G_{eq}[(A_i + \alpha_i(r^2 - L^2) + \beta_i(\psi_{eq} - 2E))\rho_{eq}] \tag{5.32}$$

$$= \sum_{i=1}^{m} \dot\lambda_i \psi_i, \tag{5.33}$$

where we have recognized the definition of ψ_i given by equation (5.30). Indeed, the above equation is just the time derivative of equation (5.29). This is not surprising as the only time dependency in (5.29) is in the coefficient vector λ. Furthermore, equation (5.28) also implies that

$$\dot\alpha' = \sum_{i=1}^{m} \dot\lambda_i \alpha_i, \qquad \dot\beta' = \sum_{i=1}^{m} \dot\lambda_i \beta_i.$$

Substituting our equations for $\partial_t\psi'$ and ψ' into the Liouville residual and expanding the vector multiplication, gives us, to leading order,

$$R = \sum_{i=1}^{m} \dot\lambda_i \left(A_i + \alpha_i(r^2 - L^2) + \beta_i(\psi_{eq} - 2E) - \beta_{eq}\psi_i\right) + \lambda_i \left([\mathbf{A}_i, \psi_{eq}] - \alpha_{eq}[r^2, \psi_i]\right) \tag{5.34}$$

If we define the vectors $\mathbf{U}$ and $\mathbf{V}$ by

$$U_i = A_i + \alpha_i(r^2 - L^2) + \beta_i(\psi_{eq} - 2E) - \beta_{eq}\psi_i, \tag{5.35}$$

$$V_i = [A_i, \psi_{eq}] - \alpha_{eq}[r^2, \psi_i], \tag{5.36}$$

we can compactly write the Liouville residual as

$$R = \dot\lambda^T \mathbf{U} + \lambda^T \mathbf{V}. \tag{5.37}$$

This is a Liouville residual that respects the circulation, angular impulse and energy constraints to leading order.

Squaring and taking the expectation gives us

$$\langle R^2 \rangle = \dot{\lambda}^T \langle \mathbf{U}\mathbf{U}^T \rangle \dot{\lambda} + \lambda^T \langle \mathbf{V}\mathbf{U}^T \rangle \dot{\lambda} + \lambda^T \langle \mathbf{V}\mathbf{V}^T \rangle \lambda.$$

Comparing this with (4.34), we are lead to define the matrices

$$C = \langle \mathbf{U}\mathbf{U}^T \rangle, \;\; J = \langle \mathbf{V}\mathbf{U}^T \rangle, \;\; K = \langle \mathbf{V}\mathbf{V}^T \rangle. \tag{5.38}$$

It is clear that we can now use the near-equilibrium closure as described previously: the optimal path $\hat{\lambda}(t)$ satisfies the linear system

$$\dot{\lambda} = C^{-1}(J - M(t))\lambda$$

where C and J are given above and $M(t)$ is given by the initial value problem

$$\dot{M} + MC^{-1}M + JC^{-1}M - MC^{-1}J = D, \qquad M(0) = 0,$$

where $D = K + JC^{-1}J$. Finally, the average of the resolved vector is given by

$$\mathbf{a}(t) = \left\langle \mathbf{A} | \tilde{\rho}(\hat{\lambda}(t)) \right\rangle = C\hat{\lambda}(t).$$

CHAPTER 6

SYMMETRIZATION OF POINT VORTEX DISTRIBUTION

A major development in high Reynolds number fluid dynamics was McWilliams discovery of the emergence of isolated persistent vortices from a disorderly initial vorticity distribution [40]. This discovery stood in stark contrast to the cascade theory of turbulence in which vorticity patches were ripped apart until they were small enough that they would dissipate due to the fluid viscosity. McWilliams argued that the vorticity extrema of sufficient magnitude resisted the strain deformations due to neighboring vorticity structures which lead to turbulent cascade. These extrema would continue to accumulate circulation and grow in size. In long time, this results in the isolated coherent vortices which then dominated the dynamics.

McWilliams noted two types of interactions in this long time regime: Pairwise interactions and relaxation towards axisymmetry. The pairwise interaction is the most common and occurs when the vortices are separated by distances significantly larger than the vortex size. Here the isolated patches appear as point vortices to one another and advect each other as described by (2.14). The relaxation toward axisymmetry occurred after a close approach by another vorticity concentration. In this close encounter, one of two things would happen. Either the vortices would strain and distort one another away from the normal axisymmetric state or the two vortices would merge (this requires the two patches to be of the same sign). In the latter case one of the two vortices, usually the weaker one, is ripped apart and the remaining vortex absorbs some of its circulation while the rest is lost to the turbulent cascade. Once the two vortices are far apart again or the merging process is complete, we see the relaxation back toward an axisymmetric state.

We will apply the closure theory developed in the preceding chapter to study this axisymmetrization process. Apart from being a phenomena generally of interest in two-dimensional turbulence theory, it is well positioned for us to study with the optimal closure for a couple of reasons. First, the axisymmetric states are precisely those described by the equilibrium statistical mechanics of point vortices as described in chapter 3. This means that we will be able to use the near equilibrium formulation of the optimal closure and so avoid computing solutions of the Hamilton-Jacobi equation. Second, we will be able to elegantly describe the problem with only two resolved quantities—the second spatial moments of the cloud. As a conclusion in studying the problem, we also predict how the rate of symmetrization depends on the inverse temperature of the final equilibrium state. Since there is a one-to-one correspondence of β and the energy, this is equivalent to the dependence of the energy.

6.1 Observables

As has been stated, we want to look at the rate of radial symmetrization of a point vortex distribution. A natural way to characterize the asymmetry is to consider the spatial moments. The first moments are given precisely by the center of vorticity and always lie at the origin. Therefore we consider the second moments x^2, xy and y^2. These moments completely determine an elliptical vorticity patch and form a natural "first-order" approximation of the radial asymmetry.

We will not use the second moments in the standard form though. Since $r^2 = x^2 + y^2$ is radially symmetric and a conserved quantity, it makes sense to choose the simple observables

$$A_1(\mathbf{x}) = x^2 - y^2, \qquad A_2(\mathbf{x}) = 2xy. \tag{6.1}$$

This form of the three second moments has the benefit of being orthogonal with respect to any radially symmetric distribution such as the equilibrium vorticity.

We call (somewhat arbitrarily) A_1 the orientation and A_2 the ellipticity. The reasoning for this is that $\langle A_2 \rangle$ looks like (twice) a covariance and so measures how compressed the cloud is along the line $y = x$. Given this measurement, the only other degree of freedom is the rotation of the ellipse, or the orientation. These names are arbitrary since in polar coordinates $A_1 = r^2 \cos(2\theta)$ and $A_2 = r^2 \sin(2\theta)$ and so the two observables differ only by

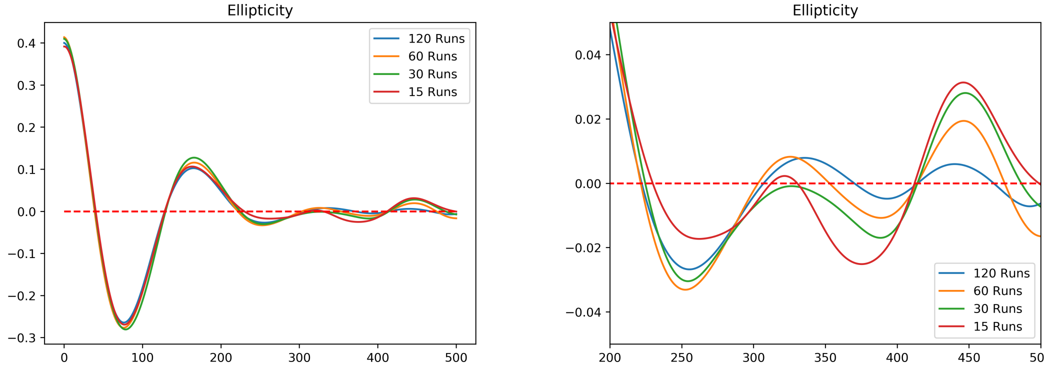

Figure 6.1: Plot of ellipticity for various number of runs. All runs consisted of 1000 point vortices drawn from a bivariate normal random variable with unit x and y variance and covariance of 0.2. The right plot shows the same data but is zoomed in on time $t = 200$ to $t = 500$. During this time range, the cloud can be said to be in equilibrium so the right hand plot shows the deviations from equilibrium for a given number of runs. These give a rough estimate of the sampling error incurred by using a finite number of runs. This magnitude of error should be understood to be present throughout the entire time interval and not just at equilibrium.

a rotation of $\pi/2$.

6.2 Results

We regard the truth as the mean of many numerical simulations of the system (2.14). We call this ensemble direct numerical simulations (EDNS). Specifically, we took $N = 1000$ and $\gamma = 10^{-3}$. Recall also that we fixed the angular impulse at $L^2 = 2.0$. To integrate this system, we use the standard 4th order Runge-Kutta scheme with a step-size of $\Delta t = 10^{-2}$. This step size was chosen so that the change in the conserved quantities was not significant (generally $< 10^{-6}$ although single runs occasionally violated this) through simulation time $t = 500$. The initial point vortex positions were generated randomly from some appropriate distribution. The details of the distribution are discussed on a case by case basis. For this reason, the initial conditions given are not the precise initial conditions of the direct numerics.

There are also sampling error effects in the EDNS curves. Because the curves are a sample mean approximation of the true expected value, the given curve is not the exact evolution of the initial distribution but an approximation. From a (frequentist) statistics point of view, each curve is an estimator of the true evolution and has an interval associated with it in which the actual evolution lies with some chosen probability. The size of the interval depends on the number of samples, or runs in our case, and the chosen probability with the interval decreasing in magnitude as the number of samples increases and increasing in magnitude as we choose larger probabilities. At equilibrium, the true curve would never deviate from the equilibrium value. Therefore, the magnitude of fluctuations around the equilibrium value gives a rough estimate of the magnitude of the sampling error incurred by using a finite sample size. Figure 6.1 depicts the evolution of the ellipticity for several different numbers of runs and particularly focuses on the long times when the observable can be said to be in equilibrium. Based on these curves and the amount of wall clock time required to run the system (especially in the single-layer case where it is necessary to compute a modified Bessel function of the second kind), we deemed 60 ensemble runs to have sufficiently small sampling error.

In addition to the time plots, we look at several error quantities. The classic relative error is given by

$$e_{rel} = \frac{\max_t |a_{truth}(t) - a_{pred}(t)|}{\max_t |a_{truth}(t)|}.$$

In the context of classical numerical methods, this is an adequate measure of error. Given the drastic model reduction we have undertaken, it is not realistic to expect this error to be small in the normal sense. Indeed, the closure consistently has a higher frequency (rotates more quickly) than the EDNS so that the best runs have relative error of roughly 10%.

Because exactly predicting the correct curve is not our main goal, we also look at a different error quantity. We define peak error as the difference between the corresponding first peaks. That is, if we denote the first local extrema in the domain $t > 0$ by p_{truth} for the EDNS value and p_{pred} for the closure, then the peak error is given by

$$e_{peak} = |p_{truth} - p_{pred}|.$$

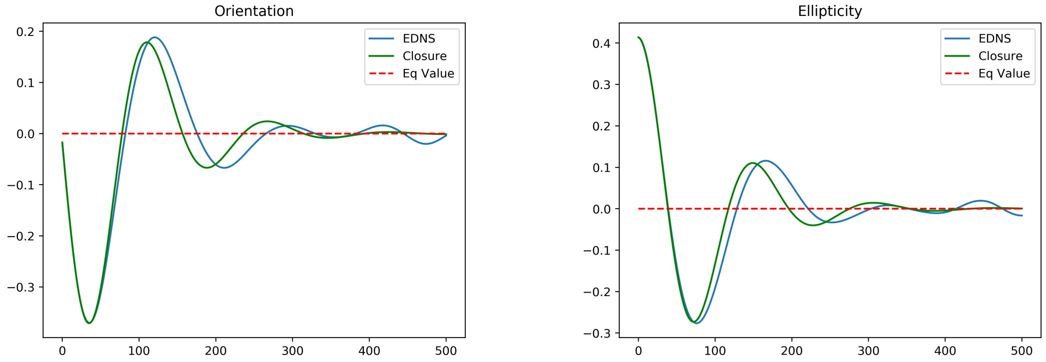

Figure 6.2: EDNS compared to the optimal closure for case 1. The initial values are $a_1 = 0.0$ (orientation) and $a_2 = 0.4$ (ellipticity). The first and second and even the third peaks are captured well by the closure. We see good agreement on how long it takes to equilibrate.

The relative peak error is given by

$$e_{relpeak} = \frac{|p_{truth} - p_{pred}|}{|p_{truth}|}.$$

This is a good measure of error if we are primarily interested in predicting the magnitude of departures from equilibrium. Specifically, perhaps we are interested in how a deviation from equilibrium in one quantity drives a deviation from equilibrium in another quantity. For example, we could view our current problem as a deviation in the ellipticity driving a deviation in the orientation and our goal is to predict the magnitude of the latter. In this context, the relative peak error is a very good measure of the predictive power of the closure.

Observable	Init Cond	Abs Peak Err	Rel Peak Err	Max Abs Err	Rel Err
a_1	0.0	8.98389e-04	2.42757e-03	7.93252e-02	2.14348e-01
a_2	0.4	3.42847e-03	1.24019e-02	7.36481e-02	1.77998e-01
a_1	0.0	2.98681e-02	4.14740e-02	8.19773e-02	1.13831e-01
a_2	0.8	5.71151e-02	1.10310e-01	8.36808e-02	1.03865e-01
a_1	0.0	1.11250e-01	1.04882e-01	1.89100e-01	1.78276e-01
a_2	1.2	1.73228e-01	2.48632e-01	2.45297e-01	2.03629e-01

Table 6.1: Absolute and relative errors of the closure compared to EDNS for the Euler equation. Peak error is the difference between the first extreme values occurring after $t = 0$. In the first two cases the peak error is considerably better than the relative error. This is the result in the closure result rotating faster than the EDNS.

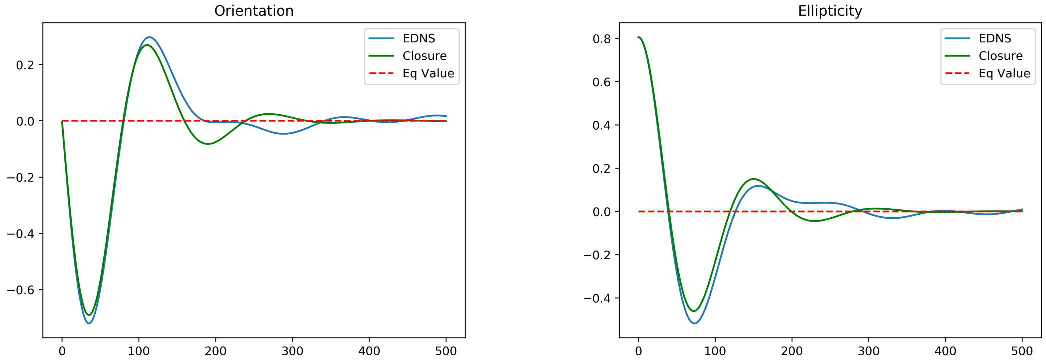

Figure 6.3: EDNS compared to the optimal closure for case 2. The initial values are $a_1 = 0.0$ and $a_2 = 0.8$. The closure captures the first two peaks well. It predicts a third peak that is not present in the EDNS. In fact, the behavior of the EDNS around $t = 200$ (where the closure predicts the third peak) begins to show nonlinear behavior. The equilibration time is still roughly the same.

Figures 6.2, 6.3 and 6.4 compare the numerical simulation (blue) and the optimal closure prediction (green) for three different initial conditions: $a_2 = 0.4$, $a_2 = 0.8$ and $a_2 = 1.2$ with $a_1 = 0.0$ in all cases. These were generated using a bivariate normal random variable with unit x and y variance and covariance 0.2, 0.4 and 0.6, respectively. Table 6.1 gives the discussed error quantities for these cases. Figures 6.5, 6.6 and 6.7 depict the evolution of a single vortex ensemble up to simulation time 250 at intervals of 50 time units. Overlaid on each frame is the contour plot of the optimal trial density.

In terms of the relative error, the second case with initial conditions $a_1(0) = 0.0$ and $a_2(0) = 0.40$ generates the best results (roughly 90% accuracy for both observables). While the relative error of the first and third cases are comparable, we see from the plots that in the first case, the error is a result of phase difference—the optimal closure rotates faster than in actuality. Whereas in the third case, we start to see a failure to capture the magnitude of the peak. This failure is expressed in the relative peak error. About 1% in case 1 versus 25% in case 3. Furthermore, there appears to be a significant nonlinear behavior around $t = 150$ immediately before the observables settle into their equilibrium values. By nonlinear behavior, we mean a behavior that cannot be captured by our linear reduced model.

Looking at the vortex ensemble and closure contour plots in figure 6.7 suggests what is happening. As the ellipticity of the initial vortex cloud is increased, we see the evolution of

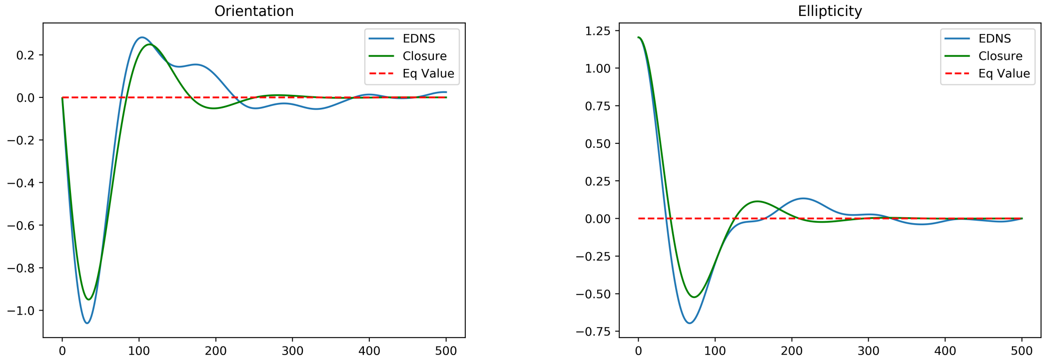

Figure 6.4: EDNS compared to the optimal closure for case 3. The initial values are $a_1 = 0.0$ and $a_2 = 1.2$. We start to see the closure fail to adequately capture the first peak and we see significant nonlinear behavior in the vortex ensemble average in the ellipticity graph (right) around time $t = 125$ and in the orientation graph (left) around time $t = 150$. The predicted equilibration time is shorter than the EDNS.

the ensemble form arms stretching out from the core. The larger the initial ellipticity values, the further these arms cut into the core of the vortex cloud. This results in nearly zero vorticity where the closure predicts nonzero vorticity. Note in figure 6.7 in the simulation time 100 panel, the significant white space in the upper left and, to a lesser extent, the lower right inside of the outer most contour. This is a behavior we cannot capture with our choice of observables and, hence, with our reduced model.

The value of the peak error, the nonlinear behavior of the observables and the unpredicted bare patches are all failures of our model to predict the true behavior. There are a couple obvious possible causes. First, there is a significant unresolved variable that should be included in the model to attempt to capture the nonlinear behavior and the bare patches. This amounts to an error in observable choice—we are not watching all of the appropriate quantities. Second, it is possible that there is a significant nonlinear interaction between either the resolved variables themselves or the resolved and the unresolved variables. Since our near-equilibrium assumption means that we treat all these relationships linearly, we cannot hope to capture this interaction. Stated simply, our near-equilibrium assumption may be false.

Whatever the cause, this failure occurs between case 2 and case 3. For these two cases, the initial magnitude (in the two norm) of λ is approximately 0.145 and 0.167 so we can

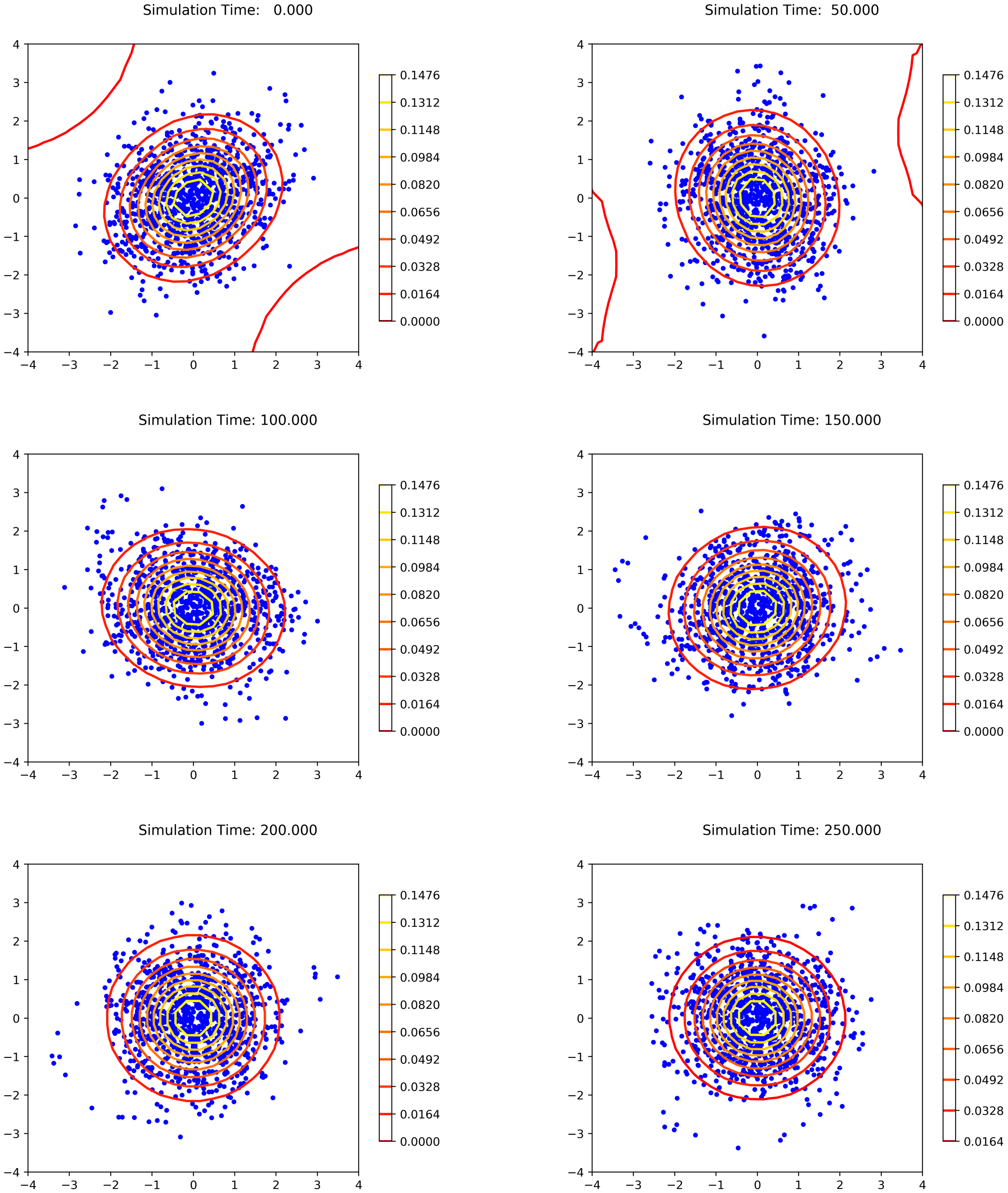

Simulation Time: 0.000

Simulation Time: 50.000

Simulation Time: 100.000

Simulation Time: 150.000

Simulation Time: 200.000

Simulation Time: 250.000

Figure 6.5: Contour plot of the closure density overlaying the evolution of a vortex ensemble for case 1 of the Euler equation. The initial condition are $a_1 = 0.0$ and $a_2 = 0.4$. The simulation times are at the top of each graphic. Note the contours and the cloud match up well. The closure has largely symmetrized by time $t = 200$. Outside of the contours we see that some of the point vortices do not appear equilibrated even in the last panel. There is some suggestion of arm structures reaching out of the core.

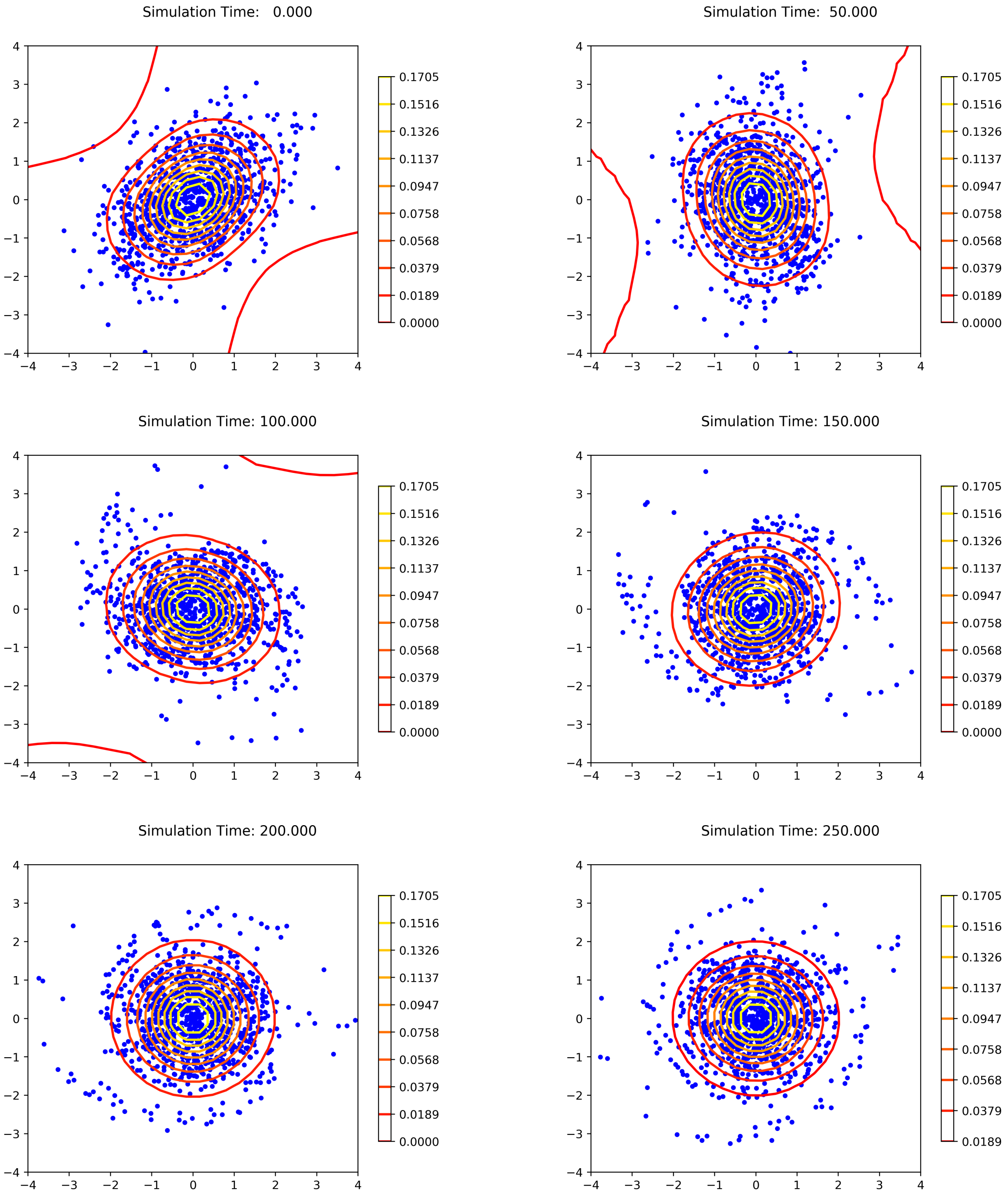

Simulation Time: 0.000

Simulation Time: 50.000

Simulation Time: 100.000

Simulation Time: 150.000

Simulation Time: 200.000

Simulation Time: 250.000

Figure 6.6: Contour plot of the closure density overlaying the evolution of a vortex ensemble for case 2 of the Euler equation. The initial conditions are $a_1 = 0.0$ and $a_2 = 0.8$. The simulation times are at the top of each graphic. We see that the contours and the core of the vortex patch line up well. The last four panels show the formation and lengthening of the spiral arms. In this case, these arms do not reach the core of the cloud. We can also see that they are formed from a small fraction of the total vorticity.

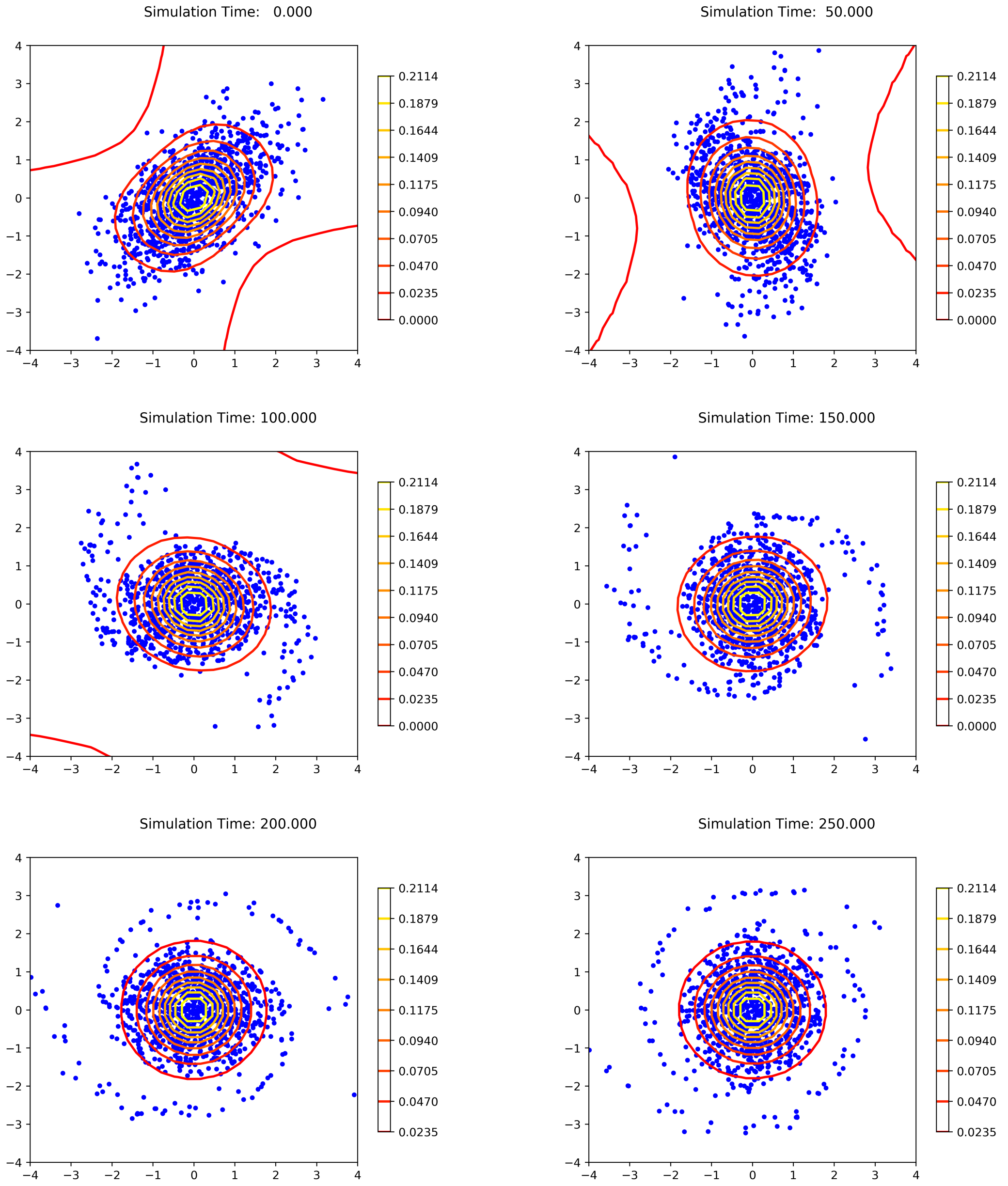
Simulation Time: 0.000

Simulation Time: 50.000

Simulation Time: 100.000

Simulation Time: 150.000

Simulation Time: 200.000

Simulation Time: 250.000

Figure 6.7: Contour plot of the closure density overlaying the evolution of a vortex ensemble for case 3 of the Euler equation. The initial condition are $a_1 = 0.0$ and $a_2 = 1.2$. The simulation times are at the top of each graphic. We see the formation of the arms earlier than case 2 (see figure 6.6) and they are starting to reach the core of the cloud. This is most apparent in the middle-left panel where there are noticeable blank spots in side the outermost contour. We can still clearly see the arms in the last frame.

say our model is good up to roughly $|\lambda| = 0.15$.

As mentioned, we could attempt to improve our model by including more observables—most obviously higher spatial moments. However, we start to run into some problems. The first has to do with the nature of our point vortex system. Many of these fringe vortices do not equilibrate. Specifically, we see that the spiral arms persist for quite awhile. This was not a problem for the second moments which are dominated by the behavior of the vortex cloud core. However, the higher moments weight the fringe vortices more heavily since they are further from the center of vorticity at the origin. Indeed, simulations suggest that the fourth moments take a very long time to reach equilibrium (simulation times great than 2000) if they ever do reach equilibrium.

The second problem has to do with our model. The only radial function that is conserved by the point vortex system is the angular impulse. It is tedious but not difficult to show that $\{f(r), H^N\} = 0$ if and only if $f(r) = r^2$. This is not the case with our model. Consider the definition of V_i given by (5.36) where A_i is a purely radial function. Since $[f, g] = 0$ for any two radially symmetric functions, we see that the first term of V_i vanishes. Looking at (5.30), and again taking A_i to be a radial function, we see that ψ_i is also a radial function so that $V_i = 0$ for any radial function. From the definition of the matrices K, J and D it follows that

$$K_{ij} = K_{ji} = J_{ij} = J_{ji} = D_{ij} = D_{ji} = 0, \quad j = 1, \ldots, m.$$

Using the Riccati differential equation for M then tells us that, for any j,

$$\dot{M}_{ij} = \sum_{k=1}^{m} \sum_{\ell=1}^{m} M_{ik} C^{-1}_{k\ell} (J_{\ell j} - M_{\ell j}).$$

Since $M(0) = 0$, it follows that $\dot{M}_{ij}(0) = 0$ and so $M_{ij}(t) = 0$ for any j. Therefore, our model does not equilibrate any purely radial function. This fact causes problems when trying to include the fourth (or higher) moments as observables.

Despite these failings, our model does have some notable highlights. First, we have greatly reduced the complexity of the system. Our original point vortex cloud was a 2000 dimensional system and our model reduced it a simple two-dimensional system. Second, our model, including the irreversible component, is derived directly from the dynamics of point vortices without resorting to any adjustable parameters. Third, our model is truly predictive. This stands in stark contrast to linear response theory which requires the computation of autocorrelation functions which in turn requires direct numerical simulation of the full model. Fourth, our closure procedure has a built in quantity to evaluate its performance provided by the value function. Intuitively, the larger the value function for a given model, the worse the performance. In the near equilibrium regime, actually computing the value function is a minimal amount of extra work. The value function is given by $\lambda^T M \lambda$ and we have to compute M to propagate the mean resolved vector.

6.3 Equilibration Rate Dependence on Inverse Temperature

We look to predict the dependence of the equilibration rate on the parameter β. Since there is a one-to-one correspondence between the energy level and β, we can also view this as how the relaxation rate depends on the energy. We first need to find a sensible measure of this rate as given by the closure.

We start by looking at how the matrices C and K simplify for our choice of observables. First note that both A_1 and A_2 are orthogonal to the radial functions r^2 and ψ_{eq} with respect to ρ_{eq}. Next note that the operator G_{eq} and the equilibrium distribution ρ_{eq} are purely radial functions. Finally, writing the observables in polar coordinates, we have $A_2(r,\theta) = A_1(r, \theta + \pi/4)$ which is again just the realization that the two observables are the same after a phase shift.

Combining these facts results three things. First, provided that D_1 is nonsingular, we have $\alpha_1 = \alpha_2 = \beta_1 = \beta_2 = 0$. In turn, this means that $\mathbf{U}$ reduces to

$$U_i = A_i - \beta_{eq} \psi_i.$$

Second, that ψ_1 and ψ_2 also differ by only a phase shift. In polar coordinate, we have $\psi_2(r,\theta) = \psi_1(r, \theta + \pi/4)$. Third, we have

$$\langle A_1 \psi_2 \rangle = \langle A_2 \psi_1 \rangle = 0.$$

The proofs of each of these simply follow from writing the necessary convolution with the Green's function in polar coordinates and using the polar forms of the observables to reduce the integrals to the desired result. As such, they are tedious and uninformative and so have been omitted.

We now use the above results to simplify the matrices C and K. In particular, we have the following

$$\left\langle U_1^2 \right\rangle = \left\langle U_2^2 \right\rangle, \quad \left\langle V_1^2 \right\rangle = \left\langle V_2^2 \right\rangle, \quad \langle U_1 U_2 \rangle = \langle V_1 V_2 \rangle = 0$$

It follows that C, C^{-1} and K are diagonal matrices with equal entries. Since both these matrices are diagonal and J is antisymmetric, we find that D must also be a diagonal matrix with equal nonzero entries. To summarize, we have the following

$$C^{-1} = \begin{pmatrix} c & 0 \\ 0 & c \end{pmatrix}, \quad K = \begin{pmatrix} \kappa & 0 \\ 0 & \kappa \end{pmatrix}, \quad J = \begin{pmatrix} 0 & -\sigma \\ \sigma & 0 \end{pmatrix}, \quad D = \begin{pmatrix} d & 0 \\ 0 & d \end{pmatrix}.$$

where

$$c = \left\langle U_1^2 \right\rangle = \left\langle U_2^2 \right\rangle, \quad \sigma = -\langle V_1 U_2 \rangle = \langle V_2 U_1 \rangle, \quad \kappa = \left\langle V_1^2 \right\rangle = \left\langle V_2^2 \right\rangle.$$

and U_i and V_i are given by (5.35) and (5.36), respectively, and the resolved vector $\mathbf{A}$ is given by (6.1).

For these matrices, it is not difficult to show that the matrix

$$M(t) = \begin{pmatrix} m(t) & 0 \\ 0 & m(t) \end{pmatrix}$$

is a solution of the Riccati equation (4.42) provided $m(t)$ is a solution of the initial value problem

$$\dot{m} = d - cm^2, \quad m(0) = 0.$$

Since the solution to (4.42) is unique, we know that M is a diagonal matrix with equal nonzero entries. Furthermore, we know that $M(t)$ converges to a stationary solution as $t \to \infty$. (This is a result from Ricatti equation theory [34] but can also be seen from the above initial value problem for m.) From this, it follows that $m(t)$ goes to the solution of the stationary equation

$$0 = \kappa - \sigma^2 c - cm^2$$

where we have used the definition of D to compute $d = \kappa - \sigma^2 c$. Solving for m we find that

$$m = \sqrt{\frac{\kappa - c\sigma^2}{c}}. \tag{6.2}$$

We have discarded the negative root because M is positive definite. This is the longtime (repeated) eigenvalue of M.

This eigenvalue, in fact, determines the rate at which the closures relaxes back to equilibrium. The relative entropy (4.5) again gives us a suitable measure for how far our trial distribution is from equilibrium. Note that we can write the near-equilibrium trial density as

$$\tilde{\rho} = \exp\{\lambda^T \mathbf{U} - \phi(\lambda)\}\rho_{eq},$$

where

$$\phi(\lambda) = \log\left(\int_{\mathbb{R}^2} \exp\{\lambda^T \mathbf{U}\}\rho_{eq}\, d\mathbf{x}\right)$$

so that we are exactly enforcing the probability constraint (5.9e). From the definition of the relative entropy, we find that

$$D_{KL}(\rho_{eq}||\tilde{\rho}) = \phi(\lambda).$$

Using the fact that λ is small and Taylor's theorem we find that

$$\begin{aligned}\phi(\lambda) &= \log\left[\int_{\mathbb{R}^2}\left(1 + \lambda^T\mathbf{U} + \frac{1}{2}\lambda^T\mathbf{U}\mathbf{U}^T\lambda\right)\rho_{eq}\, d\mathbf{x} + O(|\lambda|^3)\right]\\ &= \frac{1}{2}\lambda^T C\lambda + O(|\lambda|^3),\end{aligned}$$

where we have used the fact that $\langle \mathbf{U} \rangle = 0$. Therefore,

$$D_{KL}(\rho_{eq}||\tilde{\rho}) = \frac{1}{2}\lambda^T C\lambda \tag{6.3}$$

so that the leading order term of the relative entropy is related to the Fisher information matrix.

Taking the time derivative of this we find that

$$\begin{aligned}\frac{d}{dt}D_{KL}(\tilde{\rho}||\rho_{eq}) &= \lambda^T C C^{-1}(J-M)\lambda \\ &= -\lambda^T M \lambda \\ &= -m|\lambda|^2 \end{aligned} \tag{6.4}$$

where $m = m(t)$ is the aforementioned repeated eigenvalue of the matrix $M(t)$. Therefore, the equilibration rate to leading order is given by the eigenvalue of the matrix $M(t)$. To reduce this to a single number, we use the longtime value of m.

Figure 6.8 plots the value $m(5000)$ as we vary the value of the inverse temperature β. In it we see the standard thermodynamic trend of increased equilibration rate as β decreases, that is, as the “temperature” rises. This says that the equilibration rate rises as the vortex cloud becomes more concentrated. In fact, our numerical results here suggest that the equilibration rate goes to infinity as β approaches -8π, which is the smallest allowed value. Since the equilibrium distribution becomes more and more concentrated as β decreases, the distribution looks more and more like a point vortex with a small amount of vorticity far from the center to satisfy the angular impulse constraint. It follows that for these β values, the distribution creates larger shearing flow in the immediate area of the core. This spreads out the outer vortices more quickly and so symmetrizes faster. Ultimately, in the limit $\beta \to -8\pi$, the distribution collapses completely to a point vortex and the relaxation is “instantaneous”.

At the other extreme, as $\beta \to \infty$, the vorticity distribution becomes a uniform circular patch whose radius is determined by the angular impulse constraint. In this case our numerical results predict that the vorticity distribution does not symmetrize at all as the equilibration rate drops to zero. The closure here is predicting that uniform vorticity patches can persist under the Euler equation not simply as circular patches, which is required by the equilibrium theory, but also as elliptical patches. This is a previously known classical phenomena called a Kirchoff ellipse [43].

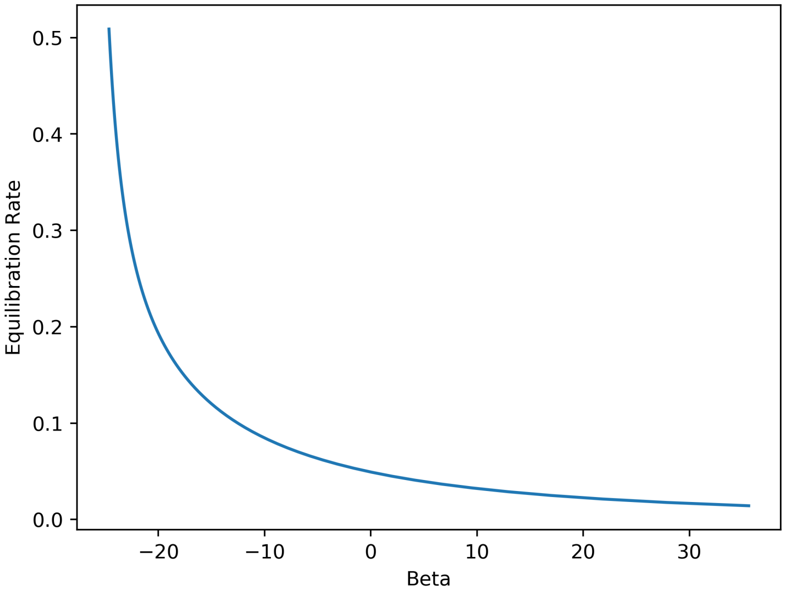

Figure 6.8: Predicted equilibration rate as a function of β. The equilibration increases as β decreases and goes to zero as β increases. In terms of the equilibrium distribution, this means that vortex clouds symmetrize faster when the center is more concentrated and symmetrize more slowly as the vortex cloud becomes more uniform. In the limit $\beta \to \infty$, the closure predicst the equilibration rate goes to zero, thus predicting the Kirchoff ellipse.

CHAPTER 7

SINGLE-LAYER QUASIGEOSTROPHIC DYNAMICS

Much of the interest in two-dimensional turbulence and coherent vorticity structures is motivated by geophysical fluid dynamics [48]. In this particular subdivision of fluid dynamics, the fluids (either the atmosphere or ocean) are extremely shallow when compared to horizontal length scales. Furthermore, the rotation of planetary bodies tends to inhibit vertical fluid flow. The combination of these two facts means that atmospheres and oceans may be treated effectively as two-dimensional or with a minimal acknowledgement of vertical variations (see chapter 9). Combine this with seemingly ubiquitous persistent geophysical vorticity structures–Jupiter's Great Red Spot [57], cyclones and anticyclones in the Earth's atmosphere and jets in the ocean such as the gulf stream [45]–and the reason for the interest of the geophysical fluids community becomes apparent.

The quasigeostrophic equation is an important part of these studies [48]. It captures the nearly geostrophic regime where planetary rotation dominates and filters out the "fast" ageostrophic motions like inertia-gravity waves. Many of the large scale coherent vorticity structures fall in this regime. The quasigeostrophic equation also brings to light the importance of potential vorticity since the equation may be viewed as a direct consequence of the conservation of potential vorticity. In the nearly geostrophic regime, the potential vorticity distribution, just like vorticity for the two-dimensional Euler equation, completely determines the dynamics.

In this chapter, we first reduce the equations for fluid flow on a rotating surface to the rotating shallow-water equations. In doing so, we come across the important notion of hydrostatic balance and the aforementioned key quantity potential vorticity. In the second section, we derive the single-layer quasigeostrophic equation from the rotating shallow-water equation as well as discussing its relation to potential vorticity conservation. Then we introduce another simplifying assumption called the rigid lid approximation which corresponds to forcing the free surface of the fluid to remain flat. We end this section with a brief discussion of the conserved quantities of the quasigeostrophic equation. For these two sections, we drew the material from the excellent books by Salmon [48] and Vallis [60]. The final section of the chapter covers the point vortex idealization in the context of the quasigeostrophic equation as well as the resulting equilibrium statistical mechanics. We find that these both greatly resemble the case of the two-dimensional Euler equation.

7.1 Rotating Shallow-Water Equations

The complete equations of motion of a rotating fluid on a planetary body are rarely used as a model. The most general of the so-called primitive equations (which use shallowness in a continuously stratified fluid layer) of practical use are the rotating shallow-water equations. In what follows, we discuss the approximations needed to reduce the general rotating fluid equations to the rotating shallow-water equations and and the conditions under which these approximations are valid. To simplify the discussion, we will assume that the fluid has constant density. In the language of geophysical fluids, we assume that the fluid is a single homogeneous layer. We also introduce the potential vorticity which is a key conserved quantity of the rotating shallow-water equations. The potential vorticity governs the large scale behavior of the fluid and is a key step on our route to the quasigeostrophic equation.

7.1.1 Equations of a Rotating Fluid

Consider a constant density inviscid fluid on the surface of the Earth. (What follows actually applies to any rotating spherical body but we will limit ourselves to the Earth for simplicity of language.) For coordinates (x', y', z'), we fix the origin at the center of the Earth and the z'-axis so it coincides with the axis of rotation. We fix the x' and y' axes so they form a right-handed coordinate system with the z' axis and we allow the coordinate frame to rotate with the Earth. In this system, the equations of motion of the fluid are

$$\frac{D\mathbf{v}}{Dt} + 2\mathbf{\Omega} \times \mathbf{v} = \frac{1}{\rho_0}\nabla p - \nabla\Phi, \tag{7.1a}$$

$$\nabla \cdot \mathbf{v} = 0, \tag{7.1b}$$

where $\mathbf{v}$ is the fluid velocity field, D/Dt denotes the material derivative and is given by

$$\frac{D}{Dt} = \partial_t + \mathbf{v} \cdot \nabla,$$

$\mathbf{\Omega}$ is the Earth's rotation vector, ρ_0 is the fluid density, p is the pressure field and Φ is the geopotential. The geopotential accounts for the centrifugal acceleration due to the rotation of the Earth and gravitational forces. In this light, it can be written as

$$\Phi = \phi + \phi_c,$$

where ϕ is the gravitational potential of the Earth and ϕ_c is the "centrifugal" potential given by

$$\phi_c = -\frac{1}{2}r_\perp^2\Omega^2,$$

where $r_\perp$ is the perpendicular distance to the Earth's rotation axis. It follows that for the position vector $\mathbf{r}$, we have

$$\nabla\phi_c = \mathbf{\Omega} \times (\mathbf{\Omega} \times \mathbf{r})$$

which is the centrifugal force, hence the name centrifugal potential. Comparing this to (2.1), we see that these are the Euler equations modified to model a rotating fluid in a gravitational field. The term $\Omega \times \mathbf{v}$ is an additional advective term due the rotating coordinate frame.

7.1.2 Derivation of Rotating Shallow-Water Equations

The system (7.1) is somewhat cumbersome to work with and most of the time is more exacting than necessary. As a result, we seek to simplify these equations with some appropriate approximations. The result will be the rotating shallow-water equations.

Our first assumption is that we consider length scales on the surface of the Earth where the curvature is not significant. Under this assumption, we can make a change of coordinates to a system based on the plane tangent to some point on the Earth's surface. We take this point to be the origin and allow the coordinates to rotate with the Earth. We choose the axes so that at the origin, the positive x-axis coincides with East, the positive y-axis coincides with North and the z-axis coincides with the radial vector emanating from the center of the Earth.

In these coordinates, we can assume a uniform gravitational field so that the gravitational potential is given by $\phi = (0, 0, -gz)$. Taking $\mathbf{v} = (u, v, w)$ and $\mathbf{\Omega} = (0, \Omega_h, \Omega_v)$, we can write (7.1) as

$$\frac{Du}{Dt} - 2\Omega_v v + 2\Omega_h w = \frac{1}{\rho_0}\partial_x p, \tag{7.2a}$$

$$\frac{Dv}{Dt} + 2\Omega_v u = -\frac{1}{\rho_0}\partial_y p, \tag{7.2b}$$

$$\frac{Dw}{Dt} - 2\Omega_h u = -\frac{1}{\rho_0}\partial_z p - g, \tag{7.2c}$$

$$\nabla \cdot \mathbf{v} = 0. \tag{7.2d}$$

The "traditional approximation" neglects the horizontal component of the rotation vector, that is, we set $\Omega_h = 0$. We will justify this assumption with a scaling argument later.

The remaining rotation vector term, $f = 2\Omega_v$, is called the Coriolis parameter. Our scaling assumption allows us to simplify this term as well. Using Taylor's theorem and expanding f, we can write

$$f \approx f_0 + \beta y, \tag{7.3}$$

where we have retained only the first two terms. This is called the beta-plane approximation. It is important to note that this β is different than the inverse temperature β that was introduced in chapter 3.

Sometimes even this approximation is more than required. In this case one can use the f-plane approximation which keeps only the first term in the Taylor expansion, that is

$$f \approx f_0. \tag{7.4}$$

Applying the traditional approximation and the beta-plane approximation (or f-plane approximation) to the system (7.2) gives us

$$\frac{Du}{Dt} - fv = -\frac{1}{\rho_0}\partial_x p, \tag{7.5a}$$

$$\frac{Dv}{Dt} + fu = -\frac{1}{\rho_0}\partial_y p, \tag{7.5b}$$

$$\frac{Dw}{Dt} = -\frac{1}{\rho_0}\partial_z p - g, \tag{7.5c}$$

$$\nabla \cdot \mathbf{v} = 0. \tag{7.5d}$$

We have left the term Coriolis parameter as the general value f but we will assume that it is given by either (7.3) or (7.4).

We now assume that the vertical component of acceleration Dw/Dt is practically zero and we can drop it in equation (7.5c) to get the relation

$$\partial_z p = -\rho_0 g. \tag{7.6}$$

This is called hydrostatic balance, and physically, it says that the vertical variation in pressure is due only to the weight of the fluid above. Because we have assumed the fluid density is constant, we can say more. If we let the free surface of the fluid be given by $z = \eta(x, y, t)$, then integrating from the surface, where we assume that the pressure is zero, to some point in the fluid, we find that (7.6) gives us

$$p(x, y, z, t) = g\rho_0(\eta(x, y, t) - z). \tag{7.7}$$

Therefore the pressure gradient is independent of z and we conclude that the horizontal flow is also independent of z—that is our fluid moves in columns.

If we are in a regime where hydrostatic balance is approximately satisfied, then we may simplify our equations. So we want to establish under what condition we may neglect the vertical component of acceleration so that equation (7.6) is a sound approximation of (7.5c). This condition can be derived through scale analysis. Let U be the typical horizontal flow, L the horizontal length scale, W the typical vertical flow and H the typical vertical length scale. We assume that the typical time scale is $T = L/U$. Under this scaling, the incompressibility condition (7.5d) gives us the relation

$$W = \frac{H}{L}U.$$

This means that

$$\frac{Dw}{Dt} \sim \frac{HU^2}{L^2},$$

where $\sim$ means scales like.

We now write the pressure as $p = g\rho_0 \cdot (\eta - z) + \rho_0 \cdot \tilde{p}$, so that $\tilde{p}$ gives the nonhydrostatic part of the pressure. Using this, equation (7.5c) reduces to

$$\frac{Dw}{Dt} = -\frac{1}{\rho_0}\partial_z[g\rho_0(\eta - z) + \rho_0 \cdot \tilde{p}] - g = -\partial_z \tilde{p}.$$

Therefore, we can regard $\tilde{p}$ as the pressure arising from the changing vertical velocity. Substituting our expression for p, we can rewrite either horizontal flow equation, say (7.5a), as

$$\frac{Du}{Dt} - fv = -g\partial_x \eta - \partial_x \tilde{p}.$$

Then, ignoring f, we have the scaling

$$\partial_x \tilde{p} \sim \frac{H}{L}\partial_z \tilde{p} \sim \frac{H}{L}\frac{Dw}{Dt} \sim \frac{H^2U^2}{L^3}.$$

Since $\frac{Du}{Dt}$ (or $\frac{Dv}{Dt}$) scale like U^2/L, we see that

$$\frac{\partial_x \tilde{p}}{\frac{Du}{Dt}} \sim \frac{H^2U^2}{L^3} \cdot \frac{U^2}{L} = \frac{H^2}{L^2}$$

and we conclude that the nonhydrostatic pressure $\tilde{p}$ is unimportant to the horizontal flow when

$$H^2/L^2 << 1. \tag{7.8}$$

Therefore, we may use the hydrostatic approximation when the fluid depth is small when in comparison to the horizontal length scale, that is, when the fluid is shallow.

We can also now justify our use of the traditional approximation. Since $W << U$ as a result of (7.8), we find that $|\Omega_h w| << |\Omega_v v|$ so that this term can be dropped. This leaves the $\Omega_h u$ term which we must show does not prevent our neglect of the $\tilde{p}$ terms (recall that this was the nonhydrostatic variations in the pressure). If

$$2\Omega_h u = \frac{\partial \tilde{p}}{\partial z},$$

then

$$\tilde{p} \sim \Omega U H$$

so that

$$\partial_x \tilde{p} \sim \frac{\Omega U H}{L}.$$

This is negligible compared to the remaining Coriolis term $2\Omega_v u$, which scales like ΩU, if $H << L$.

Assuming the shallowness condition (7.8) so that p is given by (7.7), equations (7.5a) and (7.5b) can be compactly written as

$$\frac{D\mathbf{u}}{Dt} + \mathbf{f} \times \mathbf{u} = -g\nabla\eta, \tag{7.9}$$

where we have introduced the two-dimensional horizontal velocity field $\mathbf{u} = (u, v, 0)$, the two-dimensional gradient operator $\nabla = (\partial_x, \partial_y, 0)$ and the rotation vector $\mathbf{f} = (0, 0, f)$, where f is given by the beta-plane or f-plane approximation of the Coriolis parameter.

We can also rewrite the incompressibility condition (7.5d). Rearranging terms gives us

$$\frac{\partial w}{\partial z} = -\nabla \cdot \mathbf{u}.$$

Let the bottom be given by $z = -\eta_b(x, y)$. Then integrating from the top of the fluid to the bottom and noting that the right hand side is independent of z, we get the relation

$$w(\eta) - w(-\eta_b) = -(\eta + \eta_b)\nabla \cdot \mathbf{u}.$$

Since the vertical velocity at the surface is the material derivative of the position and the position is given by η, we have that $w(\eta) = \frac{D\eta}{Dt}$. Similarly, at the bottom $w(-\eta_b) = -\frac{D\eta_b}{Dt}$. Therefore, the above equation reduces to

$$\frac{D}{Dt}(\eta + \eta_b) + (\eta + \eta_b)\nabla \cdot \mathbf{u} = 0, \tag{7.10}$$

which can also be written

$$\frac{\partial(\eta + \eta_b)}{\partial t} + \nabla \cdot (\mathbf{u}(\eta + \eta_b)) = 0. \tag{7.11}$$

We can rewrite this equation more compactly, by defining $h(x, y, t) = \eta(x, y, t) + \eta_b(x, y)$. Then (7.9) together with (7.10) and rewriting in terms of h, give us the system of equations

$$\frac{D\mathbf{u}}{Dt} + \mathbf{f} \times \mathbf{u} = -g\nabla\eta, \tag{7.12a}$$

$$\frac{Dh}{Dt} + h\nabla \cdot \mathbf{u} = 0. \tag{7.12b}$$

These are (at long last) the rotating shallow-water equations. They are a complete set of equations in the three variables $u(x, y, t)$, $v(x, y, t)$ and $\eta(x, y, t)$.

7.1.3 Potential Vorticity

We now define the potential vorticity and show it is conserved. We also examine the physical meaning of potential vorticity conservation.

Define the relative vorticity $\zeta = \nabla \times \mathbf{u}$. Just as in the Euler equations, this is a vector quantity but only the vertical component is nonzero so we may treat it as a scalar value (in fact, the relative vorticity is the vorticity from the Euler equations). Taking the curl of the momentum equation (7.12a), gives us

$$\frac{D}{Dt}(\zeta + f) + (\zeta + f)(\nabla \cdot \mathbf{u}) = 0. \tag{7.13}$$

The quantity $\zeta + f$ is known as the absolute vorticity. Rearranging equation (7.12b), we have

$$\nabla \cdot \mathbf{u} = -\frac{1}{h}\frac{Dh}{Dt},$$

which upon plugging into (7.13) and multiplying by h^3 gives us the equation

$$\frac{h\frac{D}{Dt}(\zeta + f) - \frac{Dh}{Dt}(\zeta + f)}{h^2} = 0.$$

Recognizing the quotient rule, we have the equation

$$\frac{D}{Dt}\left(\frac{\zeta + f}{h}\right) = 0. \tag{7.14}$$

The quantity $(\zeta + f)/h$ is called the potential vorticity and equation (7.14) is known as the conservation of potential vorticity.

To understand the physical meaning of this equation, we consider an arbitrary volume of fluid, and we follow its advection. Equation (7.14) tells us that the ratio $(\zeta + f)/h$ is constant or $(\zeta + f) \propto h$. Therefore, if the absolute vorticity increases, the depth of the fluid must also increase. Conversely, decreasing the vorticity causes a decrease in the height of the free surface.

The conservation of potential vorticity can be viewed as the rotating shallow-water equivalent of the conservation of vorticity in the Euler equations as expressed by equation (2.4a). Just as vorticity conservation has major effects on two-dimensional turbulence, potential vorticity conservation plays a profound role in rotating shallow-water dynamics. We will see that it governs much of the large scale motion.

7.2 Quasigeostrophic Equation

We have seen that the shallow-water equations are the result of hydrostatic balance. We will now see that when the Coriolis forces are greater in magnitude than the horizontal acceleration terms, we get a new regime called geostrophic balance which allows us to simplify the shallow-water equations even further. When we are close to this regime, as expressed by the Rossby number, the result is the (single-layer) quasigeostrophic equation.

7.2.1 Geostrophic Balance

Return momentarily to equations (7.5a) and (7.5b), which we recall here in vector form for convenience,

$$\partial_t \mathbf{u} + \mathbf{v} \cdot \nabla \mathbf{u} - \mathbf{f} \times \mathbf{u} = -\frac{1}{\rho_0} \nabla p.$$

Again, we let $\mathbf{u} \sim U$ and $(x, y) \sim L$. In this case then the advective term scales like U^2/L and the Coriolis term scales like fU. Taking the ratio of the advective term to the Coriolis term results in the dimensionless ratio known as the Rossby number

$$Ro = \frac{U}{fL}. \tag{7.15}$$

If the Rossby number is small, then the rotational term dominates the flow. If the Rossby number is large, then the flow acceleration term dominates. Therefore, the Rossby number expresses the importance of rotation.

We can also view the Rossby number as a comparison of time scales. Assume that the characteristic time of the dynamics scales like T (so $L/U = T$). Since f is an angular velocity, $T_i = 1/f$ defines a time scale, called the inertial timescale, where we have ignored the factor of 2π. Then we can write the Rossby number as

$$Ro = \frac{U}{L} \cdot \frac{1}{f} = \frac{1}{T} \cdot T_i.$$

From this perspective, we see that short lived phenomenon ($T << T_i$) like cumulus clouds or tornados will have a large Rossby number and will largely be unaffected by the rotation of the Earth. (In particular, this means that the direction the water in the sink or the toilet spins, contrary to popular belief, is in no way related to the spin of the Earth.) Phenomenon with larger time scales ($T >> T_i$) have small Rossby numbers and are greatly influenced by the Earth's rotation. This includes phenomena like the jet stream.

We now examine the case when the Rossby number is identically zero so that the change in the flow $\mathbf{v}$ is negligible when compared to the Coriolis forces. Alternatively, we can say that the time scale on which the flow changes is infinite. In this case, the horizontal momentum equations (7.5a) and (7.5b) become the time-independent equations

$$-fv = -\frac{1}{\rho_0}\partial_x p, \tag{7.16a}$$

$$fu = -\frac{1}{\rho_0}\partial_y p. \tag{7.16b}$$

This is called geostrophic balance and we define the geostrophic flow field $\mathbf{u}_g = (u_g, v_g, 0)$ to be the flow that satisfies equations (7.16). In this stationary regime, the flow and surface η are such that they balance the rotation of the Earth.

It is worth noting that in the near geostrophic regime, we can relax the shallow fluid condition (7.8) and retain our hydrostatic approximation. The reason is that in this regime our estimate of the scale of the vertical velocity was too great. Let H again denote the characteristic depth of the fluid and let $p = g\rho_0(\eta - z) + \rho_0\tilde{p}$. Then cross differentiating (7.5a) and (7.5b) and subtracting tells us that

$$\nabla \cdot \mathbf{u} = \frac{1}{f}\frac{D}{Dt}(\nabla \cdot \mathbf{u}).$$

It follows that the characteristic vertical velocity W scales not as HU/L but as

$$W \sim H(\nabla \cdot \mathbf{u}) \sim \frac{H}{f}\frac{D}{Dt}(\nabla \cdot \mathbf{u}) \sim \frac{H}{f} \cdot \frac{U^2}{L^2} = Ro \cdot \frac{HU}{L}$$

so our previous estimate was off by a factor of the Rossby number. Repeating our previous analysis then tells us that

$$\frac{\nabla\tilde{p}}{\frac{D\mathbf{u}}{Dt}} \sim Ro\frac{H^2}{L^2}$$

so that our hydrostatic assumption is valid under the weaker condition

$$Ro\frac{H^2}{L^2} << 1. \tag{7.17}$$

7.2.2 Derivation of Single-Layer Quasigeostrophic Equations

We return now to the shallow-water equations and assume that we are nearly geostrophic—that is, we assume that Ro is small. We use this assumption and a few geometric requirements to derive the quasigeostrophic equation.

Explicitly using the beta approximation $f = f_0 + \beta y$ in equations (7.12) gives us

$$\frac{D\mathbf{u}}{Dt} + (f_0 + \beta y)\mathbf{k} \times \mathbf{u} = -g\nabla\eta, \tag{7.18a}$$

$$\partial_t h + \nabla \cdot (h\mathbf{u}) = 0, \tag{7.18b}$$

where $\mathbf{k}$ is the vertical unit vector. Non-dimensionalizing (7.12) in this regime yields the equations

$$Ro\frac{D\mathbf{u}}{Dt} + (1 + \beta' y)\mathbf{k} \times \mathbf{u} = -\nabla\eta, \tag{7.19a}$$

$$Ro[\partial_t \eta + \nabla \cdot (\eta\mathbf{u})] + B\nabla \cdot [\mathbf{u}(1 - \delta)] = 0, \tag{7.19b}$$

where we have introduced the fractional bottom elevation

$$\delta = \frac{H - \eta_b(x, y)}{H},$$

the dimensionless parameter known as the Burger number

$$B = \frac{gH}{f_0^2 L^2},$$

and the nondimensional version of β

$$\beta' = \frac{\beta L}{f_0}.$$

Furthermore, all variables and derivatives are now dimensionless and assumed to be of order one.

Note that the Burger number is a comparison of length scales. If we write

$$B = \frac{gH}{f_0^2} \cdot \frac{1}{L^2},$$

we are led to introduce the length scale quantity

$$R_d = \frac{\sqrt{gH}}{f_0}$$

so that $B = R_d^2/L^2$. The length scale R_d is called the external Rossby deformation radius (often shortened to simply the deformation radius). The importance of the deformation radius will be discussed later, after we have derived the single-layer quasigeostrophic equation.

In addition to our assumption that $Ro << 1$, we also assume that $\beta' << 1$ (this is really our assumption that we are working in small enough length scales that the curvature of the Earth is not important), that $\delta << 1$ (so the bottom does not have significant variations from the typical depth H), that B is order one (so our typical length scale L is roughly the same size as the deformation radius R_d) and finally that β' and δ are of the same order as Ro so that we can write $\beta' = \hat{\beta} \cdot Ro$ and $\delta = \hat{\delta} \cdot Ro$ where $\hat{\beta}$ and $\hat{\delta}$ are both order one.

We seek solutions of equations (7.19) as expansions in the Rossby number

$$u = \mathbf{u}_0 + Ro \cdot \mathbf{u}_1 + Ro^2 \cdot \mathbf{u}_2 + \dots, \tag{7.20a}$$

$$\eta = \eta_0 + Ro \cdot \eta_1 + Ro^2 \cdot \eta_2 + \dots. \tag{7.20b}$$

Now we plug expansions (7.20) into the system (7.19) and equate orders of Ro. From the momentum equation (7.19a), we get

$$O(1): \quad \mathbf{k} \times \mathbf{u}_0 = -\nabla \eta_0, \tag{7.21a}$$

$$O(Ro): \quad \partial_t \mathbf{u}_0 + \mathbf{u}_0 \cdot \nabla \mathbf{u}_0 + \hat{\beta} y (\mathbf{k} \times \mathbf{u}_0) + \mathbf{k} \times \mathbf{u}_1 = -\nabla \eta_1, \tag{7.21b}$$

and from the surface equation (7.19b), we get

$$O(1): \quad B \nabla \cdot \mathbf{u}_0 = 0, \tag{7.22a}$$

$$O(Ro): \quad \partial_t \eta_0 + \mathbf{u}_0 \cdot \nabla \eta_0 + B \nabla \cdot \mathbf{u}_1 - B \mathbf{u}_0 \cdot \nabla \hat{\delta} = 0. \tag{7.22b}$$

Writing (7.21a) in component form and cross differentiating gives us the horizontal incompressibility condition

$$\nabla \cdot \mathbf{u}_0 = 0,$$

which is identical to (7.22a). This leaves us unable to determine the variables $\mathbf{u}_0$ and η_0, that is, the order one equations are not closed. Therefore, we must look to the first order equations.

Taking the curl of (7.21b) and rearranging gives us

$$\partial_t \zeta_0 + \mathbf{u}_0 \cdot \nabla(\zeta_0 + \hat{\beta} y) = -\nabla \cdot \mathbf{u}_1$$

where $\zeta_0 = \nabla \times \mathbf{u}_0$. To eliminate the $\mathbf{u}_1$ term in the above, we solve (7.22b) for $\nabla \cdot \mathbf{u}_1$ and substitute to get

$$\partial_t \zeta_0 + \mathbf{u}_0 \cdot \nabla(\zeta_0 + \hat{\beta} y) = \frac{1}{B}(\partial_t \eta_0 + \mathbf{u}_0 \cdot \nabla \eta_0 - B\mathbf{u}_0 \cdot \nabla \hat{\delta}).$$

Upon rearranging we have

$$\partial_t \left(\zeta_0 + \hat{\beta} y - \frac{1}{B}\eta_0 + \hat{\delta} \right) + \mathbf{u}_0 \cdot \nabla \left(\zeta_0 + \hat{\beta} y - \frac{1}{B}\eta_0 + \hat{\delta} \right) = 0.$$

Just as with the Euler equations, we can use the incompressibility condition $\nabla \cdot \mathbf{u}_0 = 0$ to introduce a stream function ψ_0 so that

$$\mathbf{u}_0 = \nabla^\perp \psi_0 = (\partial_y \psi_0, -\partial_x \psi_0).$$

Combining this relation with the definition of ζ_0, we get the relation

$$-\Delta \psi_0 = \zeta_0.$$

We also note that (7.21a) implies that $\eta_0 = -\psi_0$. In geophysical fluid dynamics it is standard to take the sign of the stream function so that $\eta_0 = \psi_0$. We have introduced the negative to be consistent with our formulation of the Euler equations.

Again, adopting the notation

$$[A, B] = \frac{\partial A}{\partial x}\frac{\partial B}{\partial y} - \frac{\partial A}{\partial y}\frac{\partial B}{\partial x},$$

we arrive at the equation

$$\partial_t \left(-\Delta\psi_0 + \hat{\beta} y + \frac{1}{B}\psi_0 + \hat{\delta} \right) + \left[-\Delta\psi_0 + \hat{\beta} y + \frac{1}{B}\psi_0 + \hat{\delta}, \psi_0 \right] = 0 \tag{7.23}$$

or, equivalently, the system

$$\begin{aligned} &\partial_t q_0 + [q_0, \psi_0] = 0, \\ &q_0 = -\Delta\psi_0 + \hat{\beta} y + \frac{1}{B}\psi_0 + \hat{\delta}. \end{aligned}$$

Restoring the dimensions (or taking L and U to be unity) and dropping the subscripts, we arrive at the single-layer quasigeostrophic equations

$$\partial_t q + [q, \psi] = 0, \tag{7.24a}$$

$$q = -\Delta\psi + \beta y + \frac{1}{R_d^2}\psi + f_0\delta, \tag{7.24b}$$

where $\psi = -(g/f_0)\eta$ and $R_d = \sqrt{gH}/f_0$ is, as previously introduced, the external Rossby deformation radius.

If we use the f plane approximation, that is, we take $\beta = 0$, and consider the special case of a flat bottom, that is, $\delta = 0$, we get the equations

$$\partial_t q + [q, \psi] = 0, \tag{7.25a}$$

$$-\Delta\psi + \frac{1}{R_d^2}\psi = q. \tag{7.25b}$$

Comparing this to the Euler equations given by (2.1), we see that the only difference is the term in (7.25b) with the deformation radius. We will exploit this similarity to apply our previous theory, the point vortex idealization as well as both the equilibrium and nonequilibrium statistical theories, with only minor modifications.

7.2.3 Relation to Potential Vorticity

There is an important connection between potential vorticity and the quasigeostrophic equation. To explore this connection, recall the potential vorticity

$$Q = \frac{\zeta + f}{h}$$

as well as our three assumptions that $Ro << 1$, $\beta L/f_0 << 1$ and $(h-H)/H << 1$. Using the third assumption, we have

$$Q = \frac{\zeta + f}{H(1 + \frac{h-H}{H})} \approx \frac{1}{H} \cdot (\zeta + f)\left(1 - \frac{h-H}{H}\right) = \frac{1}{H}(\zeta + f)\left(1 - \frac{\eta}{H} + \delta\right),$$

where we have used the fact that

$$\frac{h-H}{H} = \frac{\eta + \eta_b - H}{H} = \frac{\eta}{H} - \delta.$$

Now since the Rossby number is small and β is small compared to f_0, we know that we are near geostrophic balance so that

$$f\mathbf{k} \times \mathbf{u} \approx f_0 \mathbf{k} \times \mathbf{u} \approx -g\nabla\eta.$$

It follows that $\nabla \cdot \mathbf{u} \approx 0$ and that there is a stream function ψ such that

$$\psi = -\frac{g\eta}{f_0}$$

and

$$-\Delta\psi = \zeta.$$

Using the stream function in place of η in the above approximation of the potential vorticity and using the beta-plane approximation gives us

$$\begin{aligned} Q &\approx \frac{f_0}{H}\left(1+\frac{\beta y}{f_0}-\frac{\Delta\psi}{f_0}\right)\left(1+\frac{f_0\psi}{gH}+\delta\right) \\ &\approx \frac{f_0}{H}\left(1-\frac{\Delta\psi}{f_0}+\frac{\beta y}{f_0}+\frac{f_0\psi}{gH}+\delta\right). \end{aligned}$$

We now recognize that

$$Q \approx \frac{1}{H}q+\frac{f_0}{H},$$

where q is defined by (7.24b). Since Q is materially conserved, we have

$$\frac{D}{Dt}\left(\frac{q}{H}+\frac{f_0}{H}\right)=\frac{1}{H}\frac{Dq}{Dt}\approx\frac{DQ}{Dt}=0,$$

which simplifies to (7.24a). Therefore, we can view the single-layer quasigeostrophic equation as the result of the potential vorticity conservation of the rotating shallow-water equations.

7.2.4 Rigid-Lid Approximation

In order to gain insight into the physical meaning of the deformation radius and explore how the single-layer quasigeostrophic equations relate to the Euler equations, we now consider the case where the typical length scale L is much smaller than the deformation radius R_d. This amounts to setting R_d to infinity.

Looking at quasigeostrophic vorticity (7.24b), we compare the magnitude of two terms containing the stream function and find that

$$\Delta\psi \sim \frac{\psi}{L^2} >> \frac{\psi}{R_d^2}.$$

Since $R_d << L$, we may neglect the term ψ/R_d^2 to get the approximation

$$q \approx -\Delta\psi+\beta y+f_0\delta.$$

Recalling from the derivation of the quasigeostrophic equations (or the discussion of the relation to potential vorticity) that

$$\frac{1}{R_d^2}\psi = \frac{f_0^2}{gH}\psi = -\frac{f_0}{H}\eta,$$

we see that the term with the deformation radius arises from the changes in the free surface η. Therefore, the assumption of an infinite deformation radius is equivalent to assuming a rigid or flat surface. In terms of our variables, we assume that $\eta = 0$ for all time. This is the reason for the name rigid-lid approximation. Physically, this tells us that R_d gives the minimal length scale on which the free surface deforms.

There is one more important point to make in this regime. If we assume that the bottom is flat and use the f plane approximation, we arrive at (7.25b). Setting the deformation radius to infinity here results in the system of equations

$$\begin{aligned} &\partial_t q + [q, \psi] = 0, \\ &-\Delta\psi = q. \end{aligned}$$

These are the Euler equations given by (2.4) with q in place of ζ. Therefore, in this special case, we see that the quasigeostrophic equations present themselves as a modified (or more general) version of the Euler equations.

7.2.5 Conserved Quantities

As we saw when discussing the point vortex idealization and the equilibrium statistical mechanics for the Euler equations, conserved quantities play an important role. Here we briefly cover the quantities that are conserved by the system of equations (7.25). It should be noted that not all of these are conserved by the more general single-layer quasigeostrophic equations (7.24).

Just as with the Euler equations, the equation (7.25a) implies that the total vorticity, given by

$$\Gamma = \int_{\mathbb{R}^2} q \, d\mathbf{x}, \tag{7.26}$$

is a conserved quantity. This is just the quantity (2.5) with ζ replaced by q.

If we consider the system (7.25) on the plane, then we have the same translational and rotational symmetries as the Euler equations. Therefore, by Noether's theorem [21, 34], the center of vorticity

$$\mathbf{B} = \int_{\mathbb{R}^2} \mathbf{x} \cdot q \, d\mathbf{x} \tag{7.27}$$

and the angular impulse

$$L^2 = \int_{\mathbb{R}^2} |\mathbf{x}|^2 \cdot q \, d\mathbf{x} \tag{7.28}$$

are conserved. These are just the quantities (2.7) and (2.8), respectively, with ζ replaced by q.

Finally, the energy

$$E = \frac{1}{2} \int_{\mathbb{R}^2} \psi \cdot q \, d\mathbf{x} \tag{7.29}$$

is also conserved. Unsurprisingly, this is just (2.6) with q replacing ζ. Note, however, in this case we have $|\psi| \to 0$ as $|\mathbf{x}| \to \infty$. This results from the Green's function (7.31) and the fact that the total vorticity is finite. Then using (7.25b) and Green's first identity that we can express (7.29) as

$$E = \frac{1}{2} \int_{\mathbb{R}^2} |\nabla\psi|^2 \, d\mathbf{x} + \frac{1}{2R_d^2} \int_{\mathbb{R}^2} \psi^2 \, d\mathbf{x}. \tag{7.30}$$

This is clearly the sum of the kinetic energy (first term) and potential energy (second term).

Just as with the Euler equations, the generalized enstrophy

$$\int_{\mathbb{R}^2} f(q) \, d\mathbf{x}$$

is conserved for f sufficiently smooth. This is again named after the enstrophy which we get when $f(q) = q^2$.

7.3 Point-Vortex Idealization

Here we explore how the addition of the deformation radius affects the dynamics of the point vortex idealization and the corresponding equilibrium statistical mechanics. We limit ourselves to the special case given by (7.25) rather than the more general (7.24). In particular, we see that the changes from the Euler equations are minimal.

7.3.1 Dynamics

The introduction of the deformation radius changes the Green's function. For (7.25b), the Green's function is given by

$$G(\mathbf{x}, \mathbf{x}') = \frac{1}{2\pi} K_0(k_d |\mathbf{x} - \mathbf{x}'|), \tag{7.31}$$

where $k_d = 1/R_d$ and K_0 is the modified Bessel function of the second kind. Therefore, for the vorticity distribution

$$q^N(\mathbf{x}) = \sum_{i=1}^{N} \gamma_i \delta_{\mathbf{x}_i}(\mathbf{x}), \tag{7.32}$$

the corresponding stream function is

$$\begin{aligned} \psi^N(\mathbf{x}, t) &= \frac{1}{2\pi} \int_{\mathbb{R}^2} K_0(k_d |\mathbf{x} - \mathbf{x}'|) q_N(\mathbf{x}', t) d\mathbf{x}' \\ &= \frac{1}{2\pi} \sum_{i=1}^{N} K_0(k_d |\mathbf{x} - \mathbf{x}_i|). \end{aligned} \tag{7.33}$$

As in the Euler case, we neglect the self-interaction term, use the stream function definition and the fact that

$$\frac{d}{dr} K_0(r) = -K_1(r)$$

to arrive at the system of ordinary differential equations

$$\dot{x}_i = -\frac{k_d}{2\pi} \sum_{j \neq i} \gamma_j \frac{(y_i - y_j)}{r_{ij}} K_1\left(k_d \cdot r_{ij}\right), \tag{7.34a}$$

$$\dot{y}_i = \frac{k_d}{2\pi} \sum_{j \neq i} \gamma_j \frac{(x_i - x_j)}{r_{ij}} K_1\left(k_d \cdot r_{ij}\right), \tag{7.34b}$$

where $r_{ij} = |\mathbf{x}_i - \mathbf{x}_j|$. This is the same as (2.14) with $K_1(r)$ replacing $1/r$.

The center of vorticity (2.16) and the angular impulse (2.17) are still conserved quantities. These are simply equations (7.27) and (7.28) where the vorticity q is given by (7.32).

The Hamiltonian (2.15) is replaced by

$$H^N(\mathbf{x}_1, \dots, \mathbf{x}_N) = \frac{1}{4\pi} \sum_{i=1}^{N} \sum_{i \neq j} \gamma_i \gamma_j K_0(k_d |\mathbf{x}_i - \mathbf{x}_j|). \tag{7.35}$$

Generally speaking, to go from the Euler equations to the single-layer equations, we replace logarithmic dependence with K_0 dependence and $1/r$ dependence with K_1 dependence. This means that we may implement the closure on the point vortex system for the single-layer equations by making minor modifications to our closure for the Euler equations.

Before we continue on to the equilibrium statistical mechanical theory, we take a moment to exam the meaning of the deformation radius from another perspective as the Green's function provides great insight. The modified Bessel function of the second kind $K_0(r)$ (roughly speaking) behaves like $-\log r$ for r small and decays exponentially for $r > 1$. The function $K_1(r)$ behaves like $1/r$ for r small and exhibits the same exponential decay for $r > 1$. (See figure 7.1 for plots that compare functions K_0 and K_1 to $-\log r$ and $1/r$.) From (7.31), we see that, the deformation radius acts as a screening distance. Specifically, when any two points are separated by a distance more than the deformation radius, that is, $|\mathbf{x} - \mathbf{x}'| > R_d$, see the exponential decay part of K_0 (or K_1). Therefore the deformation radius limits the range of effect of vorticity. In the context of point vortices, the deformation radius limits the interaction range so that a point vortex only sees other vortices that are within a distance R_d.

From this perspective, it becomes obvious that in the limit $R_d \to \infty$, we recover the Euler equations, just as discussed in the case of the rigid-lid approximation. We also see that in the limit $R_d \to 0$, we will get no motion whatsoever.

7.3.2 Equilibrium Statistical Mechanics

It is surprisingly simple to modify the system (3.7) for use with our single-layer model (7.25). Because the only difference between the two systems is the change in Green's functions, we can repeat the entire statistical mechanics arguments as given in chapter 3 to arrive at the

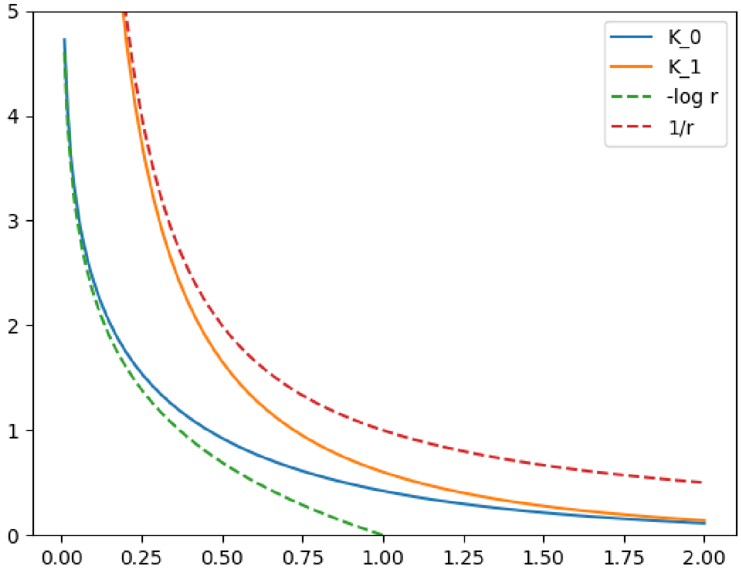

Figure 7.1: Modified Bessel functions of the second kind of order zero and one. They are asymptotically equivalent to $\log r$ and $1/r$, respectively, which is seen here. They decay exponentially starting around $r = 1$.

same variational problem (repeated here for convenience)

$$\text{minimize} \int_{\mathbb{R}^2} \rho(\mathbf{x}) \log \rho(\mathbf{x}) d\mathbf{x} \quad \text{subject to} \tag{7.36a}$$

$$\frac{1}{2} \int_{\mathbb{R}^2} \psi(\mathbf{x}) \rho(\mathbf{x}) d\mathbf{x} = E, \tag{7.36b}$$

$$\int_{\mathbb{R}^2} |\mathbf{x}|^2 \rho(\mathbf{x}) d\mathbf{x} = L^2, \tag{7.36c}$$

$$\int_{\mathbb{R}^2} \rho(\mathbf{x}) d\mathbf{x} = 1. \tag{7.36d}$$

The lone difference is that ψ solves the equation

$$-\Delta\psi + \frac{1}{R_d^2}\psi = q = \Gamma\rho.$$

We can again solve this using calculus of variations and arrive at the mean-field equations

$$q = \exp\{-\beta\psi - \alpha|\mathbf{x}|^2 - \mu\}, \tag{7.37a}$$

$$q = -\Delta\psi + \frac{1}{R_d^2}\psi, \tag{7.37b}$$

where β, α and μ are constants such that constraints (7.36b), (7.36c) and (7.36d) are satisfied. These equations describe a two parameter family of distribution in R_d and either β or the energy E.

We exploit the similarity of the single-layer equations and the Euler equations to determine that the algorithm described in section 3.3 also needs little modification. Because the only change in the mean-field equations is the change of relationship between the vorticity and stream function, we simply need to swap out our Poisson solver for something that solves (7.37b).

To get an idea of how the addition of the deformation radius affects the equilibrium distribution and stream function, figure 7.2 depicts the radial plot of the equilibrium solutions of Euler equation (or $R_d = \infty$) and the quasigeostrophic equation with $R_d = 1.0$ where both have $\beta = 6.85$. There is not a significant difference in the vorticity distribution. The center is slightly higher and the tails are slightly lighter so there is a little less vorticity at the center and more further out. This is more apparent in figure 7.3 which is a contour plot of the same two equilibrium vorticity distributions (note there is a difference in scale of the contours). The stream function seems significantly different, but the difference of a constant has no impact on the dynamics as it is the slope that is important. Note that the quasigeostrophic stream function levels off as r increase whereas the Euler equation stream function does not. This is the effect of the deformation radius. The opposite happens in the negative β states with the Euler equation being more concentrated and with a lighter tail.

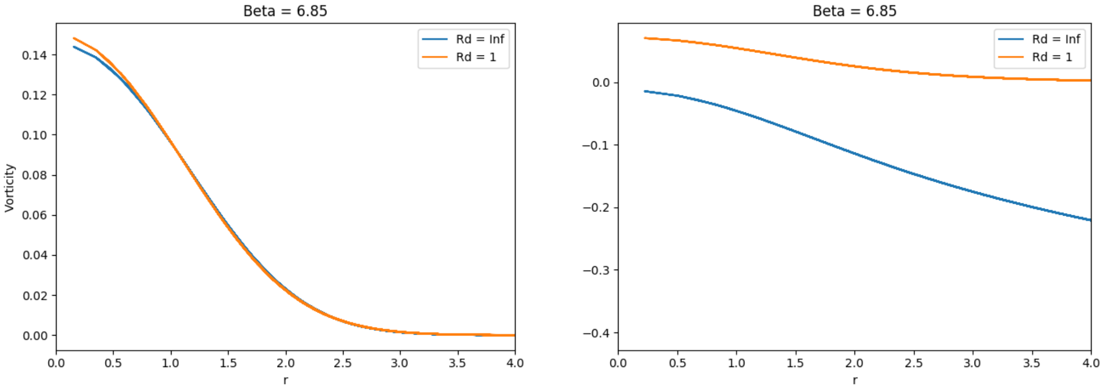

Figure 7.2: Radial plots of the equilibrium distributions and stream functions for the Euler and quasigeostrophic equations. The deformation radius is $R_d = 1.0$. The Euler equation are equivalent to $R_d = \infty$. Both have inverse temperature $\beta = 6.85$. The quasigeostrophic distribution has more vorticity at the center and less at the edge. The constant difference of the stream function has no impact on the dynamics but the quasigeostrophic stream function does level out as r increases. This is the effect of the deformation radius as the flow velocity drops to zero exponentially whereas the in the Euler case, the decay in velocity is like $1/r$.

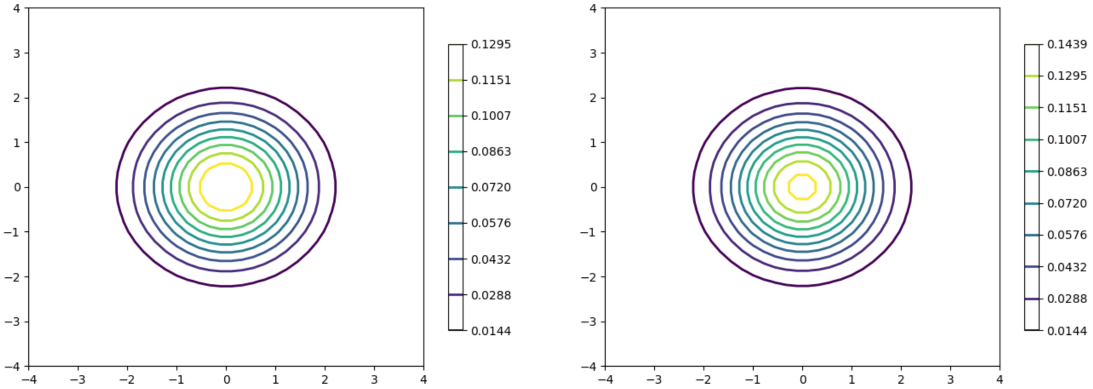

Figure 7.3: Contour plots of the equilibrium distributions for the Euler equations (left) and the quasigeostrophic equations (right). The Euler distribution is flatter at the center and more spread out (note the difference in scales) than the quasigeostrophic equation.

CHAPTER 8

SINGLE-LAYER QUASIGEOSTROPHIC OPTIMAL CLOSURE

We generalize the nonequilibrium theory we developed for the point vortex idealization of the Euler equation in chapter 5 to the single-layer quasigeostrophic equation. We then apply the theory to the same axisymmetrization problem described in chapter 6. The motivation for this problem is the same as for the Euler equation. As observed in [40], the single-layer quasigeostrophic exhibits the same emergence of coherent vortices at long time as the Euler equation and the axisymmetrization process occurs after close encounters with another vortex. Finally, we predict the rate of symmetrization as it depends on both the inverse temperature β and the deformation radius R_d.

8.1 Single-Layer Closure

Modifying our closure procedure for the single-layer model is straightforward. The mean-field reduction of the Liouville residual may be carried out in the same way from the same starting trial density (5.4) to get the implicit trial density

$$\tilde{\rho}(\mathbf{x}) = \tilde{q}(\mathbf{x}) = \exp\left\{\lambda^T \mathbf{A}(\mathbf{x}) - \beta\tilde{\psi}(\mathbf{x}) - \alpha|\mathbf{x}|^2 - \mu\right\}, \tag{8.1a}$$

$$-\Delta\tilde{\psi} + \frac{1}{R_d^2}\tilde{\psi} = \tilde{q}, \tag{8.1b}$$

$$\int_{\mathbb{R}^2} \tilde{\psi} \cdot \tilde{q}\, d\mathbf{x} = 2E, \tag{8.1c}$$

$$\int_{\mathbb{R}^2} |\mathbf{x}|^2 \tilde{q}\, d\mathbf{x} = L^2, \tag{8.1d}$$

$$\int_{\mathbb{R}^2} \tilde{\rho}\, d\mathbf{x} = 1. \tag{8.1e}$$

From here we again make a near equilibrium assumption to find that μ' is still given by (5.14), and q' must still satisfy (5.15) and (5.17). However, q' and ψ' are now related by

$$-\Delta\psi' + \frac{1}{R_d^2}\psi' = q',$$

where $\psi' \to 0$ as $|\mathbf{x}| \to \infty$. Therefore, G_{eq} is replaced by the inversion operator $G_{sl} = \left(-\Delta + \frac{1}{R_d^2} + \beta_{eq}q_{eq}\right)^{-1}$ and $P[F]$ is replaced by

$$P_{sl}[F] = F - \langle F\rangle - \beta_{eq}G_{sl}[(F - \langle F\rangle)q_{eq}].$$

It follows that α_i and β_i are still determined by (5.26) but D_1 and D_2 are now given by

$$D_1 = -\begin{pmatrix} \mathrm{Cov}\left(\psi_{eq}, P_{sl}[\psi_{eq}]\right) & \mathrm{Cov}\left(\psi_{eq}, P_{sl}[r^2]\right) \\ \mathrm{Cov}\left(r^2, P_{sl}[\psi_{eq}]\right) & \mathrm{Cov}\left(r^2, P_{sl}[r^2]\right) \end{pmatrix}, \quad D_2 = \begin{pmatrix} \mathrm{Cov}\left(\psi_{eq}, P_{sl}[\mathbf{A}^T]\right) \\ \mathrm{Cov}\left(r^2, P_{sl}[\mathbf{A}^T]\right) \end{pmatrix},$$

and the ψ_i are now given by

$$\psi_i = G_{sl}[(A_i + \alpha_i(r^2 - L^2) + \beta_i(\psi_{eq} - 2E))\rho_{eq}]. \tag{8.2}$$

These are the only differences. Everything else proceeds just as before: the Liouville residual reduces to (5.37) where $\mathbf{U}$ and $\mathbf{V}$ are still given by (5.35) and (5.36), respectively, after substituting the single-layer definitions of α_i, β_i and ψ_i. Closure is then achieved in the same manner.

8.2 Single-Layer Application and Results

We again look at the vortex cloud symmetrization problem. We use the same observables describing the orientation, $A_1 = x^2 - y^2$, and the ellipticity, $A_2 = 2xy$, of the point vortex ensemble.

Figures 8.1, 8.2, 8.3 and 8.4 give plots of several cases with similar initial conditions for $\beta \approx 0$ with deformation radii of infinity, 4.0, 2.0 and 1.0, respectively. To initialize these cases, we used the Whitaker-Turkington algorithm as described in chapter 3 with the

Observable	Deform Rad	Abs Peak Err	Rel Peak Err	Max Abs Err	Rel Err
a_1	∞	6.37047e-03	3.61181e-02	2.19530e-02	1.24465e-01
a_2	∞	8.39497e-03	6.15201e-02	1.69521e-02	8.96124e-02
a_1	4.0	2.40721e-03	6.89124e-03	5.31489e-02	1.52152e-01
a_2	4.0	3.79747e-03	1.61956e-02	6.41511e-02	1.58953e-01
a_1	2.0	5.27331e-03	3.33887e-02	4.05205e-02	2.56561e-01
a_2	2.0	3.77902e-03	4.00925e-02	4.66757e-02	2.33639e-01
a_1	1.0	5.34709e-03	3.57155e-02	3.37040e-02	2.25123e-01
a_2	1.0	1.28718e-04	1.88412e-03	2.60938e-02	1.33002e-01

Table 8.1: Absolute and relative errors of the closure compared to EDNS for the single-layer quasigeostrophic equation. All runs have the initial condition $a_1 = 0.0$ and $a_2 = 0.4$. The infinite deformation radius corresponds to the Euler equations. The relative error is quite large due to the faster rotation of the closure compared to the EDNS whereas the peak error stays roughly the same regardless of the deformation radius.

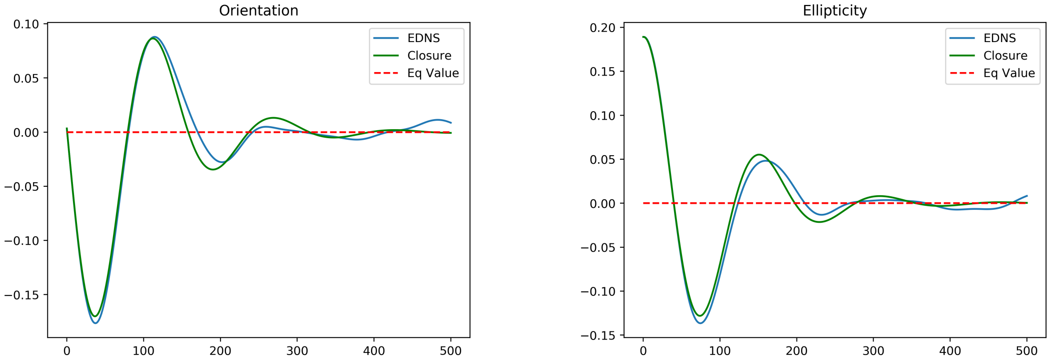

Figure 8.1: EDNS compared to optimal closure for case 1 of the single-layer quasigeostrophic equation. The initial values are $a_2 = 0.4$ and $a_1 = 0.0$ and $R_d = \infty$ which corresponds to the Euler equation. The rotation time is around 175 and both observables have mostly equilibrated by time 300.

additional constraint

$$\int_{\mathbb{R}^2} 2xy \cdot q \, dxdy = 0.40$$

to generate the distribution and sampled it through use of the CDF and random uniform sampling. Table 8.1 gives the error values discussed in section 6.2.

We again compare the optimal closure prediction to averages of vortex ensembles integrated forward in time according to the ODE system (7.34). We used the classic Runge-Kutta fourth order method with a time step of $\Delta t = 10^{-2}$ (this step size was deemed adequate again by evaluating the changes in the conserved quantities which for the most part were less than 10^{-6}). We averaged a total of 60 ensemble runs. The same caveats

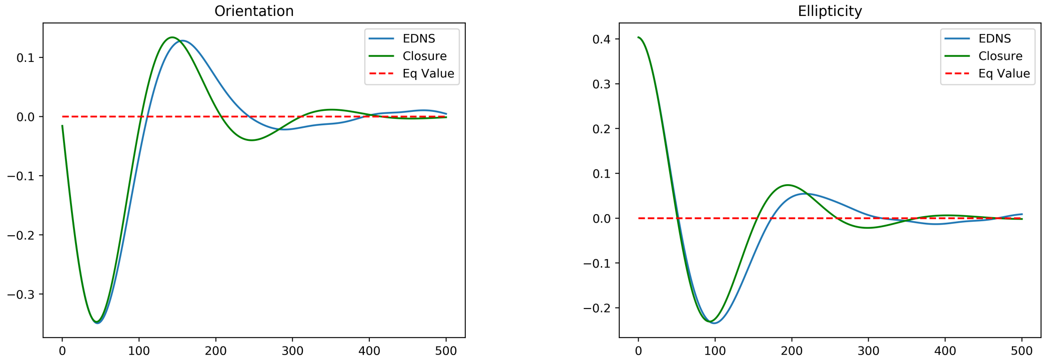

Figure 8.2: EDNS compared to optimal closure for case 2 of the single-layer quasigeostrophic equation. The initial values are $a_2 = 0.4$ and $a_1 = 0.0$ and $R_d = 4.0$. The phase difference is becoming apparent as the rotation times are roughly 200 for the closure and 230 for the EDNS. The closure captures the peak values well.

apply as when we discussed the Euler equations—because we are using a finite number of ensemble runs, the plotted curves are not the exact truth, that is, there is sampling error associated with each curve. We refer the reader back to the beginning of section 6.2 for a more thorough discussion of the implications of this and to figure 6.1 for a rough estimate of this error.

The closure captures the peaks in each case well as reflected by the peak errors. We do see an increase in the magnitude of the relative error but, from the plots, this is due to the phase difference—the closure again rotates faster than the numerical result. The decrease of the relative error in the last case is almost certainly the result of the slow rotation so that the equilibration has not completed by the end of the simulation. The most notable trend is the increase of the timescale as the deformation radius decreases. This is true both of the rotation rate and of the relaxation rate. The closure captures this dependence well.

8.3 Equilibration Rate Dependence on Parameters

As in the case of the Euler equations, we can quantify the equilibration rate, or the symmetrization rate, from the eigenvalues of the matrix M. Recall from our observables that we have a single repeated eigenvalue for M. Figure 8.5 plots of the repeated eigenvalue of M at large time ($t = 5000$) as a function of β for several different deformation radii.

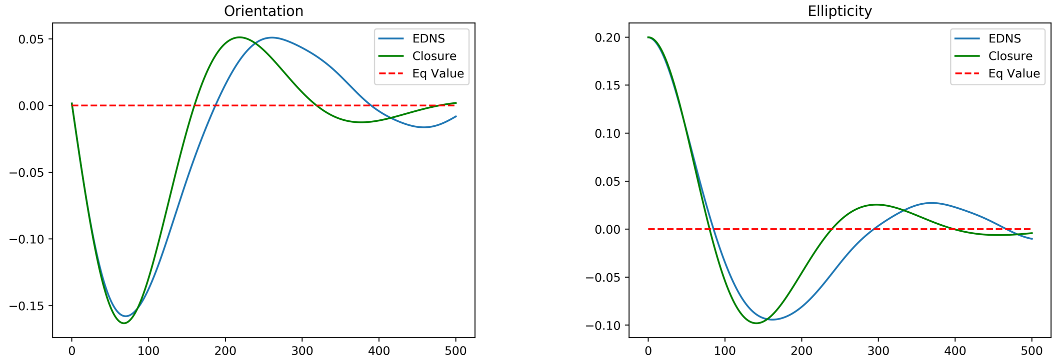

Figure 8.3: EDNS compared to optimal closure for case 3 of the single-layer quasigeostrophic equation. The initial values are $a_2 = 0.4$ and $a_1 = 0.0$ and $R_d = 2.0$. The phase difference between the closure and EDNS is very apparent. The rotation times are roughly 300 for the closure and 400 for the EDNS. The equilibration times are longer than shown in the simulation. The closure captures the peak values extremely well including the third peak of the orientation late in the simulation.

Similarly, figure 8.6 plots the eigenvalue of M as a function of the deformation radius R_d for $\beta = 0$. Because the energy of the system is dependent on the deformation radius, it is difficult to fix a β value while varying the deformation radius except when the equilibrium distribution is independent of the stream function. This is precisely the case when $\beta = 0$.

In figure 8.5, we again see that as we increase the temperature (that is, decrease β), the equilibration rate increases regardless of the deformation radius. As β increases to infinity, the equilibration rate drops to zero for any value of R_d. Indeed for sufficiently large β (≈ 20) the deformation radius seems to have little impact. Therefore, just as with the Euler equation, we see that our model is predicting the Kirchhoff ellipse and saying that these are persistent structures for any value of R_d. At the other extreme, the deformation radius has a much more profound effect. Note that the addition of the deformation radius means that $-8\pi \approx -25.13$ is no longer a lower bound for β. This means that the equilibration rate increases significantly more slowly as the deformation decreases. We see this trend more clearly in figure 8.6.

We also see that decreasing the deformation radius results in decreasing relaxation rates. This is intuitively expected. If we limit the range of interaction by decreasing the deformation radius, we expect smaller magnitude fluctuations and so slower relaxation to

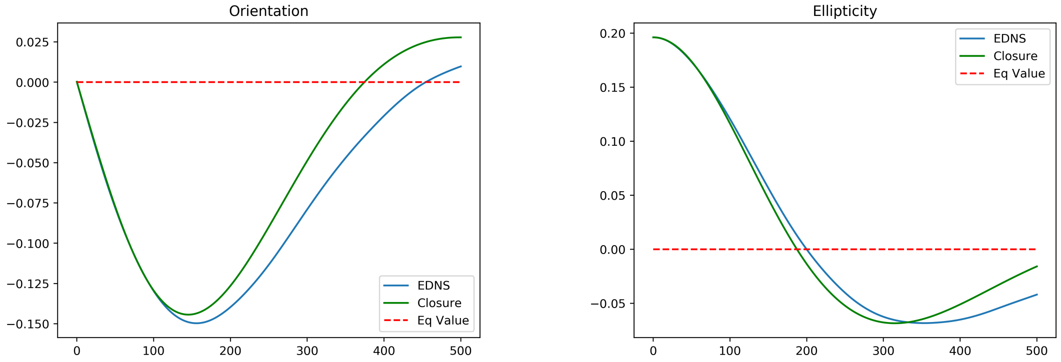

Figure 8.4: EDNS compared to optimal closure for case 4 of the single-layer quasigeostrophic equation. The initial values are $a_2 = 0.4$ and $a_1 = 0.0$ and $R_d = 1.0$. The time scales have lengthened so much that a full rotation has not been completed by the end of the run. A half rotation of the cloud has been completed around time 380 for the closure and 450 for the EDNS. There is only a single peak for each observable in the simulation but the closure does a good job predicting the magnitude of them.

equilibrium.

The closure allows us to determine more though in the case of $\beta_{eq} = 0$. In the asymptotic regime of $R_d << 1$, the closure predicts the equilibration rate is proportional to R_d^2. In the opposite regime of $R_d >> 1$, the closure predicts that the equilibration rate is given by $m_0 - m_1/R_d^2$ where m_0 is the equilibration rate for the Euler equation (or when $R_d = \infty$) and m_1 is some constant. These two regimes are represented in figure 8.6 by the magenta dashed and green dashed lines, respectively. The red dashed line gives the value of m_0.

This change of behavior can be interpreted physically. When R_d is small compared to the vortex cloud size, which is given by the angular impulse and so is order 1, increasing the deformation radius results in a point vortex seeing more point vortices at a rate roughly proportional to the increase in area. Once R_d is roughly the size of the entire vortex, that is, once R_d is order 1, increasing the interaction range no longer results in more fluctuations. So a point vortex already sees all the other vortices in the cloud and is no longer significantly affected by the increased interaction range.

To arrive at the stated asymptotic relation, we need to determine how the eigenvalue depends on the deformation radius. Recall first that, as argued in section 6.3, the matrices C, K, D and M are all diagonal with equal nonzero entries as a result of our choice of observables. Therefore, we seek to understand how m, the diagonal value of M, depends on R_d.

An important simplification when $\beta_{eq} = 0$ is that the equilibrium distribution ρ or ζ is independent of R_d (see (7.37)). This means that the only dependence m has on R_d is through the stream function and, specifically, the values ψ_{eq} and ψ_i.

Next, observe that for $\beta = 0$, the vector $\mathbf{U}$ reduces to the resolved vector $\mathbf{A}$ and has no dependence on R_d so that the matrix C is independent of R_d.

The final simplification is that the inversion operator G_{sl} reduces to the inversion operator for (7.25b). That is, both ψ_{eq} and ψ', and by extension ψ_i, satisfy an equation of the form

$$-\Delta\phi + \frac{1}{R_d^2}\phi = f(\mathbf{x})$$

This means that these functions depend on R_d in the same way.

We can now determine the asymptotic dependence of m on R_d for $R_d << 1$ and $R_d >> 1$. We start with the former. Let $\varepsilon = R_d^2$ so that ψ_{eq} and ψ_i satisfy the equation

$$-\varepsilon\Delta\phi + \phi = \varepsilon f$$

for an appropriate f. From this, we find that $\phi \sim \varepsilon\phi_0 + \varepsilon^2\phi_1 + \ldots$ where ϕ_0 and ϕ_1 satisfy

$$\phi_0 = f, \qquad \phi_1 = \Delta\phi_0.$$

Conceivably we could solve for the functions ϕ_0 and ϕ_1 but all we care about is the dependence on $\varepsilon = R_d^2$. From the above expansion, we see that both ψ_{eq} and ψ_i grow like R_d^2 for R_d small. It follows that $V \sim R_d^2$ and in turn that $\kappa \sim R_d^4$ and $\sigma \sim R_d^2$. Using these terms in (6.2), we find that for small R_d,

$$m \sim R_d^2$$

as stated.

In the case of $R_d >> 1$, we set $\varepsilon = 1/R_d^2$. Then ψ_{eq} and ψ_i satisfy an equation of the form

$$-\Delta\phi + \varepsilon\phi = f.$$

We now assume that $\phi \sim \phi_0 + \varepsilon\phi_1 + \ldots$. We then find that ϕ_0 and ϕ_1 satisfy

$$-\Delta\phi_0 = f, \qquad \Delta\phi_1 = \phi_0.$$

We again ignore the functions ϕ_0 and ϕ_1 and focus on the dependence on ε. As both ψ_{eq} and ψ_i have this form, we find that $V \sim v_0 + \varepsilon v_1$ for some functions v_0 and v_1. From this it results that

$$\kappa \sim \kappa_0 + \varepsilon\kappa_1, \qquad \sigma^2 \sim \sigma_0 + \varepsilon\sigma_1$$

Substitution of these expressions into (6.2), expanding the square root and replacing ε with $1/R_d^2$, we find that

$$m \sim m_0 + \frac{1}{R_d^2} m_1.$$

As the constant term m_0 arises from the order one terms and $\varepsilon = 0$ corresponds to the case of an infinite deformation radius, it must be the eigenvalue associated with the Euler equation case.

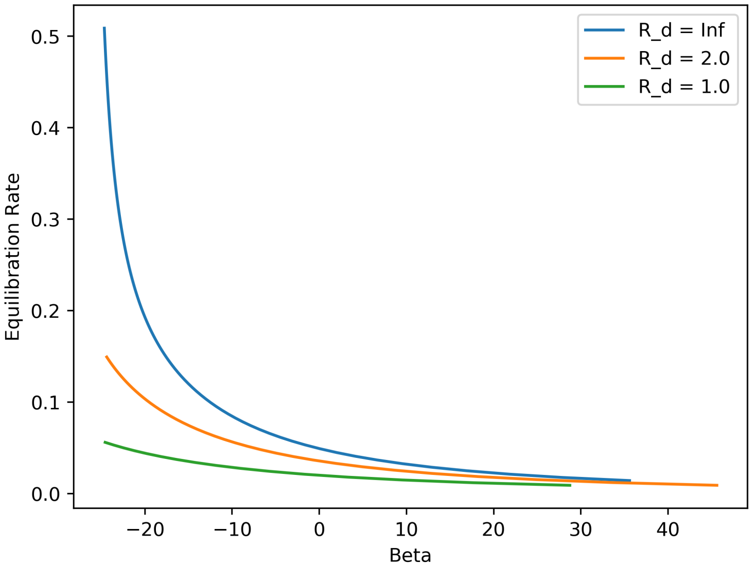

Figure 8.5: Predicted symmetrization rate versus inverse temperature for various values of the deformation radius. We again see that the equilibration goes to zero as β goes to infinity. We also see the equilibration increases as β decreases. Note that the deformation radius means that $-8\pi \approx -25.13$ is no longer a lower bound for β.

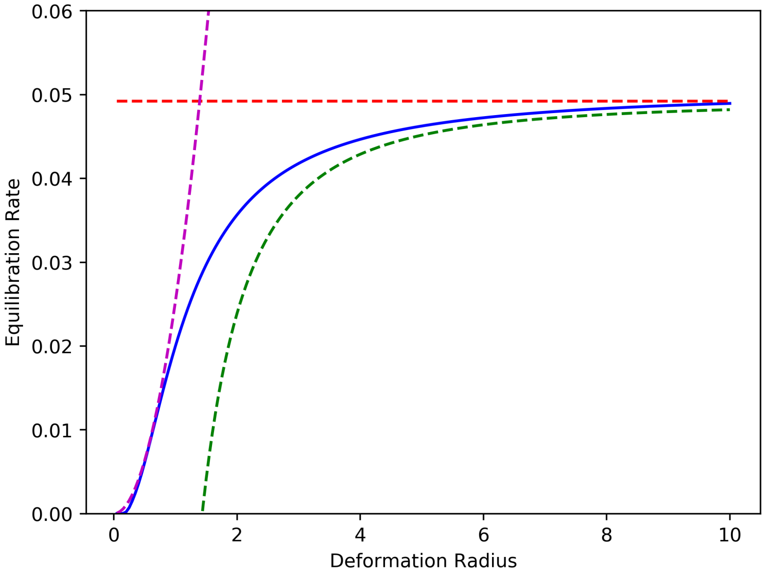

Figure 8.6: Predicted symmetrization rate versus deformation radius for $\beta = 0$. Near zero the equilibration grows like R_d^2 as shown by the dashed magenta line. At large values of R_d, the equilibration grows like $1/R_d^2$ as shown by the dashed green line. The dashed red line is the equilibration value for the Euler equations case (or $R_d = \infty$).

CHAPTER 9

TWO-LAYER QUASIGEOSTROPHIC DYNAMICS

We will now study a more realistic version of the quasigeostrophic equation. Instead of a single fluid of constant density, we assume that there are two fluid layers each of constant density. Physically, the density difference is often the result of temperature differences. We can view this system as a warmer less dense fluid on top of a colder more dense fluid. This simple modification to quasigeostrophic equations provides a surprising amount of insight into geophysical fluids while remaining relatively simple [48]. Indeed the interaction of the two-layers is fundamental as revealed by the fact that the continuously stratified quasigeostrophic equation can be viewed as a fluid composed of infinitely many layers [60].

In this chapter, we derive the two-layer quasigeostrophic equations as well as rewrite them in barotropic and baroclinic components. We then move on to describe the energy of the system and particularly the potential energy that can be converted into kinetic energy. Following this, we look at the theory of baroclinic instability. We rely heavily on [48] and [60] for these topics. Then we cover the point vortex idealization for the two-layer system as well as the accompanying equilibrium statistical mechanics theory.

9.1 Two-Layer Quasigeostrophic Equations

In this section we derive the equations of the two-layer system. The derivation is similar to the single-layer case so we will discuss it briefly. Then we discuss an alternate view of the two-layer system by decomposing it into the barotropic and baroclinic modes.

9.1.1 Derivation

Consider two fluids each with constant density ρ_1 and ρ_2 where the ρ_1 is the density of the fluid on top and we assume that $\rho_1 < \rho_2$. We denote the surface of the top layer by $\eta_1(x, y, t)$, the interface between the two fluids by $\eta_2(x, y, t)$ and the bottom topography by $\eta_b(x, y)$. We denote the depth of the top layer by $h_1(x, y, t)$ and the depth of the bottom layer by $h_2(x, y, t)$. From these definitions, it is clear that $h_1 = \eta_1 - \eta_2$ and $h_2 = \eta_2 - \eta_b$.

We now make three assumption. First, the variation in layer thickness is small. If we let H_k denote the typical depth of the k^{th} layer, we can write $h_k = H_k + h'_k$ and this assumption then takes the form that $h'_k/H_k << 1$. Second, the Rossby number is small. This means that the rotational advection terms dominate the local acceleration and our flow is nearly geostrophic. Third, the variations in the Coriolis parameter are small. Mathematically, if we let $f = f_0 + \beta y$, then this assumption takes the familiar form $\beta L/f_0 << 1$ where L is a typical horizontal length scale. These assumptions are nearly identical to those made for the derivation of the single-layer equations.

Just as we found the single-layer equation as a perturbation expansion of the rotating shallow-water equations, we could do the same for the two-layer equations. Instead for brevity, we will start from the potential vorticity. For the k^{th} layer, let

$$Q_k = \frac{\zeta_k + f}{h_k}$$

denote the potential vorticity of that layer. Then each layer conserves potential vorticity so that

$$\partial_t Q_k + \mathbf{u}_k \cdot \nabla Q_k = 0. \tag{9.1}$$

From our three assumptions, we have

$$\begin{aligned} Q_k &\approx \frac{1}{H_k}(\zeta_k + f)\left(1 - \frac{h'_k}{H_k}\right) \\ &\approx \frac{1}{H_k}\left(\zeta_k + f - f_0\frac{h'_k}{H_k}\right) \end{aligned} \tag{9.2}$$

Since Q_k is an advected term (Q_k only appears in (9.1) with derivatives), we may neglect the constant terms and conclude that

$$\partial_t q_k + \mathbf{u}_k \cdot \nabla q_k = 0,$$

where

$$q_k = \zeta_k + f - f_0 \frac{h_k'}{H_k}. \tag{9.3}$$

In order to complete the derivation we want to replace the h_k' term. To do this, we use hydrostatic and geostrophic balance. From hydrostatic balance, we know that the pressure is given by integrating from the top so that

$$\begin{aligned} p_1 &= \rho_1 g(\eta_1 - z) \\ p_2 &= \rho_1 g(\eta_1 - \eta_2) + \rho_2 g(\eta_2 - z) = \rho_1 g \eta_1 + \rho_1 g' \eta_2 - \rho_2 g z \end{aligned}$$

where we have introduced the reduced gravity $g' = g(\rho_2 - \rho_1)/\rho_1$. Since we are nearly geostrophic, we expect

$$\begin{aligned} \mathbf{f}_0 \times \mathbf{u}_1 &= -g\nabla\eta_1 = -g\nabla(h_1' + h_2' + \eta_b), \\ \mathbf{f}_0 \times \mathbf{u}_2 &= -g\nabla\eta_1 - g'\nabla\eta_2 = -g\nabla(h_1' + h_2' + \eta_b) - g'\nabla(h_2' + \eta_b). \end{aligned}$$

Because the right hand side in both equations is a gradient term, we can cross differentiate and find that $\mathbf{u}_k$ is (approximately) incompressible. Therefore, we can define stream functions ψ_1 and ψ_2 such that

$$\mathbf{u}_k = \nabla^\perp \psi_k, \quad -\Delta\psi_k = \zeta_k.$$

It follows that we have the relations

$$\psi_1 = -\frac{g}{f_0}(h_1' + h_2' + \eta_b), \quad \psi_2 = -\frac{g}{f_0}(h_1' + h_2' + \eta_b) - \frac{g'}{f_0}(h_2' + \eta_b).$$

Solving for h_1' and h_2' between these two gives the equations

$$h_1' = -\frac{f_0}{g'}(\psi_1 - \psi_2) - \frac{f_0}{g}\psi_1, \tag{9.4a}$$

$$h_2' = -\frac{f_0}{g'}(\psi_2 - \psi_1) - \eta_b. \tag{9.4b}$$

Using these equations in (9.3) gives us the two-layer quasigeostrophic equations

$$q_1 = -\Delta\psi_1 + \frac{1}{R_{1d}^2}(\psi_1 - \psi_2) + \beta y + \frac{1}{R_{ed}^2}\psi_1, \tag{9.5a}$$

$$\partial_t q_1 + [q_1, \psi_1] = 0, \tag{9.5b}$$

$$q_2 = -\Delta\psi_2 - \frac{1}{R_{2d}^2}(\psi_1 - \psi_2) + \beta y + \frac{f_0}{H_2}\eta_b, \tag{9.5c}$$

$$\partial_t q_2 + [q_2, \psi_2] = 0, \tag{9.5d}$$

where R_{ed} is the external deformation radius and we have introduced R_{kd}, the Rossby internal deformation radius of the k^{th} layer, given by

$$R_{kd} = \frac{\sqrt{g' H_k}}{f_0}.$$

In everything that follows, we make the following simplifying assumptions: The bottom topography is flat (so that $\eta_b = H_1 + H_2$), our length scales of interest are much less than R_{ed} (this is the rigid lid approximation) and finally, $H_1 = H_2$ so that $R_{1d} = R_{2d} = R_d$. With these assumptions the system (9.5) reduces to

$$q_1 = -\Delta\psi_1 + \frac{1}{R_d^2}(\psi_1 - \psi_2), \tag{9.6a}$$

$$\partial_t q_1 + [q_1, \psi_1] = 0, \tag{9.6b}$$

$$q_2 = -\Delta\psi_2 - \frac{1}{R_d^2}(\psi_1 - \psi_2), \tag{9.6c}$$

$$\partial_t q_2 + [q_2, \psi_2] = 0. \tag{9.6d}$$

9.1.2 Barotropic and Baroclinic Components

In the simplified case of (9.6), we can write the system in a different way. If we add (9.6a) to (9.6c), we get the equation

$$q_1 + q_2 = -\Delta(\psi_1 + \psi_2).$$

This suggests that we define the new variables

$$q_T = \frac{1}{2}(q_1 + q_2), \qquad \psi_T = \frac{1}{2}(\psi_1 + \psi_2), \tag{9.7}$$

which are called the barotropic vorticity and barotropic stream function, respectively. The two are then related by

$$q_T = -\Delta\psi_T. \tag{9.8}$$

Subtracting the same two equations gives us

$$q_1 - q_2 = -\Delta(\psi_1 - \psi_2) + \frac{2}{R_d^2}(\psi_1 - \psi_2),$$

which leads us to introduce the variables

$$q_C = \frac{1}{2}(q_1 - q_2), \qquad \psi_C = \frac{1}{2}(\psi_1 - \psi_2). \tag{9.9}$$

These are called the baroclinic vorticity and baroclinic stream function, respectively. They satisfy the relation

$$q_C = -\Delta\psi_C + \frac{2}{R_d^2}\psi_C. \tag{9.10}$$

From the definitions, we see that the barotropic components are an average of the two-layers. They can be viewed as the single-layer behavior of the system. Indeed, the barotropic vorticity evolves according to the dynamic equation

$$\partial_t q_T + [q_T, \psi_T] + [q_C, \psi_C] = 0,$$

so that if there is no baroclinic component ($q_C = \psi_C = 0$), the barotropic components obey the Euler equation. If we had not made the rigid lid approximation, the barotropic components would obey the single-layer equations given by (7.25). In this sense, the barotropic components give the single-layer behavior of the model.

On the other hand, the baroclinic components quantify the difference in the two-layers. It describes the asymmetry of the system or the two-layer behavior of the model. Indeed, the baroclinic vorticity is advected by

$$\partial_t q_C + [q_T, \psi_C] + [q_C, \psi_T] = 0.$$

This tells us that q_C evolves according to the cross term advection—that is, its evolution is governed by how the barotropic and baroclinic components interact with one another. This stands in contrast to the evolution equation for the barotropic vorticity which evolves according to the self interaction terms.

Before moving on, we note for future use that we can recover the original variables using the equations

$$q_1 = q_T + q_C, \qquad \psi_1 = \psi_T + \psi_C, \tag{9.11}$$

$$q_2 = q_T - q_C, \qquad \psi_2 = \psi_T - \psi_C. \tag{9.12}$$

These are easily obtained from the definitions.

9.2 Available Potential Energy

The study of the two-layer quasigeostrophic system focuses on baroclinic instability. This instability is driven by the conversion of potential energy into kinetic energy. In this section, we will define the total energy and discuss how it is divided into kinetic and potential energy. Fundamentally, the potential energy is gravitational in nature but much of it is not transferable into kinetic energy. This leads us to the idea of available potential energy.

From time symmetry and Noether's theorem [21, 34], we know that the quantity

$$E = \frac{1}{2} \int_{\mathbb{R}^2} \psi_1 q_1 + \psi_2 q_2 \, d\mathbf{x} \tag{9.13}$$

is conserved. As suggested by the notation, this is the two-layer energy. It is a natural extension of the energy from the Euler equation case.

We now examine how this total energy is divided into kinetic and potential components. We first use (9.6a) and (9.6c) to eliminate q_1 and q_2 to get

$$E = \frac{1}{2} \int_{\mathbb{R}^2} \psi_1 \left(-\Delta \psi_1 + \frac{1}{R_d^2}(\psi_1 - \psi_2) \right) + \psi_2 \left(-\Delta \psi_2 - \frac{1}{R_d^2}(\psi_1 - \psi_2) \right) \, d\mathbf{x}$$

Using Green's first identity and rearranging terms, we see that

$$E = \frac{1}{2} \int_{\mathbb{R}^2} |\nabla \psi_1|^2 + |\nabla \psi_2|^2 + \frac{1}{R_d^2}(\psi_1 - \psi_2)^2 \, d\mathbf{x},$$

which can be interpreted as the kinetic energy of the first layer, the kinetic energy of the second layer and a potential energy.

In terms of the barotropic and baroclinic modes, the total energy is given by

$$E = \int_{\mathbb{R}^2} \psi_T q_T + \psi_C q_C \, d\mathbf{x}. \tag{9.14}$$

Proceeding as before, we find that

$$E = \int_{\mathbb{R}^2} |\nabla \psi_T|^2 + |\nabla \psi_C|^2 + \frac{2}{R_d^2} \psi_C^2 \, d\mathbf{x}. \tag{9.15}$$

The potential energy term present in both decompositions and given by

$$APE = \frac{1}{2R_d^2} \int_{\mathbb{R}^2} (\psi_1 - \psi_2)^2 \, d\mathbf{x} = \frac{2}{R_d^2} \int_{\mathbb{R}^2} \psi_C^2 \, d\mathbf{x} \tag{9.16}$$

is called the available potential energy. This is the potential energy that is available to the system to turn into kinetic energy.

It should be noted that these are strictly formal calculation. As our domain is all of

$\mathbb{R}^2$, many of the above integrals (if not all of them) are infinite. It is nevertheless revealing. In particular, it tells us that the minimal potential energy state is when $\psi_1 = \psi_2$ or when $\psi_C = 0$. This is a purely barotropic state and corresponds to a flat interface between the two fluids.

To understand the distinction between potential energy and available potential energy, consider the potential energy of a two-layer shallow-water system

$$PE = \frac{1}{2}\int_{\mathbb{R}^2} \rho_2 g(h_1^2 - \eta_b^2) - \rho_1 g h_1^2 d\mathbf{x} = \frac{1}{2}\int_{\mathbb{R}^2} \rho_1 g'(h_1')^2 d\mathbf{x} + constants,$$

where we have used the notation defined in section 9.1. Examining the terms, this is clearly a gravitational potential energy, much of which is pent up in the constants. The constant terms cannot be converted to kinetic energy. The remaining term is precisely what we have defined to be the available potential energy. From a physical standpoint, the unavailable potential energy is the gravitational potential energy of the less dense fluid on top of the denser fluid. Reducing the gravitational potential energy of a fluid parcel in the top layer, requires moving it closer to the bottom and thus displacing the denser fluid and increasing the total potential energy.

9.3 Baroclinic Instability

Baroclinic instability theory was pioneered by Charney [12] and Eady [20] using linear stability analysis to examine the onset of the resulting turbulent flow. They were attempting to understand the mechanisms of the midlatitude synoptic storms. Since then it has been used in oceanography as well as extraterrestrial atmospherics [60]. Here we recount the Phillips problem which is the the two-layer version of their argument. It was originally worked out by Phillips [46] and the spirit is the same as that of Eady's and Charney's works.

Fundamentally, the phenomenology is about the conversion of potential energy into kinetic energy. The uneven heating of the Earth's surface causes a temperature difference in the atmosphere with warmer air near the equator and cooler air at the (north) pole. In terms of our two-layer setup, this corresponds to the interface between the two-layers sloping upward as we head north (the positive y direction). The rotation of the Earth inhibits transferring the potential energy in this configuration into kinetic energy. In fact it can stop it completely, that is, this can be a stable structure, if the slope is not sufficiently large. We will now work out the Phillips problem as presented in [60] (with some help from [48] as well). Specifically, we will use linear stability analysis on an idealized problem to find stability criteria as well as make a rough estimate of the size of the resulting instability.

We start from the system (9.6) but in the beta plane instead of the f plane. The equations then take the form

$$q_1 = -\Delta\psi_1 + \frac{1}{R_d^2}(\psi_1 - \psi_2) + \beta y, \tag{9.17a}$$

$$\partial_t q_1 + [q_1, \psi_1] = 0, \tag{9.17b}$$

$$q_2 = -\Delta\psi_2 - \frac{1}{R_d^2}(\psi_1 - \psi_2) + \beta y, \tag{9.17c}$$

$$\partial_t q_2 + [q_2, \psi_2] = 0. \tag{9.17d}$$

Recall that we have assumed a rigid lid, a flat bottom and equal layer depth. A steady solution of the equations is given by

$$\psi_1 = Uy, \qquad \psi_2 = -Uy.$$

This corresponds to a flow of magnitude U in the positive x direction in the top layer and in the negative x direction in the bottom layer.

Now consider a small perturbation of this solution so that

$$\psi_1 = Uy + \psi_1', \qquad \psi_2 = -Uy + \psi_2',$$

where ψ_1' and ψ_2' are small. Plugging this into (9.17), eliminating the potential vorticity and discarding the double prime terms gives us the (linearized) system

$$
\begin{aligned}
(\partial_t + U\partial_x)\left(-\Delta\psi_1' + \frac{k_d^2}{2}(\psi_1' - \psi_2')\right) - \partial_x\psi_1'(\beta + k_d^2 U) = 0,\\
(\partial_t - U\partial_x)\left(-\Delta\psi_2' - \frac{k_d^2}{2}(\psi_1' - \psi_2')\right) - \partial_x\psi_2'(\beta - k_d^2 U) = 0,
\end{aligned}
$$

where we have introduced $k_d^2 = 2/R_d^2$. We now seek solutions of the form

$$
\psi_j' = \mathrm{Re}(\tilde{\psi}_j e^{ik(x-ct)} e^{ily}),
$$

where k and l are the x and y wave numbers, respectively, and $\tilde{\psi}_j$ is a (complex) amplitude. (This means we must assume a square, doubly periodic domain.)

Plugging this form into our linearized equations, we find that

$$
\begin{aligned}
(ik(U-c))(K^2\tilde{\psi}_1 + \frac{k_d^2}{2}(\tilde{\psi}_1 - \tilde{\psi}_2)) - ik\tilde{\psi}_1(\beta + k_d^2 U) = 0,\\
-(ik(U+c))(K^2\tilde{\psi}_2 - \frac{k_d^2}{2}(\tilde{\psi}_1 - \tilde{\psi}_2)) - ik\tilde{\psi}_2(\beta - k_d^2 U) = 0,
\end{aligned}
$$

where $K^2 = k^2 + l^2$. After rearranging and canceling common terms, we get the homogeneous linear system in $\tilde{\psi}_1$ and $\tilde{\psi}_2$

$$
\begin{aligned}
\left[(U-c)\left(K^2 + \frac{k_d^2}{2}\right) - (\beta + k_d^2 U)\right]\tilde{\psi}_1 - \frac{k_d^2(U-c)}{2}\tilde{\psi}_2 = 0\\
\frac{k_d^2(U+c)}{2}\tilde{\psi}_1 - \left[(U+c)\left(K^2 + \frac{k_d^2}{2}\right) + (\beta - k_d^2 U)\right]\tilde{\psi}_2 = 0.
\end{aligned}
$$

In order to have a nontrivial solution, we require that the determinant of the coefficient matrix is zero. This condition results in the quadratic equation in c

$$
0 = K^2(K^2 + k_d^2)c^2 + 2\beta(K^2 + k_d^2/2)c + \beta^2 - U^2K^2(K^2 - k_d^2).
$$

Solving yields the relationship

$$
c = -\frac{\beta}{K^2 + k_d^2}\left[1 + \frac{k_d^2}{2K^2} \pm \frac{k_d^2}{2K^2}\left(1 + \frac{4K^4(K^4 - k_d^4)}{k_\beta^4 k_d^4}\right)^{1/2}\right],
$$

where $k_\beta = \sqrt{\beta/U}$.

Given the initial form of our solution, we know that our solution will grow like $e^{\mathrm{Im}(c)t}$. In the case of $\beta = 0$, we find (either from our solution or more simply from the quadratic equation) that

$$c = \pm U \left(\frac{K^2 - k_d^2}{K^2 + k_d^2} \right)^{1/2}.$$

This has a positive imaginary part for any value of U so that there is always instability. However, note that the instability occurs only when $K < k_d = 2/R_d$ so that the wave numbers that experience instability are smaller than the deformation radius.

For the general case, in order for instability to occur, we require

$$k_\beta^4 k_d^4 + 4K^4(K^4 - k_d^4) < 0, \tag{9.18}$$

where $K^4 = (k^2 + l^2)^2$. Rearranging and using the definition of k_β gives us the inequality

$$\beta^2 k_d^4 < 4U^2 K^4 (k_d^4 - K^4).$$

The maximum of the right hand side occurs at $K^4 = k_d^4/2$. Plugging this in, we arrive at the instability criterion

$$\frac{2\beta}{k_d^2} = \beta R_d^2 < 2U,$$

where $2U$ is the difference between the velocities in the two-layers.

Examining this inequality, we see first that β has a stabilizing influence on the system. Indeed for a fixed U and R_d value, we can always find β large enough so that the system is stable. From another perspective, we see that for a fixed β and R_d, there is a minimum shear velocity for instability to occur. Recall that the stream functions are $\psi_1 = Uy$ and $\psi_2 = -Uy$ and that the stream functions relate directly to the displacement of the interface. Therefore the larger the value of U, the more baroclinic the initial condition and the larger the slope of the interface between the layers.

Returning to our original instability inequality (9.18), we can extract a few more pieces of information. Just as in the case of $\beta = 0$, we see that the instability can only occur on scales comparable to or larger than the deformation radius as it is necessary that

$$k_d^2 > K^2.$$

Next, if we consider $K << k_d$, then (9.18) is approximately $k_\beta^4 - 4K^4 < 0$ so that

$$K > \frac{\beta}{U\sqrt{2}}$$

and we see that there is a low wave number cutoff for instability.

9.4 Point Vortex Idealization

The point vortex idealization was worked out for the two-layer equations by Gryanik [23]. Hogg and Stommel further explored this model in [25] and [26]. In these works, they observed that a positive vortex in the upper layer will lower the interface as will a negative vortex in the lower layer. Because these point vortices have opposite signs, they will self advect and, in doing so, transport heat and reduce the available potential energy. They called these pairs hetons and noted that they can be cold (the heton we described above is cold as the interface of the fluid has been raised) or warm (this would be the opposite arrangement with the negative vortex on top and the positive vortex on bottom). They also discovered that groups of like temperature hetons tended to repel each other when separated by a distance larger than the internal deformation radius and to merge when their separation was less than internal deformation radius. Based on this observation, they suggested that hetons were a new approach to modeling baroclinic instability—one that does not require the idealized circumstances necessary for the linear stability analysis of Eady and Charney as discussed in the last section.

In this section, we give the dynamical system which describes the evolution of a point vortex ensemble and the corresponding equilibrium statistical mechanics theory. Many of the details are similar (if not identical) to the Euler case so we will describe them only briefly and instead emphasize the physical interpretation.

9.4.1 Dynamics

Consider a system of N point vortices in the top layer and N point vortices in the bottom layer. Let the position of the i^{th} vortex in the k^{th} layer be denoted by $\mathbf{x}_{ki}$ and let its strength be γ_{ki}. Then the vorticity distribution in each layer is given by

$$q_1^N = \sum_{i=1}^{N} \gamma_{1i} \delta_{\mathbf{x}_{1i}}(\mathbf{x}), \qquad q_2^N = \sum_{i=1}^{N} \gamma_{2i} \delta_{\mathbf{x}_{2i}}(\mathbf{x}). \tag{9.19}$$

To derive the dynamical system, it is easiest to use the barotropic and baroclinic components. From the relations (9.8) and (9.10), we see that the barotropic Green's function is

$$g_T(\mathbf{x}, \mathbf{x}') = -\frac{1}{2\pi} \log |\mathbf{x} - \mathbf{x}'|, \tag{9.20}$$

and the baroclinic Green's function is

$$g_C(\mathbf{x}, \mathbf{x}') = \frac{1}{2\pi} K_0(k_d |\mathbf{x} - \mathbf{x}'|), \tag{9.21}$$

where $k_d = \sqrt{2}/R_d$. Combining this with the definitions (9.7) and (9.9), we see that the stream function of the k^{th} layer is given by

$$\psi_k^N(\mathbf{x}) = \sum_{\ell=1}^{2} \sum_{j=1}^{N} \gamma_{\ell j} g_T(\mathbf{x}, \mathbf{x}_{\ell j}) - \sigma(k, \ell) \gamma_{\ell j} g_C(\mathbf{x}, \mathbf{x}_{\ell j}), \tag{9.22}$$

where

$$\sigma(k, \ell) = \begin{cases} 1, & k = \ell, \\ -1, & k \neq \ell. \end{cases}$$

We obtain the stream function which advects the i^{th} point vortex in the k^{th} layer from (9.22) by omitting the self advecting term. Denoting this stream function by $\psi_{ki}^N(\mathbf{x})$, we get the system of $4N$ ordinary differential equations which governs the dynamics from

$$\dot{\mathbf{x}}_{ki} = \nabla^{\perp} \psi_{ki}, \tag{9.23}$$

where $\nabla^{\perp}$ is given by (2.3).

It is worth taking a moment to look at the resulting flow in a simplified case. Consider the case of a single point vortex in the top layer of unit strength. Then for any point in the top layer (9.22) reduces to

$$\psi_1^1(\mathbf{x}) = g_T(\mathbf{x}, \mathbf{x}_{11}) - g_C(\mathbf{x}, \mathbf{x}_{11}),$$

and the magnitude of the tangential velocity is

$$\frac{1}{2\pi}\left(\frac{1}{r} + k_d K_1\left(k_d r\right)\right),$$

where K_1 is the modified Bessel of the second kind and r is the radial distance from the vortex. Both K_0 and K_1 decay exponentially at distances longer than $1/k_d = R_d/\sqrt{2}$ and are effectively zero. Therefore, at distances from the point vortex larger than the (internal) deformation radius, the top layer stream function appears to be a single-layer fluid. Specifically, it has the $1/r$ dependence that we saw with the point vortex idealization of the Euler equations. On the other hand, for small distances, we know that $K_1(r) \sim 1/r$ so that

$$\left(\frac{1}{r} + k_d K_1\left(k_d r\right)\right) \sim \left(\frac{1}{r} + \frac{k_d}{k_d r}\right) = \frac{2}{r}.$$

Therefore the second layer strengthens the point vortex by a factor of two.

For any point in the bottom layer in our current case, (9.22) reduces to

$$\psi_2^1(\mathbf{x}) = g_T(\mathbf{x}, \mathbf{x}_{11}) + g_C(\mathbf{x}, \mathbf{x}_{11}),$$

and the magnitude of the tangential velocity is

$$\frac{1}{2\pi}\left(\frac{1}{r} - k_d K_1\left(k_d r\right)\right).$$

Here we see the same long range behavior. That is, at distances larger than the deformation radius, the stream function looks like the stream function of a single-layer with a single point vortex. However, at small distances, we get a significantly different behavior. Again, using the asymptotics for K_1 with small argument, we have

$$\left(\frac{1}{r} - k_d K_1\left(k_d r\right)\right) \sim \left(\frac{1}{r} - \frac{k_d}{k_d r}\right) = 0.$$

Therefore, the magnitude of the flow reduces to zero as we approach the location of the point vortex in the bottom layer. It follows that another point vortex positioned at the same spot in the bottom layer does not see the point vortex in the top layer. Indeed, the stream function for two point vortices at the same point in different layers is identical to the single-layer stream function of a point vortex with twice the strength.

Returning to the dynamics of our two distributions, we can again write this system as a canonical Hamiltonian system with the conjugate variables $q_{ki} = \sqrt{\gamma_{ki}} x_{ki}$ and $p_{ki} = \sqrt{\gamma_{ki}} y_{ki}$ (as in the Euler case) with the Hamiltonian

$$\begin{aligned} H^N = &\frac{1}{4}\sum_{i=1}^{N}\sum_{j\neq i}\gamma_{1i}\gamma_{1j}\left[g_T(\mathbf{x}_{1i},\mathbf{x}_{1j}) + g_C(\mathbf{x}_{1i},\mathbf{x}_{1j})\right] \\ &+ \frac{1}{2}\sum_{i=1}^{N}\sum_{j=1}^{N}\gamma_{1i}\gamma_{2j}\left[g_T(\mathbf{x}_{1i},\mathbf{x}_{2j}) - g_C(\mathbf{x}_{1i},\mathbf{x}_{2j})\right] \\ &+ \frac{1}{4}\sum_{i=1}^{N}\sum_{j\neq i}\gamma_{2i}\gamma_{2j}\left[g_T(\mathbf{x}_{2i},\mathbf{x}_{2j}) + g_C(\mathbf{x}_{2i},\mathbf{x}_{2j})\right]. \end{aligned} \tag{9.24}$$

This is the energy from the top layer self-interaction (first term) plus energy from the top-bottom interaction (second term) plus the energy from the bottom self-interaction (third term). As it is time independent, the Hamiltonian is a conserved quantity. In fact, it is the point vortex equivalent (after omitting the self interaction terms) of the continuum energy

$$E = \frac{1}{2}\int_{\mathbb{R}^2} \psi_1 q_1 + \psi_2 q_2 \, d\mathbf{x} = \int_{\mathbb{R}^2} \psi_T q_T + \psi_C q_C \, d\mathbf{x}. \tag{9.25}$$

We once again have translational and rotational symmetries which lead to the conservation of the center of vorticity

$$\mathbf{B} = \sum_{k=1}^{2}\sum_{i=1}^{N}\gamma_{ki}\mathbf{x}_{ki} \tag{9.26}$$

and the angular impulse

$$L^2 = \sum_{k=1}^{2} \sum_{i=1}^{N} \gamma_{ki} |\mathbf{x}_{ki}|^2. \tag{9.27}$$

The corresponding continuum values are given by

$$\mathbf{B} = \int_{\mathbb{R}^2} \mathbf{x}(q_1 + q_2) d\mathbf{x} \tag{9.28}$$

and

$$L^2 = \int_{\mathbb{R}^2} |\mathbf{x}|^2 (q_1 + q_2) d\mathbf{x}, \tag{9.29}$$

respectively. Just as we did in the Euler case we will use translational invariance to assume that the center of vorticity is the origin.

Finally, as a direct result of the conservation of (potential) vorticity, we have that the total circulation in each layer is conserved. In terms of the point vortices, this means that the quantity Γ_k given by

$$\Gamma_k = \sum_{i=1}^{N} \gamma_{ki} \tag{9.30}$$

is a constant. Actually, as is normal with point vortices, the values γ_{ki} are all constants. The continuum equivalent is

$$\Gamma_k = \int_{\mathbb{R}^2} q_k d\mathbf{x}. \tag{9.31}$$

9.4.2 Equilibrium Statistical Mechanics

DiBattista and Majda extended the point vortex statistical mechanics for the plane to the two-layer quasigeostrophic equations [19]. The primary result is a set of mean-field equations which describe the stream functions and vorticity distributions of the most probable state. They derive these equations using both a kinetic argument and a maximum entropy argument. What follows is their maximum entropy argument with some comments added.

To start, just as in the Euler case, we assume that any configuration with the appropriate value of the Hamiltonian and angular impulse is equally probable. The same warnings apply here as in the single-layer case: there are no physical grounds on which we make this assumption. From this, there is an appropriate microcanonical measure from which we can define the entropy.

In the limit $N \to \infty$, $\gamma \to 0$ with $\Gamma = \gamma N$ held constant, we find that maximizing the entropy is equivalent to minimizing quantity

$$\int_{\mathbb{R}^2} \rho_1 \log \rho_1 + \rho_2 \log \rho_2 \, d\mathbf{x}.$$

To see this, we can make the same sort of classical argument previously made or appeal directly to the theory of large deviations.

Finding the most probable distribution with energy E and angular impulse L^2 is then equivalent to solving the constrained optimization problem

$$\text{minimize} \int_{\mathbb{R}^2} \rho_1 \log \rho_1 + \rho_2 \log \rho_2 \, d\mathbf{x} \quad \text{subject to} \tag{9.32a}$$

$$\frac{1}{2} \int_{\mathbb{R}^2} \psi_1 q_1 + \psi_2 q_2 d\mathbf{x} = E, \tag{9.32b}$$

$$\int_{\mathbb{R}^2} |\mathbf{x}|^2 (q_1 + q_2) d\mathbf{x} = L^2, \tag{9.32c}$$

$$\int_{\mathbb{R}^2} q_1 d\mathbf{x} = 1, \tag{9.32d}$$

$$\int_{\mathbb{R}^2} q_2 d\mathbf{x} = 1, \tag{9.32e}$$

where $q_1 = \Gamma_1 \rho_1$ and $q_2 = \Gamma_2 \rho_2$, and the stream functions ψ_1 and ψ_2 are solutions the system

$$q_1 = -\Delta \psi_1 + \frac{1}{R_d^2} (\psi_1 - \psi_2), \qquad q_2 = -\Delta \psi_2 - \frac{1}{R_d^2} (\psi_1 - \psi_2),$$

where R_d is the (internal) deformation radius.

This can be solved using the calculus of variations as before to arrive at the system of mean-field equations

$$q_1 = \Gamma_1 \exp\{(-\beta \psi_1 - \alpha r^2) \Gamma_1 - \mu_1\}, \tag{9.33a}$$

$$-\Delta \psi_1 + \frac{1}{R_d^2} (\psi_1 - \psi_2) = q_1, \tag{9.33b}$$

$$q_2 = \Gamma_2 \exp\{(-\beta \psi_2 - \alpha r^2) \Gamma_2 - \mu_2\}, \tag{9.33c}$$

$$-\Delta \psi_2 - \frac{1}{R_d^2} (\psi_1 - \psi_2) = q_2, \tag{9.33d}$$

where α, β, μ_1 and μ_2 are values such that the constraints (9.32b), (9.32c), (9.32d) and (9.32e) are satisfied. The solution of this nonlinear system gives the most probable distribution.

The Whitaker-Turkington algorithm described in section 3.3 can be used yet again to compute the equilibrium states. The only aspect that is not immediately obvious is how to modify the energy constraint. The key is to realize that we can view the vorticity distributions q_1 and q_2 as well as the stream functions ψ_1 and ψ_2 as components of a vector (say $\mathbf{q}$ and ψ, respectively) and then apply the our previous energy constraint modification to these vectors.

In this light, we can write the energy constraint as

$$\frac{1}{2}\int_{\mathbb{R}^2} \psi \cdot \mathbf{q}\, d\mathbf{x} = E.$$

Therefore, the linearized energy constraint is simply

$$H_n + \int_{\mathbb{R}^2} \psi^n \cdot (\mathbf{q} - \mathbf{q}^n) d\mathbf{x} = H_n + \int_{\mathbb{R}^2} \psi_1^n (q_1 - q_1^n) + \psi_2^n (q_2 - q_2^n)\, d\mathbf{x} = E, \tag{9.34}$$

where

$$H_n = \frac{1}{2}\int_{\mathbb{R}^2} \psi^n \cdot \mathbf{q}^n d\mathbf{x} = \frac{1}{2}\int_{\mathbb{R}^2} \psi_1^n q_1^n + \psi_2^n q_2^n\, d\mathbf{x}.$$

All the other constraints are linear and straightforward to implement.

We also need a way to solve the partial differential equation system

$$\begin{aligned} q_1 &= -\Delta\psi_1 + \frac{1}{R_d^2}(\psi_1 - \psi_2), \\ q_2 &= -\Delta\psi_2 - \frac{1}{R_d^2}(\psi_1 - \psi_2), \end{aligned}$$

for a given q_1 and q_2. The most direct method would be to rewrite the system as

$$T \begin{pmatrix} \psi_1 \\ \psi_2 \end{pmatrix} = \begin{pmatrix} q_1 \\ q_2 \end{pmatrix},$$

where

$$T = \begin{pmatrix} -\Delta + \frac{1}{R_d^2} & -\frac{1}{R_d^2} \\ -\frac{1}{R_d^2} & -\Delta + \frac{1}{R_d^2} \end{pmatrix}.$$

We then construct a solver for the differential operator T.

An alternative is to use the barotropic and baroclinic decomposition. The barotropic stream function solves

$$-\Delta\psi_T = q_T,$$

and the baroclinic stream function solves

$$-\Delta\psi_C + \frac{2}{R_d^2}\psi_C = q_C.$$

These are the two equations that we needed to solve to compute equilibrium states for the Euler equation and the single-layer quasigeostrophic equation cases.

In this approach, we solve the system by first forming q_T and q_C using the fact that $q_T = (q_1 + q_2)/2$ and $q_C = (q_1 - q_2)/2$. Then using our preexisting solvers, find the solutions ψ_T and ψ_C of the above equations. From these, we can form the stream functions for each layer using $\psi_1 = \psi_T + \psi_C$ and $\psi_2 = \psi_T - \psi_C$.

Having determined the correct form for the linearized energy constraint and how to solve the system of partial differential equations, we find that the algorithm is the same. For a given q_1, q_2, ψ_1 and ψ_2, find α, β, μ_1 and μ_2 so that the constraints (9.34), (9.32c), (9.32d) and (9.32e) are satisfied. Use these values in (9.33a) and (9.33c) to update the distributions q_1 and q_2. From these vorticity distributions, solve for ψ_1 and ψ_2 using one of the methods outlined above. We repeat this process until some appropriate convergence criterion is met. We applied the same criteria as given in section 3.3.

CHAPTER 10

TWO-LAYER QUASIGEOSTROPHIC OPTIMAL CLOSURE

In [39], McWilliams finds from direct numerical simulation of the stratified quasigeostrophic equation that the same sort of coherent vorticity structures emerge in longtime simulations as for the Euler equation and the single-layer quasigeostrophic equation. He further found that the coherent vortices prefer to form vertically aligned states, or in the language of geophysical fluids, they prefer to be purely barotropic.

The simplicity of the two-layer model makes it a good testing ground to study this barotropization problem. In this context, it is a little surprising that there is relatively little statical mechanical theories for the two-layer quasigeostrophic model. DiBattista and Majda developed an equilibrium theory for a square domain based on continuum methods [18]. They also extended the point vortex equilibrium theory to the two-layer system in the entire plane [19]. There has been no work on the nonequilibrium theory (at least that we are aware of).

We use the optimal closure procedure again. This time to develop a nonequilibrium statistical theory for the two-layer quasigeostrophic equation by using the point vortex idealization. Just as in the Euler and single-layer cases, we make a mean-field approximation. This approximation reduces the Liouville residual to an information theoretical residual on the two-layer quasigeostrophic equation so that once again, we see that the point vortices provide us with a vehicle to determine the residual on the original continuum equations. We then make a near equilibrium assumption and use this to turn our implicit trial densities to explicit densities with a resolved vector that respects the conserved quantities. In the near equilibrium regime, we also examine the rate of conversion of available potential energy into kinetic energy.

Having developed this nonequilibrium theory, we then look to study the barotropization of coherent vortices noted in the numerical simulations of McWilliams. To do this, we examine baroclinic perturbations of stable barotropic states. We apply the theory's prediction of potential energy transfer rates and compare it to direct numerical simulations. Finally, we will see how the closure predicts that the equilibration rate and available potential energy transfer rate depend on the inverse temperature β and the internal deformation radius R_d.

10.1 Two-Layer Closure

In this section, we use the optimal closure to develop a nonequilibirum mean-field theory for the point vortex idealization applied to the two-layer quasigeostrophic equation. We start with the general case and then simplify by making a near equilibrium assumption. This again allows us to take our implicit mean-field trial densities and reformulate them explicitly as well as reformulating the resolved vector to respect the conserved quantities. Finally, in the near equilibrium regime, we explore how the closure predicts the available potential energy flows into kinetic energy.

10.1.1 General Case

We take the trial densities for the vorticity in each layer to be the quasi-equilibrium distributions

$$\tilde{\rho}_1(x_1, y_1) = \exp\{[\lambda^T \mathbf{A}_1 - \beta\tilde{\psi}_1 - \alpha r_1^2]\Gamma_1 - \mu_1\}, \tag{10.1a}$$

$$\tilde{\rho}_2(x_2, y_2) = \exp\{[\lambda^T \mathbf{A}_2 - \beta\tilde{\psi}_2 - \alpha r_2^2]\Gamma_2 - \mu_2\}, \tag{10.1b}$$

where $r_k^2 = x_k^2 + y_k^2$, $\mathbf{x}_k = (x_k, y_k)$ is a point in the k^{th} layer, Γ_k is the total circulation in the k^{th} layer and ψ_1 and ψ_2 satisfy

$$-\Delta\tilde{\psi}_1 + \frac{1}{R_d^2}(\tilde{\psi}_1 - \tilde{\psi}_2) = q_1 \tag{10.1c}$$

$$-\Delta\tilde{\psi}_2 - \frac{1}{R_d^2}(\tilde{\psi}_1 - \tilde{\psi}_2) = q_2 \tag{10.1d}$$

where $q_k = \Gamma_k \tilde{\rho}_k$.

Furthermore, we have assumed that the vector of observables is of the form

$$\mathbf{A}(x_1, y_1, x_2, y_2) = \mathbf{A}_1(x_1, y_1) + \mathbf{A}_2(x_2, y_2) \tag{10.2}$$

where $\mathbf{A}_k$ is the component of the observable for the k^{th} layer. We can justify this assumption physically. The layers only interact through the displacement of the interface. As the stream functions of the top and bottom layer relate directly to the displacement of the fluid interface (see equations (9.4)), they capture the entirety of the two layers' interaction. Therefore, any interaction of the two layers must be through the stream functions. The above form of the observable vector follows from this.

As a result of this assumption, we are able to write the trial density for the entire system as the product measure

$$\tilde{\rho}(x_1, y_1, x_2, y_2) = \tilde{\rho}_1(x_1, y_2)\tilde{\rho}_2(x_2, y_2). \tag{10.3}$$

Again, this parallels the actual dynamics of the two-layer equations. The vorticity distributions (or point vortices) do not interact directly but only through the stream functions.

We have started with a mean-field form of trial density and we need to rewrite the Liouville residual to match it. We use a similar argument as before. Assume that q_1^N and q_2^N converge weakly to some continuum distributions q_1 and q_2, respectively. From this we conclude that $\psi_{ki} \approx \psi_k$. Therefore, for a function of the form

$$B^N(\mathbf{x}_{11}, \dots, \mathbf{x}_{2N}) = \sum_{k=1}^{2} \sum_{i=1}^{N} B(x_{ki}, y_{ki}),$$

we have

$$\{B^N, H^N\} = \sum_{k=1}^{2} \sum_{i=1}^{N} [B^N, \psi_{ki}]_{(x_{ki}, y_{ki})} \approx N \left([B_1, \psi_1]_{(x_1, y_1)} + [B_2, \psi_2]_{(x_2, y_2)} \right).$$

where $B_k = B(x_k, y_k)$.

Combining this with the product measure form of $\tilde{\rho}$, we find that the Liouville residual is

$$\begin{aligned}R &= (\partial_t + [\cdot,\psi_1]_{(x_1,y_1)} + [\cdot,\psi_2]_{(x_2,y_2)})(\log\tilde{\rho}_1 + \log\tilde{\rho}_2)\\ &= (\partial_t + [\cdot,\psi_1]_{(x_1,y_1)})\log\tilde{\rho}_1 + (\partial_t + [\cdot,\psi_2]_{(x_2,y_2)})\log\tilde{\rho}_2\\ &= R_1 + R_2,\end{aligned}$$

where we have used the fact that

$$[\tilde{\rho}_\ell,\psi_k]_{(x_k,y_k)} = 0,$$

for $\ell \neq k$. The resulting Liouville residual again takes the form of an information theoretic residual on the flow of the continuum dynamics. That is, we can think of the Liouville residual as the information lost by forcing our vorticity distributions to remain in our family of trial distributions.

The form of the Liouville residual is very revealing but needs to be expanded to actually be of use computationally. To do this we adopt a couple of conventions. First, for a given function $f(x,y)$, we denote by f_k its value on the k^{th} layer. That is, $f_k = f(x_k,y_k)$. Second, it is understood that in the advection term $[\cdot,\psi_k]$, the derivatives are with respect to x_k and y_k.

Using these conventions, expanding the Liouville residual for the k^{th} layer gives us

$$\begin{aligned}R_k = \Gamma_k(&\dot{\lambda}(\mathbf{A}_k - \mathbf{a}_k) - \dot{\beta}(\psi_k - \langle\psi_k|\tilde{\rho}\rangle) - \beta(\partial_t\psi_k - \langle\partial_t\psi_k|\tilde{\rho}\rangle) - \dot{\alpha}(r_k^2 - \langle r_k^2|\tilde{\rho}\rangle)\\ &+ \lambda[\mathbf{A}_k,\psi_k] - \alpha[r_k^2,\psi_k]).\end{aligned}$$

Summing the residual for the two layers and collecting common terms, we find the total Liouville residual is given by

$$\begin{aligned}R = {}&\dot{\lambda}(\Gamma_1(\mathbf{A}_1 - \mathbf{a}_1) + \Gamma_2(\mathbf{A}_2 - \mathbf{a}_2)) - \dot{\beta}(\Gamma_1\tilde{\psi}_1 + \Gamma_2\tilde{\psi}_2 - 2E)\\ &- \beta\left(\partial_t\Gamma_1\tilde{\psi}_1 + \partial_t\Gamma_2\tilde{\psi}_2 - \left\langle\partial_t\Gamma_1\tilde{\psi}_1|\tilde{\rho}\right\rangle - \left\langle\partial_t\Gamma_2\tilde{\psi}_2|\tilde{\rho}\right\rangle\right) - \dot{\alpha}(\Gamma_1 r_1^2 + \Gamma_2 r_2^2 - L^2)\\ &+ \lambda(\Gamma_1[\mathbf{A}_1,\tilde{\psi}_1] + \Gamma_2[\mathbf{A}_2,\tilde{\psi}_2]) - \alpha(\Gamma_1[r_1^2,\tilde{\psi}_1] + \Gamma_2[r_2^2,\tilde{\psi}_2]),\end{aligned}$$

where we have replaced the unknown true stream functions ψ_1 and ψ_2 with the trial stream functions $\tilde{\psi}_1$ and $\tilde{\psi}_2$, respectively.

We now have a Liouville residual in mean-field form that is compatible with the trial densities given by (10.1). In principle, we could now find the path $\lambda(t)$ that solves the constrained minimization problem

$$\begin{aligned}
&\min_{\lambda(0)=\lambda_0} \int_0^\tau \langle R^2 | \tilde{\rho} \rangle \, dt \quad \text{subject to} \\
&\quad \frac{1}{2}\left(\int_{\mathbb{R}^2} \tilde{\psi}_1 \tilde{q}_1 d\mathbf{x}_1 + \int_{\mathbb{R}^2} \tilde{\psi}_2 \tilde{q}_2 d\mathbf{x}_2 \right) = E, \\
&\quad \int_{\mathbb{R}^2} |\mathbf{x}_1|^2 \tilde{q}_1 d\mathbf{x}_1 + \int_{\mathbb{R}^2} |\mathbf{x}_2|^2 \tilde{q}_2 d\mathbf{x}_2 = L^2, \\
&\quad \int_{\mathbb{R}^2} \tilde{\rho}_1 d\mathbf{x}_1 = 1, \\
&\quad \int_{\mathbb{R}^2} \tilde{\rho}_2 d\mathbf{x}_2 = 1.
\end{aligned}$$

This gives us our general nonequilibrium theory.

10.1.2 Near Equilibrium Formulation

Just as in the Euler equations case, our trial densities are implicit in nature which complicates the already difficult problem of solving our constrained optimization problem. We have already seen one way to deal with both of these problems: Assume that we are near to a statistical equilibrium state. Specifically, we now assume that $|\lambda| << 1$ and that $\lambda = 0$ corresponds to an equilibrium. We will use this assumption to take the implicit trial densities given by (10.1) and write them in explicit form. Additionally, for these explicit trial densities, our optimization problem will reduce to solving a matrix Ricatti equation. The process is the same as in the Euler case. We write everything as expansions in λ and then use the energy and angular impulse constraints to write the perturbations of α and β as functions of λ. These are then used to write the stream function perturbations as a function of λ alone. This allows us to reduce the Liouville residual to a near equilibrium form which depends only on λ.

Using the small λ assumption, we write $\alpha = \alpha_{eq} - \alpha'$, $\beta = \beta_{eq} - \beta'$, $\mu_k = \mu_k^{eq} + \mu_k'$, $\tilde{q}_k = q_k^{eq} + q_k'$ and $\tilde{\psi}_k = \psi_k^{eq} + \psi_k'$, where all prime terms are $O(\lambda)$. Note that all averages are now taken with respect to the equilibrium density $\rho^{eq} = \rho_1^{eq}\rho_2^{eq}$.

Under the near equilibrium assumption, the trial densities become

$$\tilde{\rho}_k = [1 + \Gamma_k(\lambda\mathbf{A}_k - \beta_{eq}\psi_k' + \beta'\psi_k^{eq} + \alpha' r^2) - \mu_k']\rho_k^{eq} + O(|\lambda|^2).$$

From this we find that

$$q_k' = \Gamma_k\rho_k' = [\Gamma_k(\lambda\mathbf{A}_k - \beta_{eq}\psi_k' + \beta'\psi_k^{eq} + \alpha' r^2) - \mu_k']q_k^{eq},$$

and the stream functions then satisfy

$$\begin{aligned} -\Delta(\psi_1^{eq} + \psi_1') + \frac{1}{R_d^2}(\psi_1^{eq} + \psi_1' - \psi_2^{eq} - \psi_2') &= q_1^{eq} + q_1', \\ -\Delta(\psi_2^{eq} + \psi_2') - \frac{1}{R_d^2}(\psi_1^{eq} + \psi_1' - \psi_2^{eq} - \psi_2') &= q_2^{eq} + q_2'. \end{aligned}$$

It follows that ψ_1' and ψ_2' are related to q_1' and q_2' by

$$\begin{aligned} -\Delta\psi_1' + \frac{1}{R_d^2}(\psi_1' - \psi_2') &= q_1', \\ -\Delta\psi_2' - \frac{1}{R_d^2}(\psi_1' - \psi_2') &= q_2'. \end{aligned}$$

We require the trial distributions to satisfy the constraints on energy, angular momentum and the circulation in both layers:

$$\begin{aligned} &\frac{1}{2}\int_{\mathbb{R}^2} \tilde{\psi}_1\tilde{q}_1 + \tilde{\psi}_2\tilde{q}_2 \, d\mathbf{x} = E, \\ &\int_{\mathbb{R}^2} r^2(\tilde{q}_1 + \tilde{q}_2)\, d\mathbf{x} = L^2, \\ &\int_{\mathbb{R}^2} \tilde{q}_1 \, d\mathbf{x} = \Gamma_1, \\ &\int_{\mathbb{R}^2} \tilde{q}_2 \, d\mathbf{x} = \Gamma_2. \end{aligned}$$

In the near equilibrium regime this gives the following linearized constraints

$$\begin{aligned}
&\int_{\mathbb{R}^2} \psi_1' q_1^{eq} + \psi_2' q_2^{eq} \, d\mathbf{x} = \int \psi_1^{eq} q_1' + \psi_2^{eq} q_2' \, d\mathbf{x} = 0, \\
&\int_{\mathbb{R}^2} r^2 (q_1' + q_2') \, d\mathbf{x} = 0, \\
&\int_{\mathbb{R}^2} q_1' \, d\mathbf{x} = \int q_2' \, d\mathbf{x} = 0.
\end{aligned}$$

Using the expressions for q_1' and q_2', the two circulation constraints reduce to

$$\mu_k' = \lambda_k \mathbf{a}_k - 2\beta_{eq} E_k' + 2\beta' E_k^{eq} + \alpha' L_k^2,$$

where $\mathbf{a}_k = \langle \mathbf{A}_k \rangle$ and

$$E_k^{eq} = \frac{1}{2} \int_{\mathbb{R}^2} \psi_k^{eq} q_k^{eq} \, d\mathbf{x}, \quad E_k' = \frac{1}{2} \int_{\mathbb{R}^2} \psi_k' q_k^{eq} \, d\mathbf{x}, \quad L_k^2 = \int_{\mathbb{R}^2} r^2 q_k^{eq} \, d\mathbf{x}.$$

Therefore, the vorticity distribution perturbation for the k^{th} layer can be written

$$q_k' = [\lambda \Gamma_k (\mathbf{A}_k - \mathbf{a}_k) - \beta_{eq}(\Gamma_k \psi_k' - 2E_k') + \beta'(\Gamma_k \psi_k^{eq} - 2E_k^{eq}) + \alpha'(\Gamma_k r_k^2 - L_k^2)] q_k^{eq}. \quad (10.4)$$

Taking these expressions for q_1' and q_2' and substituting into our system for ψ_1' and ψ_2' gives

$$\begin{aligned}
-\Delta \psi_1' + \frac{1}{R_d^2}(\psi_1' - \psi_2') &= [\lambda^T \Gamma_1 (\mathbf{A}_1 - \mathbf{a}_1) - \beta_{eq}(\Gamma_1 \psi_1' - 2E_1') + \beta'(\Gamma_1 \psi_1^{eq} - 2E_1^{eq}) \\
&\quad + \alpha'(\Gamma_1 r^2 - L_1^{2,eq})] q_1^{eq}, \\
-\Delta \psi_2' - \frac{1}{R_d^2}(\psi_1' - \psi_2') &= [\lambda^T \Gamma_2 (\mathbf{A}_2 - \mathbf{a}_2) - \beta_{eq}(\Gamma_2 \psi_2' - 2E_2') + \beta'(\Gamma_2 \psi_2^{eq} - 2E_2^{eq}) \\
&\quad + \alpha'(\Gamma_2 r^2 - L_2^{2,eq})] q_2^{eq}.
\end{aligned}$$

Moving all terms with ψ_1' and ψ_2' to one side, we find that they must satisfy the linear system

$$T_1\psi_1' - \frac{1}{R_d^2}\psi_2' = [\lambda^T\Gamma_1(\mathbf{A}_1 - \mathbf{a}_1) + \beta'(\Gamma_1\psi_1^{eq} - 2E_1^{eq}) + \alpha'(\Gamma_1 r^2 - L_1^{2,eq})]q_1^{eq}$$
$$-\frac{1}{R_d^2}\psi_1' + T_2\psi_2' = [\lambda^T\Gamma_2(\mathbf{A}_2 - \mathbf{a}_2) + \beta'(\Gamma_2\psi_2^{eq} - 2E_2^{eq}) + \alpha'(\Gamma_2 r^2 - L_2^{2,eq})]q_2^{eq}$$

where $T_k f = -\Delta f + \frac{1}{R_d^2}f + \beta_k^{eq}q_k^{eq}(f - \langle f\rangle_k)$. We can write the whole thing in matrix-vector form

$$\begin{pmatrix} T_1 & -\frac{1}{R_d^2} \\ -\frac{1}{R_d^2} & T_2 \end{pmatrix}\begin{pmatrix}\psi_1' \\ \psi_2'\end{pmatrix} = \lambda^T\mathbf{u}_\mathbf{A} + \beta'\mathbf{u}_E + \alpha'\mathbf{u}_{L^2}, \tag{10.5}$$

where we have introduced the vectors

$$\mathbf{u}_\mathbf{A} = \begin{pmatrix}\Gamma_1(\mathbf{A}_1 - \mathbf{a}_1)q_1^{eq} \\ \Gamma_2(\mathbf{A}_2 - \mathbf{a}_2)q_2^{eq}\end{pmatrix}, \quad \mathbf{u}_E = \begin{pmatrix}(\Gamma_1\psi_1^{eq} - 2E_1^{eq})q_1^{eq} \\ (\Gamma_2\psi_2^{eq} - 2E_2^{eq})q_2^{eq}\end{pmatrix}, \quad \mathbf{u}_{L^2} = \begin{pmatrix}(\Gamma_1 r^2 - L_1^2)q_1^{eq} \\ (\Gamma_2 r^2 - L_2^2)q_2^{eq}\end{pmatrix}.$$

We again expect the stream function to look like a point vortex at the origin when very far away. This is fulfilled by the equilibrium stream functions ψ_1^{eq} and ψ_2^{eq} so that the far-field conditions on ψ_1' and ψ_2' are

$$\psi_1' \to 0, \quad \psi_2' \to 0$$

as $|\mathbf{x}| \to \infty$.

Let $\mathbf{G}^{tl}$ denote the inversion operator of the system (10.5). We can write

$$\begin{pmatrix}\psi_1' \\ \psi_2'\end{pmatrix} = \lambda\mathbf{G}^{tl}\mathbf{u}_A + \beta'\mathbf{G}^{tl}\mathbf{u}_E + \alpha'\mathbf{G}^{tl}\mathbf{u}_{L^2} \tag{10.6}$$

Since $\mathbf{G}^{tl}$, $\mathbf{u}_\mathbf{A}$, $\mathbf{u}_E$ and $\mathbf{u}_{L^2}$ are all predetermined, we only need to perform the inversion computation of each vector once.

Substituting the solutions for ψ_1' and ψ_2' into the energy and angular momentum constraints and noting that

$$2E_k' = \Gamma_k\left\langle\lambda G_k^{tl}\mathbf{u}_A + \alpha' G_k^{tl}\mathbf{u}_{L^2} + \beta' G_k^{tl}\mathbf{u}_E\right\rangle_k,$$

gives a system of linear equations for α' and β'

$$D_1 \begin{pmatrix} \alpha' \\ \beta' \end{pmatrix} = D_2 \lambda, \tag{10.7}$$

where D_1 is the 2×2 matrix

$$D_1 = - \begin{pmatrix} \sum_k \Gamma_k \left\langle r^2 P_k(\Gamma_k r^2) \right\rangle_k & \sum_k \Gamma_k \left\langle r^2 P_k(\Gamma_k \psi_k^{eq}) \right\rangle_k \\ \sum_k \Gamma_k \left\langle \psi_k^{eq} P_k(\Gamma_k r^2) \right\rangle_k & \sum_k \Gamma_k \left\langle \psi_k^{eq} P_k(\Gamma_k \psi_k^{eq}) \right\rangle_k \end{pmatrix}$$

and D_2 is the $2 \times m$ matrix

$$D_2 = \begin{pmatrix} \sum_k \Gamma_k \left\langle r^2 P_k \mathbf{A} \right\rangle_k \\ \sum_k \Gamma_k \left\langle \psi_k^{eq} P_k \mathbf{A} \right\rangle_k \end{pmatrix},$$

and we have introduced the notation $P_k F = (F - \langle F \rangle_k - \beta_{eq} \Gamma_k q_k^{eq} (G_k^{tl} \mathbf{u}_F - \left\langle G_k^{tl} \mathbf{u}_F \right\rangle_k)$.

Provided that D_1 is invertible, we can write

$$\alpha' = \sum_{i=1}^{m} \alpha_i' \lambda_i \quad \beta' = \sum_{i=1}^{m} \beta_i' \lambda_i$$

where the coefficients are given by the corresponding entries in the matrix $D_1^{-1} D_2$.

Using the chain rule we can write

$$\partial_t \psi_k' = \dot{\lambda}^T (\nabla_\lambda \psi_k' + \partial_{\beta'} \psi_k' \nabla_\lambda \beta' + \partial_{\alpha'} \psi_k' \nabla_\lambda \alpha')$$

so that

$$\partial_t \psi_k' = \sum_{i=1}^{m} \psi_{ki}' \cdot \dot{\lambda}_i, \tag{10.8}$$

where

$$\begin{aligned} \psi_{ki}' &= \partial_{\lambda_i} \psi_k' + \partial_{\beta'} \psi_k' \beta_i' + \partial_{\alpha'} \psi_k' \alpha_i' \\ &= G_k^{tl} \mathbf{u}_{A^i} + \beta_i' G_k^{tl} \mathbf{u}_E + \alpha_i' G_k^{tl} \mathbf{u}_{L^2}. \end{aligned} \tag{10.9}$$

We can now write our trial densities explicitly. From (10.7) we can compute α'_i and β'_i. Then using (10.6) and (10.9), we can compute the values of ψ'_{ki}. Finally, using (10.4) we compute q'_1 and q'_2 and add them to q_1^{eq} and q_2^{eq}, respectively, to get the trial densities.

Turning our attention to the Liouville residual, the near equilibrium assumption allows us to write

$$\begin{aligned}
R = {} & \dot{\lambda}^T[\Gamma_1(\mathbf{A}_1 - \mathbf{a}_1) + \Gamma_2(\mathbf{A}_2 - \mathbf{a}_2)] + \dot{\beta}'(\Gamma_1\psi_1^{eq} + \Gamma_2\psi_2^{eq} - 2E) \\
& - \beta_{eq}\partial_t(\Gamma_1\psi'_1 + \Gamma_2\psi'_2) + \dot{\alpha}'(\Gamma_1 r_1^2 + \Gamma_2 r_2^2 - L^2) \\
& + \lambda^T(\Gamma_1[\mathbf{A}_1, \psi_1] + \Gamma_2[\mathbf{A}_2, \psi_2^{eq}]) - \alpha_{eq}(\Gamma_1[r_1^2, \psi'_1] + \Gamma_2[r_2^2, \psi'_2]) \\
& + O(|\lambda|^2)
\end{aligned}$$

Plugging in the expressions for ψ'_k, $\partial_t\psi'_k$, β' and α' and dropping higher order terms then gives

$$R = \mathbf{U}^T\dot{\lambda} + \mathbf{V}^T\lambda \tag{10.10}$$

where

$$\begin{aligned}
U_i = {} & \Gamma_1(A_1^{(i)} - a_1^{(i)}) + \Gamma_2(A_2^{(i)} - a_2^{(i)}) + \alpha'_i(\Gamma_1 r_1^2 + \Gamma_2 r_2^2 - L^2) \\
& + \beta'_i(\Gamma_1\psi_1^{eq} + \Gamma_2\psi_2^{eq} - 2E) - \beta_{eq}(\Gamma_1\psi'_{1i} + \Gamma_2\psi'_{2i})
\end{aligned} \tag{10.11}$$

and

$$V_i = \Gamma_1[A_1^{(i)}, \psi_1^{eq}] + \Gamma_2[A_2^{(i)}, \psi_2^{eq}] - \alpha_{eq}(\Gamma_1[r^2, \psi'_{1i}] + \Gamma_2[r^2, \psi'_{2i}]) \tag{10.12}$$

Applying the near equilibrium version of the general closure theory, we have the matrices C, J and K given by

$$C = \left\langle \mathbf{U}\mathbf{U}^T \right\rangle, \quad J = \left\langle \mathbf{V}\mathbf{U}^T \right\rangle, \quad K = \left\langle \mathbf{V}\mathbf{V}^T \right\rangle,$$

where all averages are taken with respect to the equilibrium density $\rho_{eq} = \rho_1^{eq}\rho_2^{eq}$. The matrix D is given by

$$D = K + JC^{-1}J.$$

The paths of the average observables are then given by the linear system of equations

$$\dot{\mathbf{a}} = [J - M(t)]\lambda, \quad C\lambda = \mathbf{a},$$

where as before $M(t)$ is the solution to the Riccati differential equation

$$\dot{M} + MC^{-1}M + JC^{-1}M - MC^{-1}J = D, \quad M(0) = 0.$$

10.1.3 Available Potential Energy Conversion

We have seen that the root of baroclinic instability is the transference of available potential energy into kinetic energy. Even the work of Hogg and Stommel seeks to understand mechanisms of converting potential energy into kinetic. Therefore it is worth exploring what our optimal closure predicts about the flow of energy. Here we will look at the near equilibrium case and derive a matrix that governs the rate at which energy is converted from available potential energy into kinetic energy.

Recall the energy of the system can be written as

$$E = \int_{\mathbb{R}^2} \psi_T q_T + \psi_C q_C \, d\mathbf{x}.$$

This is the sum of barotropic and baroclinic energy. Since we are in an unbounded domain, the barotropic kinetic energy is infinite. However, the baroclinic kinetic energy is finite so that we can rewrite the second term as

$$E_c = \int_{\mathbb{R}^2} |\nabla\psi_C|^2 d\mathbf{x} + \frac{2}{R_d^2} \int_{\mathbb{R}^2} \psi_C^2 \, d\mathbf{x}.$$

The second of these terms is the available potential energy. Expanding about the equilibrium state, we find that the available potential energy is given by

$$APE = \frac{2}{R_d^2} \int_{\mathbb{R}^2} (\psi_C^{eq} + \psi_C')^2 \, d\mathbf{x}.$$

Now if $\psi_C^{eq} = 0$ (as is the case when $\Gamma_1 = \Gamma_2$) or, more generally, if

$$\int_{\mathbb{R}^2} \psi_C^{eq} \psi_C' \, d\mathbf{x} = 0,$$

then

$$APE = APE_{eq} + \frac{2}{R_d^2} \int_{\mathbb{R}^2} (\psi_C')^2 \, d\mathbf{x} = APE_{eq} + \frac{1}{2R_d^2} \int_{\mathbb{R}^2} (\psi_1' - \psi_2')^2 \, d\mathbf{x},$$

where APE_{eq} is the equilibrium available potential energy given by

$$APE_{eq} = \frac{2}{R_d^2} \int_{\mathbb{R}^2} (\psi_C^{eq})^2 \, d\mathbf{x}.$$

Using the fact that

$$\psi_k' = \sum_{i=1}^{m} \psi_{ki}' \lambda_i,$$

we can then write the total available potential energy as the quadratic form

$$APE = APE_{eq} + \frac{1}{2R_d^2} \sum_{i=1}^{m} \sum_{j=1}^{m} \lambda_i \lambda_j \int_{\mathbb{R}^2} (\psi_{1i}' - \psi_{2i}')(\psi_{1j}' - \psi_{2j}') \, d\mathbf{x}.$$

This leads us to define the matrix P where

$$P_{ij} = \frac{1}{R_d^2} \int_{\mathbb{R}^2} (\psi_{1i}' - \psi_{2i}')(\psi_{1j}' - \psi_{2j}') \, d\mathbf{x}. \tag{10.13}$$

so that the total available potential energy is given by

$$APE = APE_{eq} + \frac{1}{2} \lambda^T P \lambda. \tag{10.14}$$

Differentiating with respect to t gives us

$$\begin{aligned} \frac{d}{dt} APE &= \lambda^T P \dot{\lambda} \\ &= \lambda^T P C^{-1} (J - M) \lambda \end{aligned} \tag{10.15}$$

Therefore, the time-dependent matrix $PC^{-1}(J - M(t))$ governs the flow of available potential energy into kinetic energy and the rate relates back to λ, the coefficient of the resolved vector.

If the above conditions are not satisfied, then first two terms in the available potential energy expansion gives

$$APE = APE_{eq} + \frac{2}{R_d^2}\int_{\mathbb{R}^2} \psi_C^{eq}\psi_C' \, d\mathbf{x} = APE_{eq} + \frac{1}{2R_d^2}\int_{\mathbb{R}^2} (\psi_1^{eq} - \psi_2^{eq})(\psi_1' - \psi_2') \, d\mathbf{x}$$

where APE_{eq} is the same as above. This leads us to define the vector $\mathbf{p}$ where

$$p_i = \frac{1}{2R_d^2}\int_{\mathbb{R}^2} (\psi_1^{eq} - \psi_2^{eq})(\psi_{1i}' - \psi_{2i}') \, d\mathbf{x}.$$

In this case, the total available potential energy is given by

$$APE = APE_{eq} + \mathbf{p}^T\lambda.$$

Taking the time derivative, we find that

$$\frac{d}{dt}APE = \mathbf{p}^T C^{-1}(J - M)\lambda. \tag{10.16}$$

Here, the time-dependent vector $\mathbf{p}^T C^{-1}(J - M)$ governs the flow of the potential energy into kinetic energy. Comparing this to (10.15), we see that the matrix P has been replaced by the vector $\mathbf{p}$.

10.2 Two-Layer Application and Results

Rotating stratified fluids have been observed in numerical simulation to form coherent purely barotropic vorticity structures [39]. This “barotropization” is a three-dimensional analogue of the symmetrization problem we studied previously. In light of the division of energy given by (9.15), we may also view it as a preference for minimal potential energy states. As such the process is similar to baroclinic instability, in that it is one of the ways that the atmosphere or ocean converts available potential energy into kinetic energy.

We will use the above closure procedure to investigate the formation of these barotropic structures as well as to predict the rate of their formation. Specifically, we will look at baroclinic perturbations of the stable barotropic states. This can be viewed as the bookend of the traditional baroclinic instability as we are focused on the end stages of the evolution whereas the linear stability analysis of baroclinic instability focuses on the initial stages of the evolution. In addition, we will quantify the conversion of available potential energy into kinetic energy. To simplify our analysis, we restrict to the case of equal circulation in each layer so that $\Gamma_1 = \Gamma_2 = 1$.

10.2.1 Observables

In order to study the process of barotropization, we could consider elliptical clouds of point vortices and see how they interact. But we propose what we believe to be a more physically meaningful situation. Consider two like signed vorticity patches. One patch is in the top layer and the other is in the bottom layer. These two patches are given some initial separation distance and allowed to advect one another until they collapse into a single barotropic vortex cloud. This is reminiscent of the mechanism of the growth of unstable modes of baroclinic instability as discussed by Salmon in [48]. To investigate this problem a natural choice of observables is the separation of the center of the vortex clouds as measured along the x and y axes. That is, in the notation of the previous section, we take

$$A^1(x_1, x_2) = x_1 - x_2, \qquad A^2(y_1, y_2) = y_1 - y_2$$

so that the average resolved vector $\mathbf{a}$ gives us the difference in the first moments of the two vortex clouds

$$a^1 = \langle x|\rho_1\rangle - \langle x|\rho_2\rangle\,, \qquad a^2 = \langle y|\rho_1\rangle - \langle y|\rho_2\rangle$$

This choice of observables also has a nice interpretation in terms of the baroclinic and barotropic components. Note that we can write the center of vorticity as

$$\mathbf{B} = \int_{\mathbb{R}^2} \mathbf{x} \cdot (q_1 + q_2)\, d\mathbf{x} = 2\int_{\mathbb{R}^2} \mathbf{x} \cdot q_T\, d\mathbf{x}$$

so that the center of vorticity is (twice) the center of the barotropic vorticity. Taking the average of our above observables gives us (in vector form)

$$\int_{\mathbb{R}^2} \mathbf{x} \cdot (q_1 - q_2)\, d\mathbf{x} = 2 \int_{\mathbb{R}^2} \mathbf{x} \cdot q_C \, d\mathbf{x}$$

so that our observable choice corresponds to (twice) the center of the baroclinic vorticity.

10.2.2 Results

We again compare the optimal closure to the mean of an ensemble of direct numerical simulations. Since the truth is an average of runs, it is actually an approximation of the true evolution. As such, the EDNS curves are guides to the true evolution and each one really has an accompanying sampling error. See section 6.2 for a more thorough discussion. To produce these curves, we randomly generated 40 different initial ensembles from the same distributions and ran each of these forward in time according to the system of differential equations given by (9.23). These ensembles consisted of 1000 vortices in the top layer and 1000 vortices in the bottom layer. We fixed the total circulation $\Gamma = 2$ which was evenly divided between the layers ($\Gamma_1 = \Gamma_2 = 1$). Each of the 2000 point vortices had strength $\gamma = 10^{-3}$. The system was advanced in time using the standard Runge-Kutta 4th order scheme with a step size of $\Delta t = 10^{-2}$. The step size was chosen because it was used in the single-layer case and, generally, the changes in conserved quantities were not significant ($< 10^{-6}$). However, there were more violations of this than in the single-layer case but remained fairly rare.

To generate the initial clouds of point vortices, we drew samples from a two bivariate normal random variable. The two distributions must be related in a certain way to preserve the various conserved quantities. Since the center of vorticity is conserved and is identically zero, we must have that

$$\int_{\mathbb{R}^2} \mathbf{x} q_1 \, d\mathbf{x} = -\int_{\mathbb{R}^2} \mathbf{x} q_2 \, d\mathbf{x}.$$

Therefore if the clouds are separated by a distance $2s$ along the x-axis, the two normal distributions must have means $(s, 0)$ and $(-s, 0)$. Furthermore, if we fix the angular impulse at $L^2 = 4$ and divide it equally among the layers, then the variance of the normal random

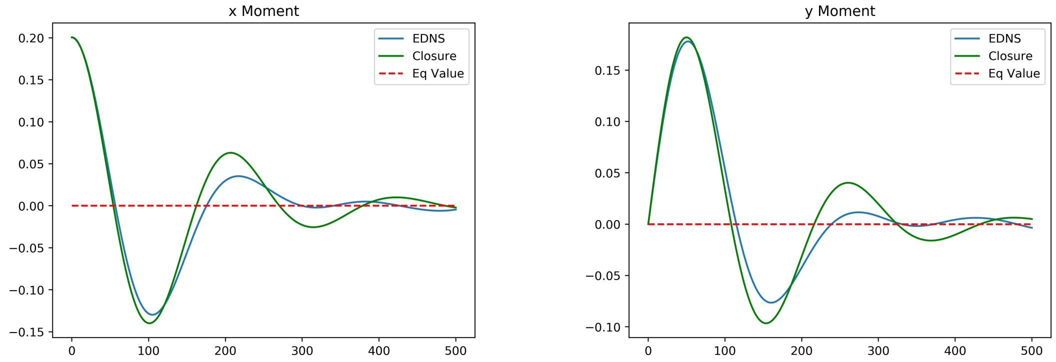

Figure 10.1: EDNS compared to optimal closure for case 1 of the two-layer quasigeo-strophic equation. The initial conditions are $a_1 = 0.2$ and $a_2 = 0.0$ and $R_d = 1.0$. The closure captures the first peak well and overestimates the second. This is a common trend among smaller perturbations. There is good agreement between the two on the time taken to equilibrate.

variables must decrease as the separation distance increases. Specifically, the trace of the covariance matrix must equal $2 - s^2$. We took the distributions to be radially symmetric so that the covariance matrix was

$$\Sigma = \begin{pmatrix} 1 - \frac{s^2}{2} & 0 \\ 0 & 1 - \frac{s^2}{2} \end{pmatrix}. \tag{10.17}$$

This fully defines the two distributions from which we drew samples.

10.2.2.1 Observable Prediction

Figures 10.1, 10.2, 10.3 and 10.4 give the plots of the predicted observable paths and the plots of the EDNS observable paths with $R_d = 1.0$ and initial separations of 0.2, 0.4, 0.6 and 0.8, respectively. Table 10.1 gives the relative error and peak error as described in section 6.2. In the first three cases, the closure does a good job predicting the magnitude of the first peak as well as the second and sometimes even the third peak. We see the same phase difference between the closure and the EDNS as in the Euler and single-layer results with the closure rotating slightly faster than the EDNS. We also see that the closure actually expects larger variations for the second and third peaks for smaller departures from equilibrium suggesting that there is some range at which the merging process is faster than

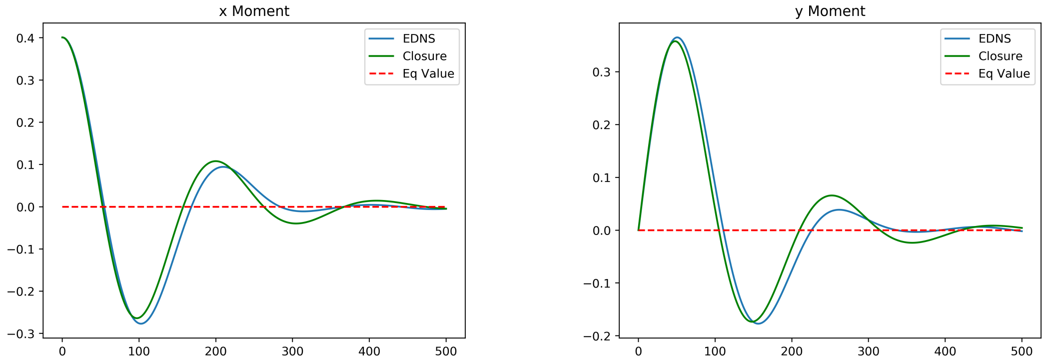

Figure 10.2: EDNS compared to optimal closure for case 2 of the two-layer quasigeo-strophic equation. The initial conditions are $a_1 = 0.4$ and $a_2 = 0.0$ and $R_d = 1.0$. The closure predicts each peak well. The equilibration time scale agrees with the EDNS. The phase difference is not as noticeable in this case.

Observable	Init Cond	Abs Peak Err	Rel Peak Err	Max Abs Err	Rel Err
a_1	0.2	1.01262e-02	7.80894e-02	3.31798e-02	1.65477e-01
a_2	0.0	3.98510e-03	2.23927e-02	3.16776e-02	1.78000e-01
a_1	0.4	1.30084e-02	4.69825e-02	5.45266e-02	1.36017e-01
a_2	0.0	7.25209e-03	1.98663e-02	4.52622e-02	1.23991e-01
a_1	0.6	4.88576e-02	1.20704e-01	1.26589e-01	2.11290e-01
a_2	0.0	2.48602e-02	4.57205e-02	1.17588e-01	2.16257e-01
a_1	0.8	1.13183e-01	2.17730e-01	2.55321e-01	3.19059e-01
a_2	0.0	5.55970e-02	7.75434e-02	2.47772e-01	3.45578e-01

Table 10.1: Absolute and relative errors of the closure compared to EDNS for the two-layer quasigeostrophic equation with deformation radius 1.0. Peak error is the difference between the first extreme values occurring after $t = 0$. Just as for the Euler and single-layer cases, the peak error is consistently better than the relative error due to the closure result rotating faster than the EDNS.

the closure is predicting. The last case we start to see the closure struggle with the peak error breaking 20% and the relative error nearly hitting 35%.

Figures 10.5, 10.6 and 10.7 are similar plots but with $R_d = 2.0$ and initial separations of 0.2, 0.3 and 0.5, respectively. Table 10.2 gives the error values for these cases. Here, we see the closure do well in the first case, where it captures the first and second peaks well, adequately in the second case, where it captures the first peak well and is not great on the second peak, and badly in the third case, where it completely misses the second peak and the first peak of a_1 but does get the first peak of a_2. The degradation of performance is far faster here with regard to separation distance.

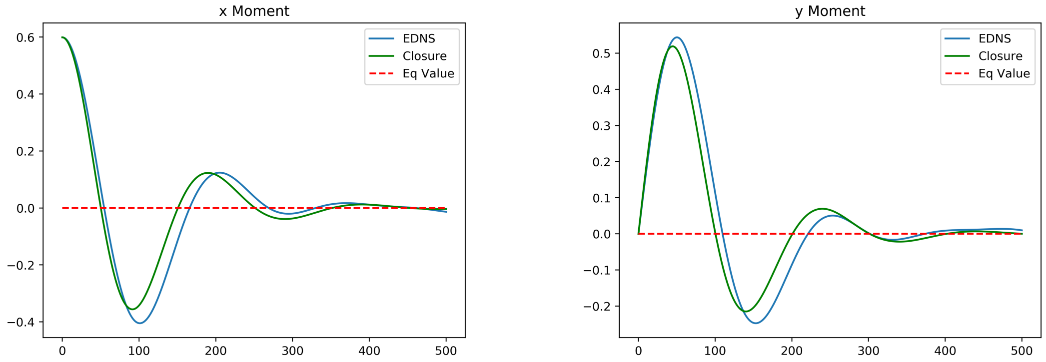

Figure 10.3: EDNS compared to optimal closure for case 3 of the two-layer quasigeo-strophic equation. The initial conditions are $a_1 = 0.6$ (x moment) and $a_2 = 0.0$ (y moment) and $R_d = 1.0$. The first peaks are captured well by the closure with the a_1 peak being somewhat underestimated. The closure starts to struggle with subsequent peaks for a_2. Interestingly, the closure does a better job with the second x peak. The equilibration time is still roughly the same.

Observable	Init Cond	Abs Peak Err	Rel Peak Err	Max Abs Err	Rel Err
a_1	0.2	4.05523e-03	2.52919e-02	6.59596e-02	3.29826e-01
a_2	0.0	2.22700e-05	1.18879e-04	6.26326e-02	3.34326e-01
a_1	0.3	3.31944e-02	1.30447e-01	1.42038e-01	4.73636e-01
a_2	0.0	9.80810e-03	3.42655e-02	1.38156e-01	4.82545e-01
a_1	0.5	1.32657e-01	3.09987e-01	3.49993e-01	6.99481e-01
a_2	0.0	4.66988e-02	9.74623e-02	3.56236e-01	7.43263e-01

Table 10.2: Absolute and relative errors of the closure compared to EDNS for the two-layer quasigeostrophic equation with deformation radius 2.0. Peak error is the difference between the first extreme values occurring after $t = 0$. The peak error and relative error grows much faster with separation than for $R_d = 1.0$.

There are a few possible sources of problems for the closure in addition to the normal reasons (needing more resolved variables and too far from equilibrium). The first is how the deformation radius and geometry affect the ratio of the concentration and magnitude of strain placed upon the cloud in a layer. The second is how changing the deformation radius affects the equilibrium state for a fixed initial setup.

Since the deformation radius is an interaction range, we expect that the larger deformation radius would produce more mixing and a better result. However, recall that the

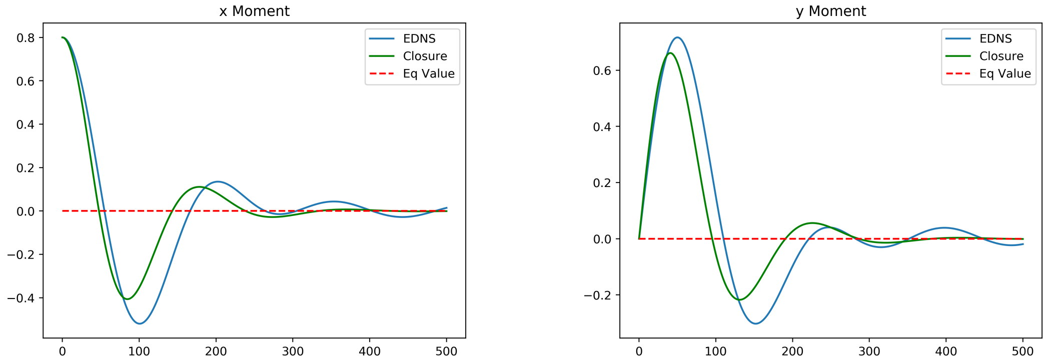

Figure 10.4: EDNS compared to optimal closure for case 4 of the two-layer quasigeo-strophic equation. The initial conditions are $a_1 = 0.8$ (x moment) and $a_2 = 0.0$ (y moment) and $R_d = 1.0$. The closure significantly underestimates the first peaks as well as the second peak of the y moment. The time scale to equilibrate is still roughly the same although it appears that the closure is shorter than the EDNS.

stream functions satisfy the equations

$$\begin{aligned} -\Delta\psi_1 + \frac{1}{R_d^2}(\psi_1 - \psi_2) &= q_1, \\ -\Delta\psi_2 - \frac{1}{R_d^2}(\psi_1 - \psi_2) &= q_2. \end{aligned}$$

Within each layer, the point vortex cloud is initialized from a radially symmetric normal random variable which is itself an equilibrium distribution. Therefore, each layer viewed separately from the other is in equilibrium. For a fixed initial condition, increasing the deformation radius has no effect on the magnitude of ψ_C since this is determined by the magnitude of q_C. Therefore, the interaction terms in these equations (that is, the forces causing variations from equilibrium within each layer) scale like $1/R_d^2$ for a fixed layer circulation. So we see that increasing the deformation radius actually decreases the interaction necessary for relaxation to the purely barotropic equilibrium.

Physically, the internal deformation radius R_d relates to the length scales on which the interface between the two layers deform with $R_d = \infty$ corresponding to a rigid or immovable interface. This means that as R_d increases and the vortex cloud size remains fixed, the clouds are unable to detect any disturbance in the interface and thus remain in their internal equilibrium.

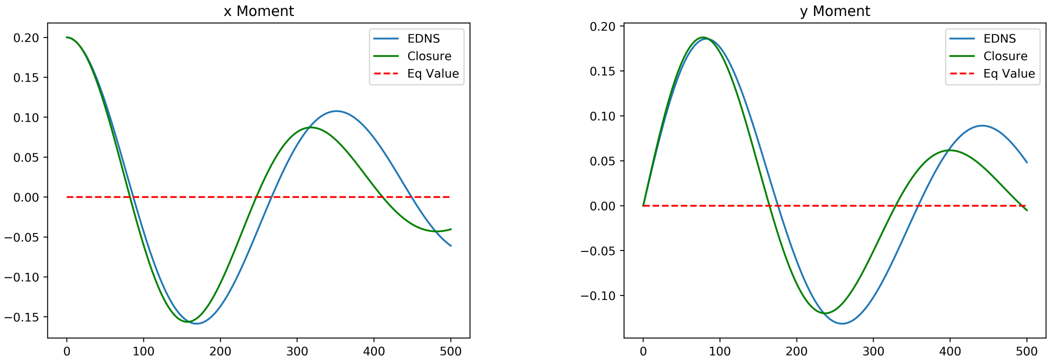

Figure 10.5: EDNS compared to optimal closure for case 5 of the two-layer quasigeo-strophic equation. The initial conditions are $a_1 = 0.2$ (x moment) and $a_2 = 0.0$ (y moment) and $R_d = 2.0$. The closure predicts the magnitude of the first peaks better than the corresponding $R_1 = 1.0$ case. The second peaks are underestimated. The simulation is not long enough to determine whether the equilibration times match.

The geometry of our setup and the conservation of angular impulse also increase the concentration of the vortex in each layer. As was stated in our discussion of the setup, the size of the vortex in each layer decreases as the separation distance increases. For a fixed angular impulse, the size of the vortex cloud in each layer is $\sqrt{(L^2 - 2s^2)/2}$ where s denotes the initial separation of the clouds. What we see is that as the square of the separation distance grows, the cloud size decreases. Indeed, this length scales goes to zero as s^2 approaches L^2 so that the clouds appear more like point vortices to one another in this limit.

This is a potential problem for our theory. Recall that within each layer, the distributions are in an equilibrium state. If the strain generated by the other vortex cloud is not sufficiently strong, then there is nothing to cause the equilibration of the system. This is similar to what McWilliams observed in his two-dimensional turbulence simulations [40]. The long lived vorticity structures could be traced back to a large value in the initial vorticity distribution. So the more concentrated a vortex, the more likely it is to persist. McWilliams argued that the increased concentration of the initial vorticity increases the strain required to disperse the patch. In our context, one patch must be strained sufficiently by the other in order to barotropize. However, increasing the separation distance increases the concentration of the vorticity and reduces the strain due to the patch in the

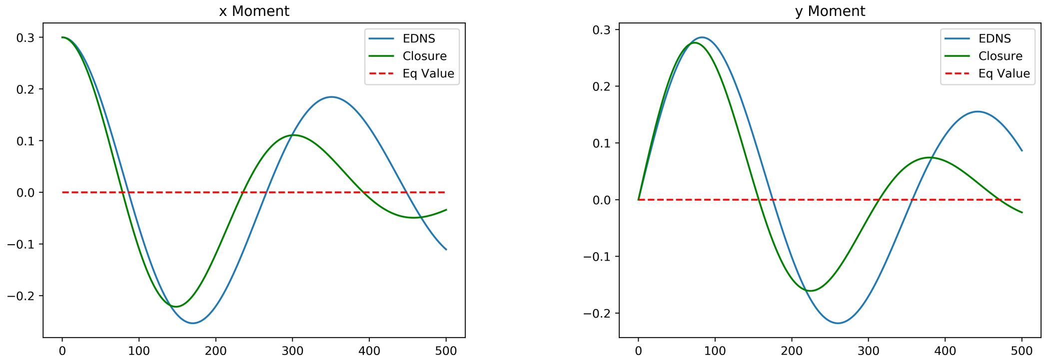

Figure 10.6: EDNS compared to optimal closure for case 6 of the two-layer quasigeo-strophic equation. The initial conditions are $a_1 = 0.3$ (x moment) and $a_2 = 0.0$ (y moment) and $R_d = 2.0$. The initial peaks predicted reasonably well but the second peaks are drastically underestimated. The results are comparable to the $R_d = 1.0$ case with twice the initial separation.

other layer. Increasing the deformation radius further acts to reduce the strain by reducing the shearing velocity.

The other issue has to do with how increasing the deformation radius affects the final equilibrium state. Let us fix a separation distance and, thereby, an initial distribution. As the deformation radius is increased, the total energy in the system increases. Physically, this is because the vortex cloud has a larger range of effect and deforms the interface over a larger distance. As a result, the value of β_{eq} decreases and the final equilibrium state is more concentrated. For initial separation 0.2, $\beta \approx -0.487$ when $R_d = 1.0$ and $\beta \approx -0.932$ when $R_d = 2.0$. The difference is more pronounced as the initial separation is increased. For initial separation 0.3, $\beta \approx -1.08$ when $R_d = 1.0$ and $\beta \approx -2.03$ when $R_d = 2.0$. It follows that the initial state moves further away from equilibrium as the deformation radius increases.

It is unclear whether any of these are the reason for the poor predictive result of the closure in this case. Other likely causes are that this is too far from equilibrium or we are being too drastic in our variable reduction and need to introduce more observables, that is, our model is too crude.

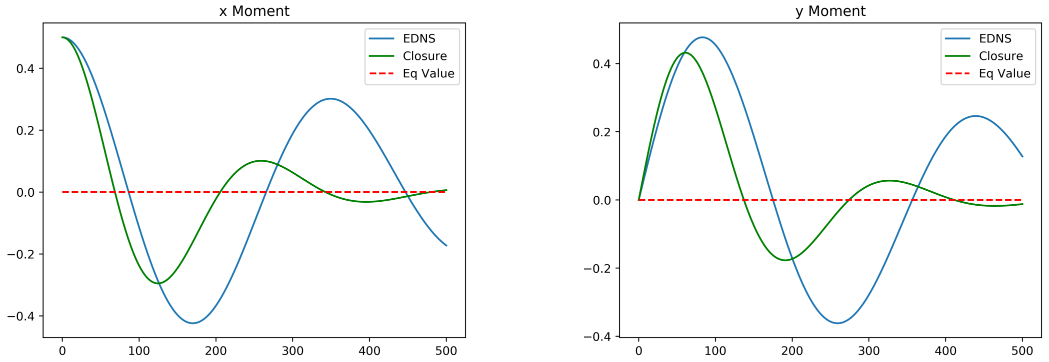

Figure 10.7: EDNS compared to optimal closure for case 7 of the two-layer quasigeo-strophic equation. The initial conditions are $a_1 = 0.5$ (x moment) and $a_2 = 0.0$ (y moment) and $R_d = 2.0$. The closure completely fails to capture the initial peaks and appears to significantly underestimate the equilibration time scale as the closure curve has only minor fluctuations by time 500 whereas the EDNS curve still has significant oscillations about the equilibrium value. For $R_d = 1.0$, the closure still had decent results with an initial separation of 0.6.

10.2.2.2 Available Potential Energy Prediction

We now turn our attention to the conversion of available potential energy to kinetic energy and how the closure compares with the underlying point vortex dynamics. First note that based on the definition (9.16), we can compute the available potential energy of the point vortex system as

$$APE_{EDNS} = \frac{\gamma^2}{8\pi^2 R_d^2} \int_{\mathbb{R}^2} \left(\sum_{i=1}^{N} K_0(k_d|\mathbf{x} - \mathbf{x}_{1i}) - K_0(k_d|\mathbf{x} - \mathbf{x}_{2i}|) \right)^2 d\mathbf{x}.$$

This can be easily be computed numerically. Furthermore, using finite differences, we can get an approximation of the rate of conversion of available potential energy into kinetic energy. Note that, because we have used finite differences to approximate the rate of conversion for the EDNS curves, the curves are quite rough and appear to be “stochastic” in nature. This is not the case. The roughness is the result only of the finite difference approximation. It should also be noted that sampling error is present in these curves as well as a result of the finite number of ensemble runs. However, this would be a smooth error and does not contribute to the rough appearance of the potential energy conversion curves.

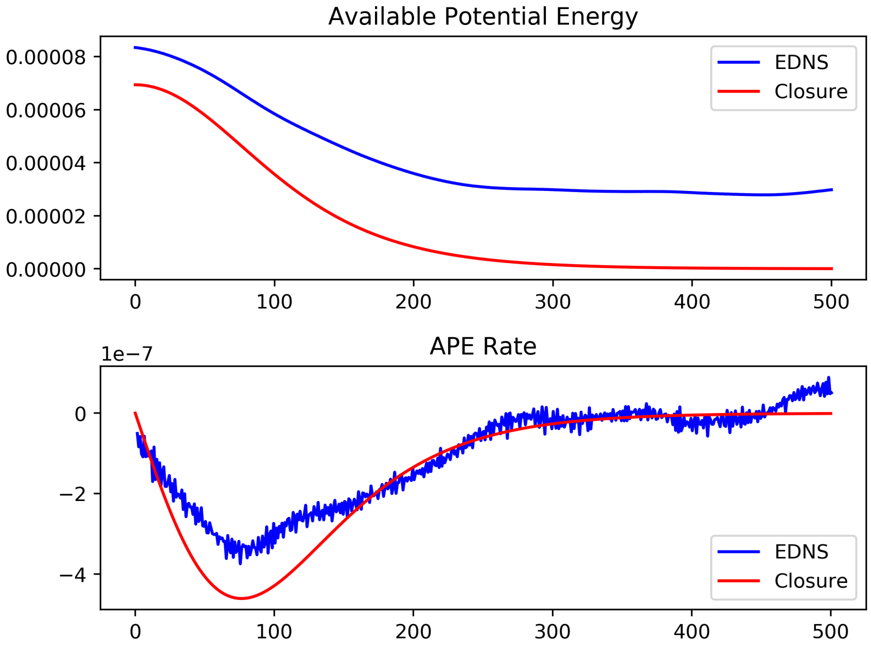

Figure 10.8: Predicted available potential energy and rate of transfer of the closure compared to EDNS for case 1. The initial conditions are $a_1 = 0.2$ and $a_2 = 0.0$ and $R_d = 1.0$. The lack of smoothness in the EDNS APE rate curve is the result of using finite differences to approximate the rate. The rough agreement between the rate curves and the scale of the energy values suggests that the discrepancy in the total APE curves is the result of sampling error. The closure predicts the time scale of energy transfer well.

Figures 10.8, 10.9, 10.10 and 10.11 compare the available potential energy calculations for the direct point vortex numerics to those predicted by the closure as detailed in section 10.1.3 for cases 1, 2, 3 and 4 as given above. Figures 10.12, 10.13 and 10.14 give the same comparison for cases 5, 6 and 7.

The results of the first four cases are in line with the closures predictive ability for the resolved vector. We see that the closure does a reasonable job predicting the total potential energy and the rate of conversion for case 2. Given the “wobbliness” of the total APE EDNS curves in case 1 and that the rate EDNS curve matches the closure curve reasonably well, it seems likely that the closure performs well in case 1 and that the significant differences are a result of the scale and sampling error. Case 3 we see the closure start to struggle. The total potential energy curve looks pretty good but the predicted peak rate is nearly twice that of the EDNS curve. In case 4, we start to see significant discrepancies in the potential energy curve as well as the rate curve—the initial APE prediction is 1.5 times more than

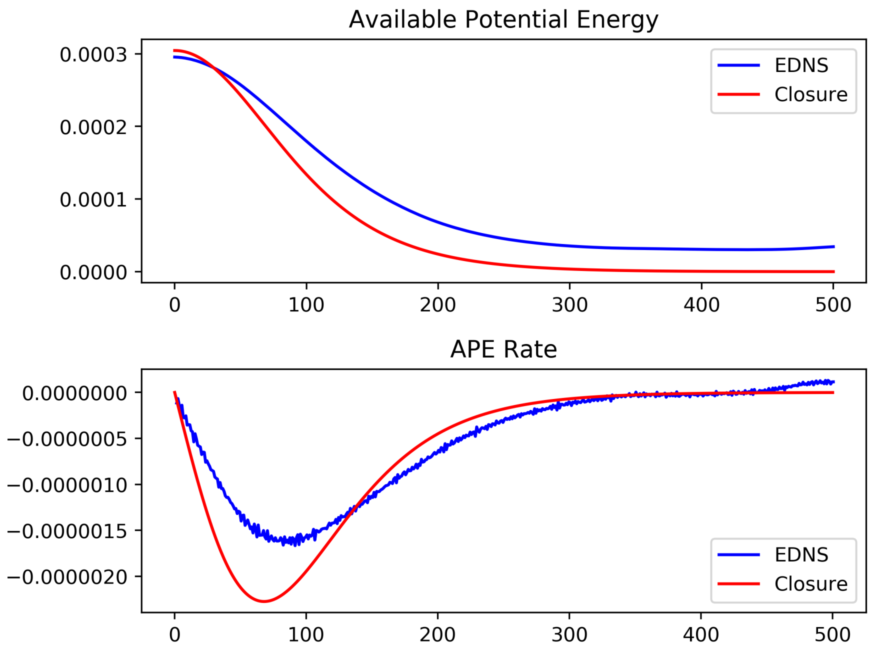

Figure 10.9: TPredicted available potential energy and rate of transfer of the closure compared to EDNS for case 2. The initial conditions are $a_1 = 0.4$ and $a_2 = 0.0$ and $R_d = 1.0$. The total APE and rate of transfer are captured well by the closure as is the time scale over which the energy transfer occurs.

the EDNS and the peak rate is more than 3 times as large. We do note that the closure predicts the time scale for potential energy conversion for these four cases reasonably well although it consistently predicts a shorter time scale than the EDNS.

In the last three cases, we see even more emphatically that the closure struggles with larger deformation radii. In case 6, we see something similar to case 3, where the total potential energy is captured adequately but the conversion rate is not—the maximum rate of the closure is more than twice the EDNS rate. On top of that, we see that the conversion time scale is not well captured at all. With case 5, we see the closure predicts the total potential energy well to start with, and then, around time 150, the two curves diverge with the EDNS curve decreasing much more slowly than the closure. Since the scales are small and both the EDNS total and rate curves exhibit some wobbling, it is likely that a significant portion of this error is sampling error. However, given the struggles of the closure in case 6, it is hard to argue that even the majority of the error is the result of a finite number of ensembles. Case 7 we see the same behavior as with the resolved variable prediction—the

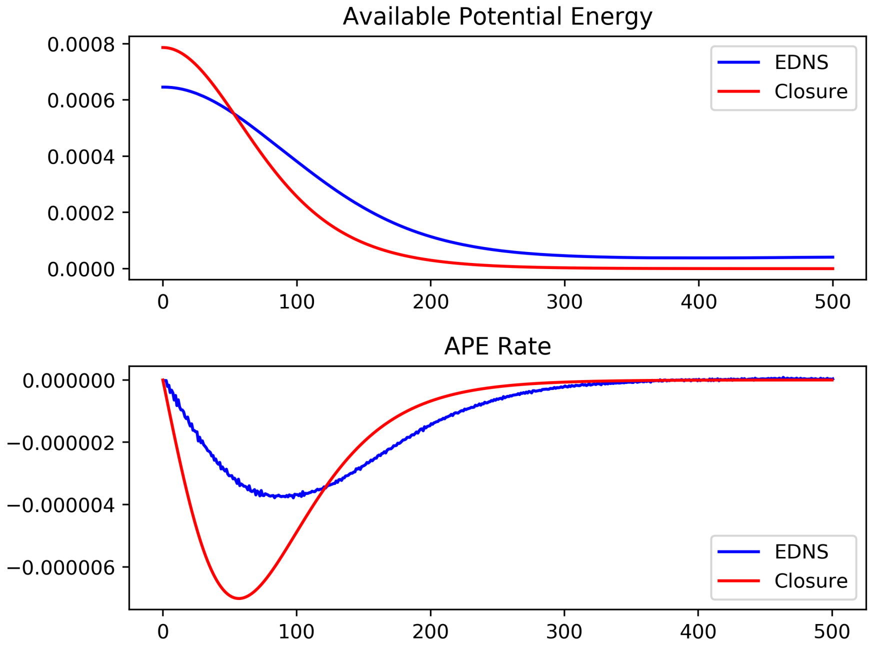

Figure 10.10: Predicted available potential energy and rate of transfer of the closure compared to EDNS for case 3. The initial conditions are $a_1 = 0.6$ and $a_2 = 0.0$ and $R_d = 1.0$. The closure total APE curve is reasonable. However, the closure clearly predicts the transfer of APE at a higher rate than the EDNS. The closure peaks at roughly twice the EDNS minimum. We also see that the time scale is slightly shorter for the closure than the EDNS but still a good estimate.

closure fails completely. The total initial potential energy is twice the EDNS value, the maximum rate is more than six times the EDNS rate and the potential energy EDNS curve has barely started to level off at the end of the simulation whereas the closure curve is more or less flat by time 300 so that the time scale is not even close to well approximated. As a small positive, we note that the closure has picked up that the time scales of conversion are longer with a larger deformation radius. Comparing case 1 and case 5 which both start with $a_1 = 0.2$ and $a_2 = 0.0$, we see that for $R_d = 1.0$, potential energy conversion has stopped by time 300, whereas for $R_d = 2.0$ only near the end of the simulation at time 500 has the conversion rate returned nearly to 0.

The explanation for the struggle of the closure at larger deformation radii with the available potential energy prediction are likely the same as that for the resolved variables: Increasing the deformation radius moves a fixed initial distribution further from equilibrium, inability of the reduced model to pick up insufficient strain on the vorticity patches,

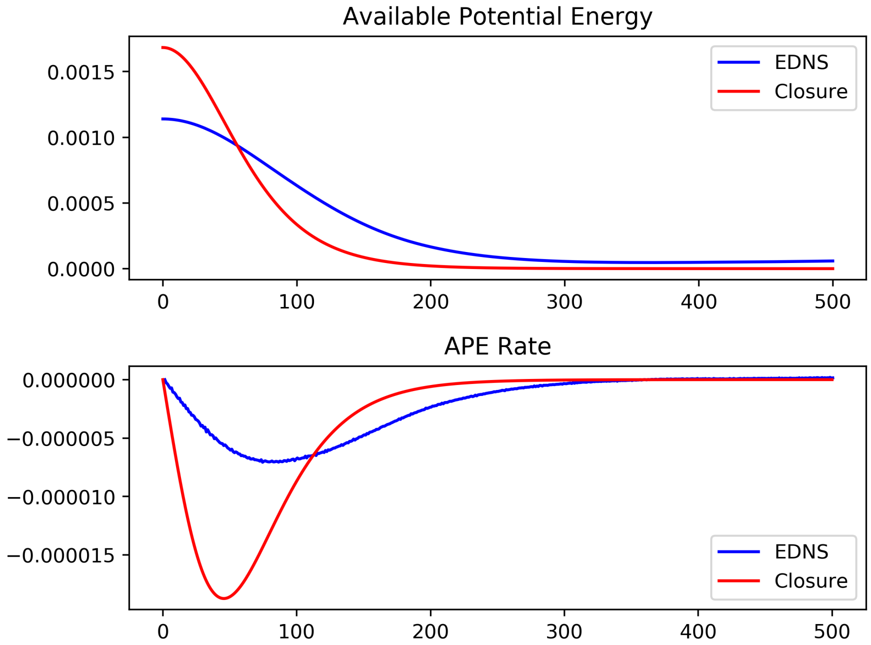

Figure 10.11: Predicted available potential energy and rate of transfer of the closure compared to EDNS for case 4. The initial conditions are $a_1 = 0.8$ and $a_2 = 0.0$ and $R_d = 1.0$. The closure predicts neither the rate nor the total energy well in this case. The starting APE total is roughly 1.5 times that of the EDNS and the peak rate is about 4 times larger. The time scale the closure predicts for the transfer is obviously shorter than the EDNS but not as off as the total APE and rate.

insufficient resolved variables or the failure of the near equilibrium approximation.

10.2.3 Parameter Dependence

We now use the closure to examine the dependence of the barotropization or equilibration rate and the available potential energy transfer rate on the inverse temperature β and the internal deformation radius R_d. Just as in the Euler equation and single-layer equation case, the C and K matrices are diagonal with equal entries so that the M matrix is diagonal with equal entries. Therefore the eigenvalues of M (or its entries) describe the rate at which the observables dissipate. Given the nature of the observables, we can also call this a barotropization rate.

Figure 10.15 gives a plot of the repeated eigenvalue of M as a function of β with the deformation radius fixed at 1.0, 2.0 and 4.0. We see again that the equilibration rate increases as β decreases and is trending toward infinity as β approaches -8π. Physically,

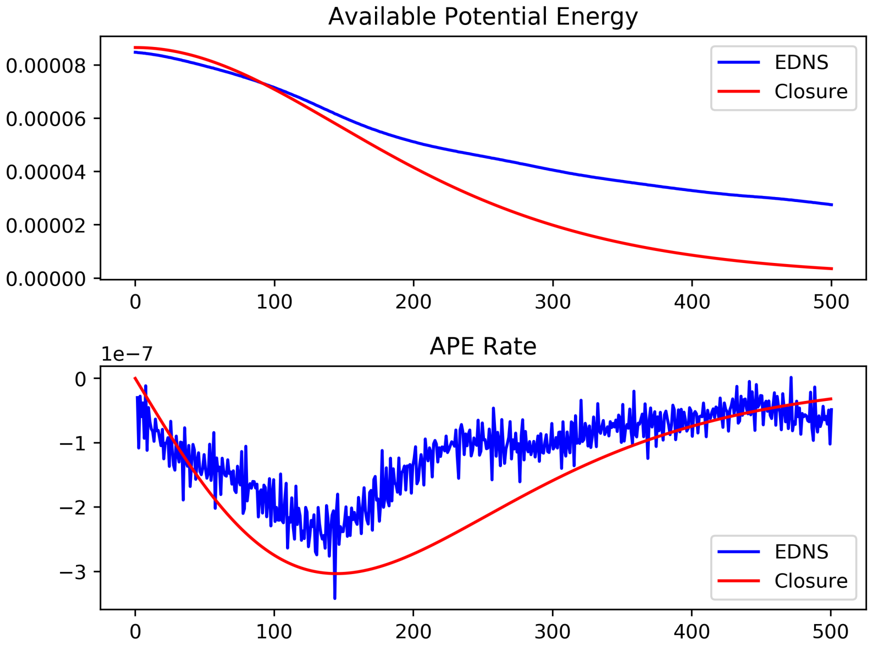

Figure 10.12: Predicted available potential energy and rate of transfer of the closure compared to EDNS for case 5. The initial conditions are $a_1 = 0.2$ and $a_2 = 0.0$ and $R_d = 2.0$. Due to the scale of the energy and the sampling error it is difficult to definitvely evaluate the closure. However, there does seem to be reasonable agreement for both the total and rate curves. The closure seems to predict the transfer time scale well.

this means that the barotropization occurs more rapidly the more concentrated or peaked the final state. As $\beta \to -8\pi$, the equilibrium distribution resembles more and more a purely barotropic point vortex. In this limit, this is the only admissible state so that everything immediately collapses. This resembles both the Euler and single-layer case.

In the limit $\beta \to \infty$, we see a different behavior than the Euler and single-layer cases. As β increases, the equilibration decreases for awhile until it hits a minimum then begins to increase again. The minimum value and the β value for which it occurs depends on the deformation radius, but all three curves exhibit this behavior. This means that the after the minimum β value, the more uniformly distributed the vorticity in the final equilibrium state, the more quickly the barotropization. This is an interesting prediction and we have no obvious physical justification for it.

Figure 10.16 depicts the relationship between the deformation radius and the barotropization rate for several different β values. Here we see that the rate of barotropization

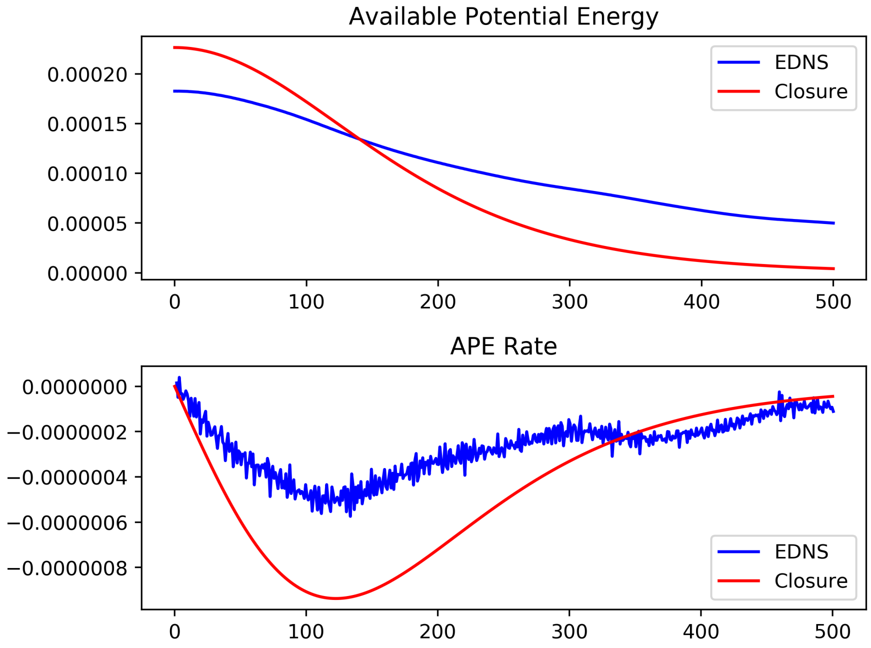

Figure 10.13: Predicted available potential energy and rate of transfer of the closure compared to EDNS for case 6. The initial conditions are $a_1 = 0.3$ and $a_2 = 0.0$ and $R_d = 2.0$. The total APE curve is not unreasonable but the peak APE rate is half of what is predicted. The closure adequately captures the time scale of transfer.

decreases as we increase the deformation radius. Since the $1/R_d^2$ is the interaction coefficient of the two layers, this is the expected relationship. That is, as we decrease the interaction strength of the the two layers, the process of vertical symmetrization takes longer. Perhaps the only surprising thing in this plot is that the equilibration rate does not approach zero as R_d approaches zero. The reason for this is that, in the limit of $R_d \to 0$, motion does not cease. In fact, we recover the Euler equation in this limit. Recall that the internal deformation radius is given by

$$R_d = \frac{\sqrt{g'H}}{f_0},$$

where f_0 is f-plane approximation of the Coriolis force, H is the depth of either layer and g' is the reduced gravity given by

$$g' = \frac{g(\rho_2 - \rho_1)}{\rho_1},$$

where ρ_1 and ρ_2 are the mass densities of the fluid in each layer. Physically, the limit of

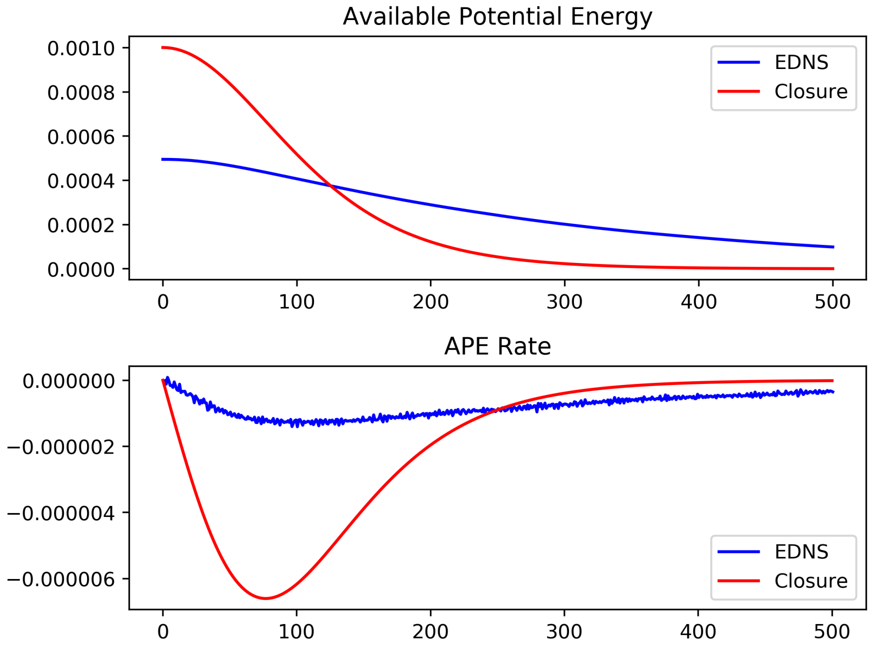

Figure 10.14: Predicted available potential energy and rate of transfer of the closure compared to EDNS for case 7. The initial conditions are $a_1 = 0.5$ and $a_2 = 0.0$ and $R_d = 2.0$. The closure fails to accurately predict the total APE, the peak rate and the time scale.

R_d going to zero can only be the result of the reduced gravity going to zero. This can only happen if the difference in fluid density tends to zero. Hence, we recover the single-layer quasigeostrophic equation. In our case, we have used the rigid lid approximation and so set the external deformation radius to infinity. Therefore, we get the Euler equations in the limit R_d going to zero.

To explore the available potential energy transfer rate dependence on the parameters, we can use the eigenvalues of the matrix $-PC^{-1}M$. We have observed numerically that the matrix P given by (10.13) is diagonal for our choice of observables. From this and the fact that C^{-1} and M are also diagonal and the fact that J is antisymmetric, we see that the matrix $PC^{-1}(J - M)$ is composed of an antisymmetric piece given by $PC^{-1}J$ and a diagonal piece given by $-PC^{-1}M$. The antisymmetric part can be interpreted as the transfer of potential energy from one observable to the other and, therefore, has no effect on the transfer rate. This manifests as the fact that $\lambda^T B \lambda = 0$ for any antisymmetric matrix B and real vector λ. It follows that the transfer of potential energy to kinetic energy is controlled entirely by the matrix $-PC^{-1}M$. Since it is diagonal, the entries are the

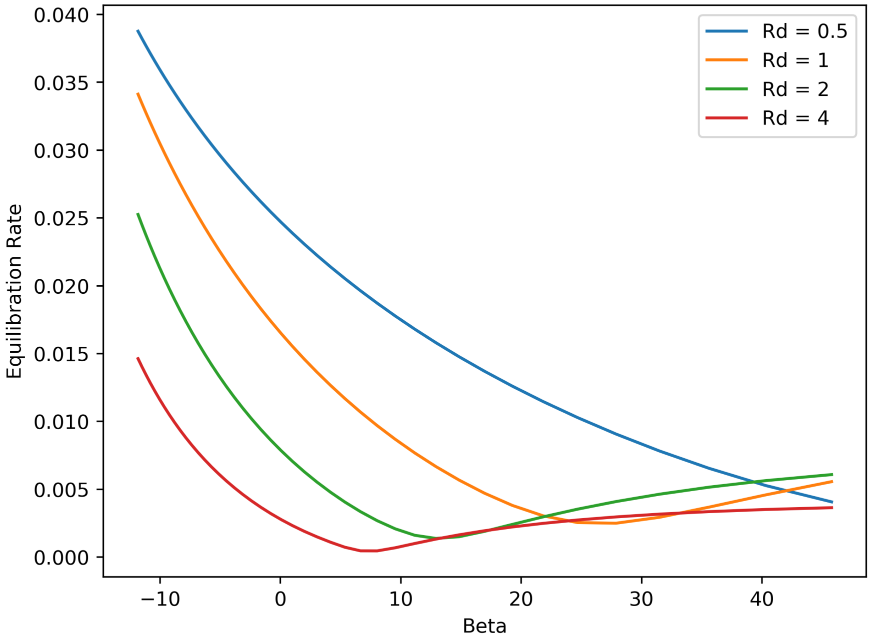

Figure 10.15: Predicted equilibration rate as a function of inverse temperature for several values of deformation radius. Similar to the single-layer case, the equilibration rate increases as β decrease showing that the closure predicts faster relaxation when the final state is more concentrated. As β increases we do see a decrease in relaxation rate to start. However, in contrast to the single-layer case, the equilibration rate increases after awhile. We see this behavior regardless of deformation radius.

eigenvalues and these give a transfer rate.

Figure 10.17 depicts the potential energy transfer rate as a function of β for $R_d = 1, 2$ and 4. Here we see that potential energy transfers more quickly as β approaches -8π and that the rise happens more quickly for a larger deformation radius. Just as the case with the equilibration, it appears that the rate approaches infinity in this limit–that is, the energy transfer becomes instantaneous. This is again an artifact of the fact that the equilibrium distribution approaches a point vortex as $\beta \to -8\pi$. In the other limit of $\beta \to \infty$, we see that the potential energy transfer rate drops to near zero with the drop happening faster with larger deformation radius. Zooming in on the interval of $\beta \in [10, 45]$ reveals a similar phenomena as with the equilibration: the curve reaches a maximum and then begins to drop again. However, unlike with the equilibration rate, there are signs that the concavity again changes and the potential energy transfer rate again begins to approach zero.

Figure 10.18 plots the available potential energy transfer rate dependence on R_d for

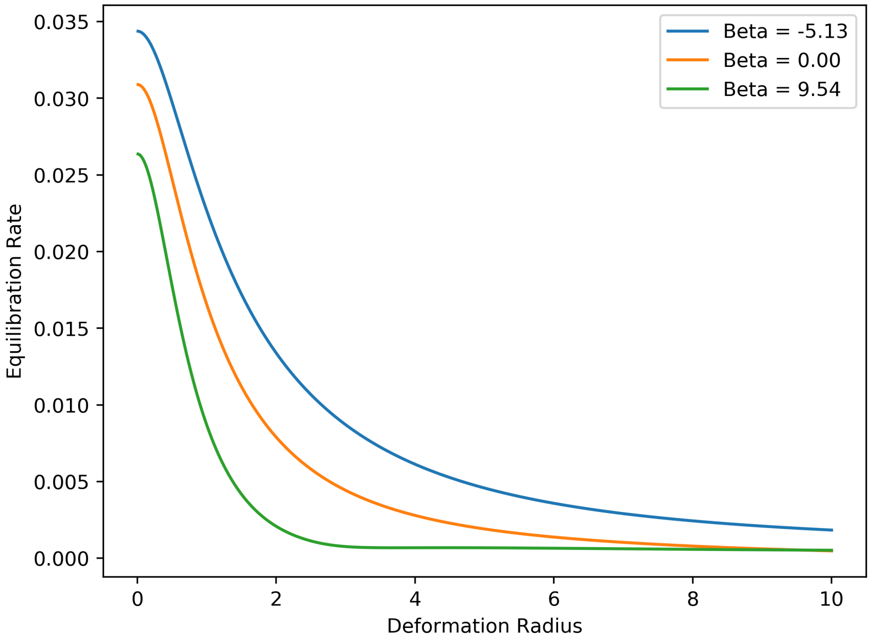

Figure 10.16: Predicted equilibration rate versus deformation radius for several values of inverse temperature. For any value of β, the relaxation rate decreases as the deformation rate increases and decays to zero as R_d goes to infinity. This is the result of the decreased interaction of the two layers as R_d increases and when $R_d = \infty$ the two layers are completely independent. As the deformation rate goes to zero, we recover the Euler equations so that the rates near zero correspond to those of the Euler equations.

several β values. The plot reveals a common “check mark” shape that each fixed β curve follows as the deformation radius increases. Of particular interest is that for any β value, the maximal rate of potential transfer occurs with deformation radius around 1.0. This is reminiscent of the conclusion of baroclinic instability: that the mode of maximum growth is roughly the same as the deformation radius. The variation due to β that we do see is that the deformation radius increases as β decreases. That is, as the vortex becomes more concentrated, we see an increase in the deformation radius that results in the fast transfer of available potential energy.

In light of the struggles of our model for larger deformation radii, this conclusion may be questioned. However, in all cases, the closure predicted faster equilibration and APE transfer than the EDNS result. Therefore, we would expect the eigenvalues of the appropriate matrix to be larger in magnitude than the true rates. It follows that the true curve should lay above our predicted curve (since the APE transfer rates are negative). Thus, the

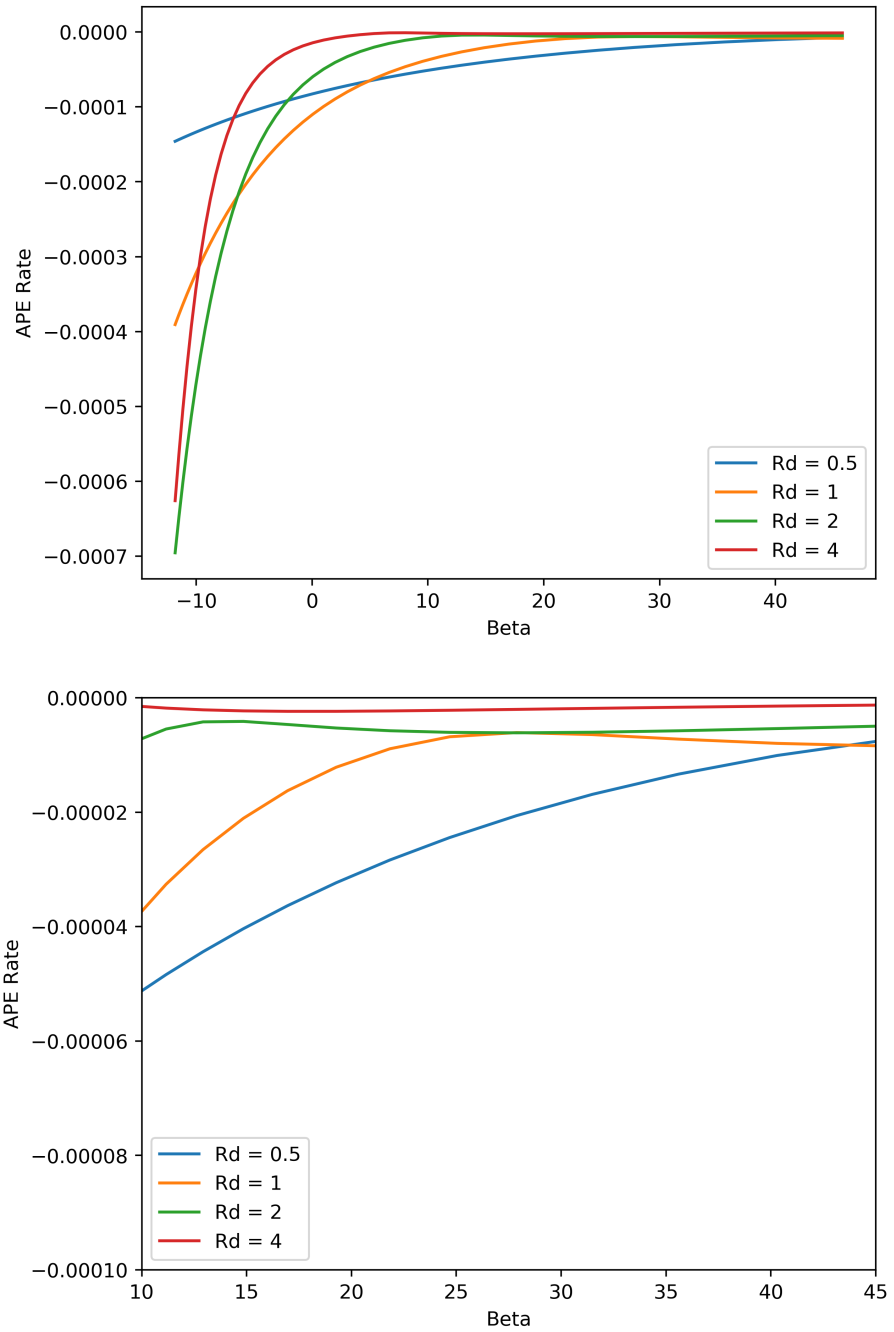

Figure 10.17: Predicted APE conversion rate as a function of inverse temperature for several values of the deformation radius. The lower plot is zoomed in on the interval [10,45]. The rate of transfer of APE increases as β decreases so that more concentrated equilibrium states transfer potential energy more quickly. As β increases, the energy transfer rate decreases until the difference due to deformation radius is negligible. Therefore, the more uniform distributions transfer energy more slowly and roughly independent of the deformation radius. The magnitude of the transfer rate increases after a certain minimal β value just as in figure 10.15.

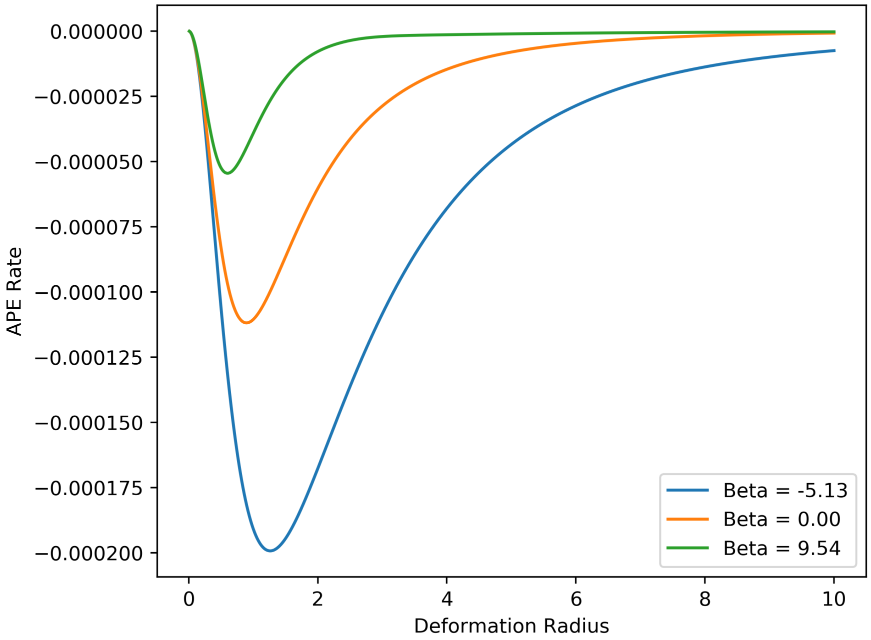

Figure 10.18: Predicted APE conversion rate as a function of deformation radius for several values of inverse temperature. Note the “check mark” shape common to each fixed β curve. The peak transfer rates all occur around $R_d = 1.0$ so that the deformation scale is roughly the same as the vorticity patch. There is an inverse relation between the two parameters. The smaller β values transfer energy more quickly at larger deformation radii and larger β values transfer energy more quickly at smaller deformation radii. The minima occur where our model has good predictive power.

check mark would be even more pronounced than in figure 10.18. Furthermore, as noted previously, the minimum occurs around $R_d = 1.0$ where our model performed well.

APPENDIX A

MEAN-FIELD CONVERGENCE OF STREAM FUNCTION

Here, we justify our replacement of the discrete stream function ψ_i^N with the continuum stream function ψ. This is done simply by making use of the fact that the distribution ζ^N converges weakly to some continuum distribution ζ. In particular, this means that for any continuous, bounded function f, we have

$$\int_{\mathbb{R}^2} f \cdot \zeta^N d\mathbf{x} \underset{N\to\infty}{\rightarrow} \int_{\mathbb{R}^2} f \cdot \zeta d\mathbf{x}.$$

First define the functions

$$\zeta_i^N(\mathbf{x}) = \sum_{j\neq i} \gamma \delta_{\mathbf{x}_j}, \tag{A.1}$$

$$\zeta^N(\mathbf{x}) = \sum_{i=1}^{N} \gamma \delta_{\mathbf{x}_j}. \tag{A.2}$$

From these definitions, we have

$$\begin{aligned}\int_{\mathbb{R}^2} \zeta_i^N f d\mathbf{x} &= \int_{\mathbb{R}^2} \zeta^N f d\mathbf{x} - \int_{\mathbb{R}^2} (\zeta^N - \zeta_i^N) f d\mathbf{x} \\ &= \int_{\mathbb{R}^2} \zeta^N f d\mathbf{x} - \gamma f(\mathbf{x}_i),\end{aligned}$$

from which we see that for any continuous and bounded function f

$$\int_{\mathbb{R}^2} \zeta_i^N f d\mathbf{x} \underset{N\to\infty}{\longrightarrow} \int_{\mathbb{R}^2} \zeta f d\mathbf{x}. \tag{A.3}$$

Therefore, ζ_i^N also converges weakly to ζ.

Now fix $\mathbf{x}_0 \in \mathbb{R}^2$. Let $g(\mathbf{x}, \mathbf{x}')$ be the appropriate Green's function to solve (2.4b). We leave this as a general function because the same arguments can be applied for (7.25b). In order to use our weak convergence argument, we need to approximate g with an appropriate continuous and bounded function. To eliminate the singularity at the origin and smooth g, we use a mollifier. Specifically, define

$$\phi(x) = \begin{cases} C \exp\left(\frac{1}{|\mathbf{x}|^2 - 1}\right), & |\mathbf{x}| < 1 \\ 0, & |x| \geq 1 \end{cases}$$

for the constant $C > 0$ such that $\int_{\mathbb{R}^2} \phi \, d\mathbf{x} = 1$. Then for any $\eta > 0$, let

$$\phi_\eta(x) = \frac{1}{\eta^2} \phi\left(\frac{\mathbf{x}}{\eta}\right).$$

We define g^η, the mollification of g, by

$$g^\eta = \phi_\eta * g,$$

where $*$ denotes the convolution product. From the properties of mollifiers (see [21] for a brief but thorough discussion), we know that g^η is infinitely smoothly differentiable and that $g^\eta \to g$ as $\eta \to 0$.

Define the mollified continuum stream function

$$\psi^\eta(\mathbf{x}) = \int_{\mathbb{R}^2} g^\eta(\mathbf{x}, \mathbf{x}')\zeta(\mathbf{x}')d\mathbf{x}'$$

and, similarly, the mollified point vortex stream function

$$\psi_i^{N,\eta}(\mathbf{x}) = \int_{\mathbb{R}^2} g^\eta(\mathbf{x}, \mathbf{x}')\zeta_i^N(\mathbf{x}')d\mathbf{x}'.$$

Fix η sufficiently small so that $|\psi^\eta(\mathbf{x}_0) - \psi(\mathbf{x}_0)| < 1/N$ and $|\psi_i^{N,\eta}(\mathbf{x}_0) - \psi_i^N(\mathbf{x}_0)| < 1/N$.

Since $|\psi^\eta(\mathbf{x}_0)| < \infty$ and $|\psi_i^{N,\eta}(\mathbf{x}_0)| < \infty$, there is $K_N \subset \mathbb{R}^2$ such that

$$\left|\psi^\eta(\mathbf{x}_0) - \int_{K_N} g^\eta(\mathbf{x}_0, \mathbf{x}')\zeta(\mathbf{x}')d\mathbf{x}'\right| < \frac{1}{N}, \tag{A.4}$$

$$\left|\psi_i^{N,\eta}(\mathbf{x}_0) - \int_{K_N} g^\eta(\mathbf{x}_0, \mathbf{x}')\zeta_i^N(\mathbf{x}')d\mathbf{x}'\right| < \frac{1}{N}. \tag{A.5}$$

Define $g^\eta_{K_N}$ to be the function given by $g^\eta_{K_N}(\mathbf{x}) = g^\eta(\mathbf{x}_0, \mathbf{x})$ for $\mathbf{x} \in K_N$ and $g^\eta_{K_N}(\mathbf{x}) = 0$ for any $\mathbf{x} \in \mathbb{R}^2$ such that $\text{dist}(\mathbf{x}, K_N) \geq 1/N$ and for $\mathbf{x}$ such that $\text{dist}(\mathbf{x}, K_N) < 1/N$, $g^\eta_{K_N}$ is continuous. Therefore $g^\eta_{K_N}$ is a continuous bounded function. It also follows that (A.4) and (A.5) are still satisfied with $g^\eta_{K_N}$ in place of g^η and $\mathbb{R}^2$ in place of K_N.

It follows that for any N, we have at $\mathbf{x}_0$

$$\begin{aligned}
|\psi_i^N - \psi| &\leq |\psi_i^N - \psi_i^{N,\eta}| + \left|\psi_i^{N,\eta} - \int_{\mathbb{R}^2} g^\eta_{K_N}\zeta_i^N d\mathbf{x}\right| + \left|\int_{\mathbb{R}^2} g^\eta_{K_N}(\zeta_i^N - \zeta)d\mathbf{x}\right| \\
&\quad + \left|\int_{\mathbb{R}^2} g^\eta_{K_N}\zeta d\mathbf{x} - \psi^\eta\right| + |\psi^\eta - \psi| \\
&\leq \frac{4}{N} + \int_{\mathbb{R}^2} g^\eta_{K_N}(\zeta_i^N - \zeta)d\mathbf{x}.
\end{aligned}$$

Letting $N \to \infty$ and using the weak convergence of ζ_i^N to ζ, we conclude that

$$\psi_i^N(\mathbf{x}_0) \to \psi(\mathbf{x}_0) \tag{A.6}$$

as desired.

APPENDIX B

DISCUSSION OF NUMERICAL METHODS

We believe in using previously implemented numerical algorithms (root finding, matrix solver, numerical integration, etc.) unless there is a compelling reason otherwise. Using these "black box" implementations has several benefits. The most obvious is saving considerable amounts of time. The other is that the commonly distributed versions of these algorithms have been used extensively so that users can have a high degree of confidence that the functions perform as advertised.

Hence, we have tried to use packaged algorithms for the large majority of the numerics in this work. As such, much of the following discussion briefly summarizes what is found in the documentation and the interested reader is encouraged to read the documentation (these almost always include references to books or papers that give the theoretical details of the particular algorithm).

The direct point vortex ensemble runs were written in C++ for speed purposes whereas the optimal closure was implemented using Python for ease and portability.

B.1 Direct Numerical Simulation of Point Vortex System

The desire for the direct numerics to run quickly was a compelling enough reason to implement the needed numerics for ourselves and to do so in C++. In doing so we can circumvent many of the safe programming practices that are needed when implementing algorithms for distribution. We also saved a significant amount of time by using a compiled language.

Of course, none of the methods used were exceptionally complicated. The right hand side of the point vortex equations (2.14) was done directly with no smoothing or cutoff distance.

This was largely dictated by ease of implementation. For the necessary computation of the modified Bessel function of the second kind for (7.34) and (9.23) we used the GNU Scientific Library. This is a free, publicly available numerical library for C and C++ programming. Information about the library and how to download it can be found at `https://www.gnu.org/software/gsl/`.

The actual time integration was done with the standard fourth order Runge-Kutta method (as was stated in the text) that can be found in any introductory numerical analysis textbook, [2] for example.

B.2 Time Integration of the Reduced Equations and the Ricatti Equation

Time integration for both the reduced equations resulting from the optimal closure and the Ricatti matrix differential equation was done using the Scipy (pronounced "Sigh Pie") module for Python. Documentation for this module is available at `https://docs.scipy.org/doc/scipy/reference/`.

The reduced equations were integrated using the class scipy.integrate.ode using the "vode" mode. This is a Python wrapper around the Fortran implemented function vode. The documentation for vode may be found at `https://computation.llnl.gov/casc/odepack/` as well as a downloadable copy (which includes more extensive documentation). This function solves nonstiff systems using Adams methods and stiff systems using backward differentiation formula methods and automatically switches between the two as needed.

The Ricatti equation was integrated using the function scipy.integrate.odeint function. This function is a Python wrapper around the function lsoda again from the Fortran library ODEPACK. Again, documentation and a downloadable copy is available at `https://computation.llnl.gov/casc/odepack/`. This function is very similar the function vode—it uses Adams methods for nonstiff systems, backward differentiation formula methods for stiff systems and switches between the two as needed.

The only reason for using different methods is that the Python implementations are not reentrant and we could not run two versions of the same solver simultaneously. As it was necessary to integrate the Ricatti equation through time to get the necessary M matrix for the integration of the reduced equations, we needed to run two solver at the same time.

B.3 Numerical Implementation of Whitaker-Turkington Algorithm

Implementation of the algorithm described in section 3.3 requires two components: a (nonlinear) root finder and a Poisson solver. Here we provide brief descriptions of the root finder and Poisson solver used in our implementation.

B.3.1 Root Finding

We relied on black box software for root finding. Specifically using the Scipy module function scipy.optimize.fsolve. This is a Python wrapper around the hybrd and hybrdj functions from the MINPACK library. The former is used when the Jacobian matrix must be approximated and the latter when the Jacobian is provided by the user. Documentation for the MINPACK library can be found at `http://www.mcs.anl.gov/~more/` and the source files can be downloaded at `http://www.netlib.org/minpack/`. Both functions use a modified version of the Powell hybrid method.

B.3.2 Poisson Solver

We needed a method to solve Poisson's equation in the plane

$$-\Delta\psi = \zeta$$

with the asymptotic boundary condition $\psi \sim -\log|\mathbf{x}|/2\pi$ as $|\mathbf{x}| \to \infty$. This boundary condition comes from the fact that a distribution of positive unit circulation looks like a point vortex with unit strength from far away.

As the vorticity distributions in our problem are smooth, a spectral method was the natural choice. For a traditional numerical analysis approach to spectral methods see [10]. For a more applied and implementation focused text see [6].

We chose to use the collocation or pseudospectral method as opposed to the Galerkin method. (Actually since we computed the integrals numerically, the two approaches are equivalent [6].) A particularly easy way to implement collocation spectral methods is to use differentiation matrices. The basic idea of differentiation matrices is to interpolate the solution in some appropriate (truncated) set of basis functions and then on a (finite) grid compute the derivatives of the basis functions exactly [53]. In this way, the differential operator is approximated by a matrix operator. In particular, let L be the differentiation matrix for the Laplacian. Then the solution of the above Poisson problem becomes the simple matrix-vector problem

$$-L\mathbf{p} = \mathbf{z},$$

where $\mathbf{p}$ and $\mathbf{z}$ are the grid point values of the functions ψ and ζ, respectively.

Because we sought the solution on the whole of $\mathbb{R}^2$, we used Hermite polynomials for the basis functions. To avoid interpolating between different grids, we used Gauss-Hermite quadrature to numerically evaluate all the necessary integrals. The MATLAB differentiation suite implemented by Weideman and Reddy [62] along with the Python port of the MATLAB code (which can be obtained at `https://github.com/labrosse/dmsuite`) formed the basis of our code.

Note that Hermite expansions require that the function decay to zero as we approach infinity which does not match our boundary condition. We solve this using the linearity of the problem. Let $\psi = \psi_D + \psi_G$ where $\psi_D \to 0$ as $|\mathbf{x}| \to \infty$ and $\psi_G \sim -\log|\mathbf{x}|/2\pi$. We build ψ_G and find the corresponding ζ_G by differentiation. Then $\zeta_D = \zeta - \zeta_G$ so that

$$-\Delta\psi_D = \zeta_D$$

where ζ_D is known and we can solve for ψ_D using a Hermite expansion and recover ψ and ψ is then recovered by using $\psi = \psi_D + \psi_G$.

BIBLIOGRAPHY

[1] Milton Abramowitz and Irene Stegun. *Handbook of Mathematical Functions with Formulas, Graphs, and Mathematical Tables.* Dover Publications, Inc., 1965. ISBN: 978-0-486-61272-0.

[2] Kendall Atkinson. *An Introduction to Numerical Analysis: Second Edition.* John Wiley & Sons, Inc., 1989. ISBN: 978-0471624899.

[3] Armando Babiano et al. "Vorticity and passive-scalar dynamics in two-dimensional turbulence". In: *Journal of Fluid Mechanics* 183 (1987), pp. 379–397. DOI: `10.1017/S0022112087002684`.

[4] G. K. Batchelor. "Computation of the Energy Spectrum in Homogeneous Two-Dimensional Turbulence." In: *Physics of Fluids (00319171)* 12.12 (1969), pp. II–233. ISSN: 00319171.

[5] Guido Boffetta and Robert E. Ecke. "Two-Dimensional Turbulence." In: *Annual Review of Fluid Mechanics* 44 (2012), p. 427. ISSN: 00664189.

[6] John P. Boyd. *Chebyshev and Fourier Spectral Methods, Second Edition (Revised).* Dover Books on Mathematics. Dover, 2001. ISBN: 978-0-486-41183-5.

[7] Haim Brezis. *Functional Analysis, Sobolev Spaces and Partial Differential Equations.* Universitext. Springer, 2011. ISBN: 978-0-387-70913-0.

[8] E. Caglioti et al. "A special class of stationary flows for two-dimensional Euler equations: a statistical mechanics description." In: *Communications in Mathematical Physics* 143.3 (1992), p. 501. ISSN: 14320916.

[9] E. Caglioti et al. "A special class of stationary flows for two-dimensional Euler equations: a statistical mechanics description. II." In: *Communications in Mathematical Physics* 174.2 (1995), p. 229. ISSN: 14320916.

[10] C. Canuto et al. *Spectral Methods: Fundamentals in Single Domains.* Scientific Computation. Springer, 2006. ISBN: 978-3-540-30725-9.

[11] George Casella and Roger L. Berger. *Statistical Inference: Second Edition.* Duxbury Resource Center, 2001. ISBN: 978-81-315-0394-2.

[12] J. G. Charney. "The dynamics of long waves in a baroclinic westerly current". In: *Journal of Meteorology* 4.5 (1947), pp. 135–162. DOI: `10.1175/1520-0469(1947)004<0136:TDOLWI>2.0.CO;2`.

[13] Pierre-Henri Chavanis. "From Jupiter's Great Red Spot to the Structure of Galaxies: Statistical Mechanics of Two-Dimensional Vortices and Stellar Systems". In: *Annals of the New York Academy of Sciences* 867.1 (1998), pp. 120–140. DOI: `10.1111/j.1749-6632.1998.tb11254.x`.

[14] Pierre-Henri Chavanis. "Kinetic theory of 2D point vortices from a BBGKY-like hierarchy". In: *Physica A: Statistical Mechanics and its Applications* 387.5 (2008), pp. 1123–1154. DOI: `https://doi.org/10.1016/j.physa.2007.10.022`.

[15] Alexandre J. Chorin. *Vorticity and Turbulence.* Applied Mathematical Sciences. Springer-Verlag, 1994. ISBN: 0-387-94197-5.

[16] Georges-Henri Cottet and Petros Koumoutsakos. *Vortex Methods: Theory and Practice.* Cambridge University Press, 2000. ISBN: 978-0-521-62186-1.

[17] Thomas M. Cover and Joy A. Thomas. *Elements of Information Theory: Second Edition.* John Wiley & Sons, Inc., 2006. ISBN: 978-0-471-24195-9.

[18] Mark T. DiBattista and Andrew J. Majda. "An Equilibrium Statistical Model for the Spreading Phase of Open-Ocean Convection". In: *Proceedings of the National Academy of Sciences of the United States of America* 11 (1999), p. 6009.

[19] Mark T. DiBattista and Andrew J. Majda. "Equilibrium Statistical Predictions for Baroclinic Vortices: The Role of Angular Momentum". In: *Theoretical and Computational Fluid Dynamics* 14 (5 2000), pp. 293–322. DOI: `https://doi.org/10.1007/s001620050142`.

[20] E. T. Eady. "Long Waves and Cyclone Waves". In: *Tellus* 1.3 (1949), pp. 33–52. ISSN: 2153-3490. DOI: `10.1111/j.2153-3490.1949.tb01265.x`.

[21] Lawrence C. Evans. *Partial Differential Equations, 2nd Edition.* Graduate Studies in Mathematics. American Mathematical Society, 2010. ISBN: 978-0-8218-4974-3.

[22] Konstantinos Gourgoulias et al. "How biased is your model? Concentration Inequalities, Information and Model Bias". In: (June 2017).

[23] V.M. Gryanik. "Dynamics of Singular Geostrophic Vortices in a Two-level Model of the Atomosphere (Ocean)." In: 19 (Mar. 1983), pp. 227–240.

[24] Karl E. Gustafson and James Albert Sethian. *Vortex Methods and Vortex Motion.* Society for Industrial and Applied Mathematics, 1991. ISBN: 978-1611-97173-6.

[25] N. G. Hogg and H. M. Stommel. "The Heton, an Elementary Interaction Between Discrete Baroclinic Geostrophic Vortices, and Its Implications Concerning Eddy Heat-Flow". In: *Proceedings of the Royal Society of London. Series A, Mathematical and Physical Sciences* 397.1812 (1985), pp. 1–20.

[26] Nelson G. Hogg and Henry M. Stommel. "Hetonic Explosions: The Breakup and Spread of Warm Pools as Explained by Baroclinic Point Vortices". In: *Journal of the Atmospheric Sciences* 42.14 (1985), pp. 1465–1476. DOI: `10.1175/1520-0469(1985)042<1465:HETBAS>2.0.CO;2`.

[27] Mark H. Holmes. *Introduction to Perturbation Methods: Second Edition.* Texts in Applied Mathematics. Springer, 2013. ISBN: 978-1-4614-5476-2.

[28] Mark H. Holmes. *Introduction to the Foundations of Applied Mathematics.* Texts in Applied Mathematics. Springer, 2009. ISBN: 978-0-387-87749-5.

[29] Michael K.-H. Kiessling. “Statistical mechanics of classical particles with logarithmic interactions”. In: *Communications on Pure and Applied Mathematics* 46.1 (1993), pp. 27–56. ISSN: 1097-0312. DOI: `10.1002/cpa.3160460103`.

[30] Richard Kleeman. “A Path Integral Formalism for Non-Equilibrium Hamiltonian Statistical Systems”. In: *Journal of Statistical Physics* 158.6 (2015), pp. 1271–1297. DOI: `10.1007/s10955-014-1149-x`.

[31] Richard Kleeman and Bruce E. Turkington. “A Nonequilibrium Statistical Model of Spectrally Truncated Burgers-Hopf Dynamics”. In: *Communications on Pure and Applied Mathematics* 67.12 (2014), pp. 1905–1946. ISSN: 1097-0312. DOI: `10.1002/cpa.21498`. URL: `http://dx.doi.org/10.1002/cpa.21498`.

[32] R.H. Kraichnan. “Inertial ranges transfer in two-dimensional turbulence”. In: *Physics of Fluids* 10.7 (1967), pp. 1417–1423. DOI: `10.1063/1.1762301`.

[33] Marcel Lesieur. *Turbulence in Fluids: Fourth Revised and Enlarged Edition.* Fluid Mechanics and its Applications: 84. Springer, 2008. ISBN: 9781402064357.

[34] Daniel Liberzon. *Calculus of Variations and Optimal Control Theory: A Concise Introduction.* Princeton University Press, 2012. ISBN: 978-0-691-15187-8.

[35] Ray Lischner. *C++ in a Nutshell: A Language and Library Reference.* O’Reilly Media, Inc., 2003. ISBN: 978-0-596-00298-5.

[36] T. S. Lundgren and Y. B. Pointin. “Statistical mechanics of two-dimensional vortices”. In: *Journal of Statistical Physics* 17.5 (Nov. 1977), pp. 323–355. DOI: `10.1007/BF01014402`.

[37] Carlo Marchioro and Mario Pulvirenti. *Mathematical Theory of Incompressible Nonviscous Fluids.* Applied Mathematical Sciences. Springer-Verlag, 1994. ISBN: 0-387-94044-8.

[38] Haralambos Marmanis. “The kinetic theory of point vortices”. In: *Proceedings of the Royal Society of London A: Mathematical, Physical and Engineering Sciences* 454.1970 (1998), pp. 587–606. DOI: `10.1098/rspa.1998.0175`.

[39] James C. McWilliams. “Statistical properties of decaying geostrophic turbulence”. In: *Journal of Fluid Mechanics* 198 (1989), pp. 199–230. DOI: `10.1017/S0022112089000108`.

[40] James C. Mcwilliams. “The emergence of isolated coherent vortices in turbulent flow”. In: *Journal of Fluid Mechanics* 146 (1984), pp. 21–43. DOI: `10.1017/S0022112084001750`.

[41] Robert Mecklenburg. *Managing Projects with GNU Make, 3rd Edition.* O'Reilly Media, Inc., 2005. ISBN: 978-0-596-00610-5.

[42] David Montgomery and Glenn Joyce. "Statistical mechanics of 'negative temperature' states." In: *Physics of Fluids* 17.6 (1974), p. 1139. ISSN: 00319171.

[43] Paul K. Newton. *The N-Vortex Problem: Analytical Techniques.* Applied Mathematical Sciences. Springer, 2001. ISBN: 0-387-95226-8.

[44] L. Onsager. "Statistical hydrodynamics". In: *Il Nuovo Cimento* 6 (Mar. 1949), pp. 279–287.

[45] Joseph Pedlosky. *Geophysical fluid dynamics: Second Edition.* Springer-Verlag, 1987. ISBN: 978-0387963877.

[46] Norman A. Phillips. "Energy Transformations and Meridional Circulations associated with simple Baroclinic Waves in a two-level, Quasi-geostrophic Model". In: *Tellus* 6.3 (1954), pp. 273–286. ISSN: 2153-3490. DOI: `10.1111/j.2153-3490.1954.tb01123.x`.

[47] Y. B. Pointin and T. S. Lundgren. "Statistical mechanics of two-dimensional vortices in a bounded container." In: *Physics of Fluids (00319171)* 19.10 (1976), p. 1459. ISSN: 00319171.

[48] Rick Salmon. *Lectures on Geophysical Fluid Dynamics.* Oxford University Press, 1998. ISBN: 0-19-510808-6.

[49] A. N. Shiryaev. *Probability: Second Edition.* Graduate Texts in Mathematics. Springer, 1996. ISBN: 978-0-387-94549-1.

[50] Patrick Tabeling. "Two-dimensional turbulence: a physicist approach." In: *Physics Reports* 362 (2002), pp. 1–62. ISSN: 0370-1573.

[51] Simon Thalabard and Bruce Turkington. "Optimal response to non-equilibrium disturbances under truncated Burgers-Hopf dynamics". In: *Journal of Physics A: Mathematical and Theoretical* 50.17 (2017), p. 175502. URL: `http://stacks.iop.org/1751-8121/50/i=17/a=175502`.

[52] Simon Thalabard and Bruce Turkington. "Optimal thermalization in a shell model of homogeneous turbulence". In: *Journal of Physics A: Mathematical and Theoretical* 49.16 (2016), p. 165502.

[53] L. Trefethen. *Spectral Methods in MATLAB.* Society for Industrial and Applied Mathematics, 2000. DOI: `10.1137/1.9780898719598`.

[54] Mark E. Tuckerman. *Statistical Mechanics: Theory and Molecular Simulation.* Oxford Graduate Texts. Oxford University Press, 2010. ISBN: 978-0198525264.

[55] Bruce Turkington. "An Optimization Principle for Deriving Nonequilibrium Statistical Models of Hamiltonian Dynamics". In: *Journal of Statistical Physics* 152 (2013), pp. 569–597. DOI: `10.1007/s10955-013-0778-9`.

[56] Bruce Turkington. “Statistical equilibrium measures and coherent states in two-dimensional turbulence”. In: *Communications on Pure and Applied Mathematics* 52.7 (1999), pp. 781–809. ISSN: 1097-0312.

[57] Bruce Turkington. “Statistical mechanics of two-dimensional and quasi-geostrophic flows”. In: *Long-Range Interacting Systems: Lecture Notes of the Les Houches Summer School* 90 (2008), pp. 159–210.

[58] Bruce Turkington, Qian-Yong Chen, and Simon Thalabard. “Coarse-graining two-dimensional turbulence via dynamical optimization”. In: *Nonlinearity* 29.10 (2016), p. 2961. URL: `http://stacks.iop.org/0951-7715/29/i=10/a=2961`.

[59] Bruce Turkington and Nathaniel Whitaker. “Statistical Equilibrium Computations of Coherent Structures in Turbulent Shear Layers”. In: *SIAM Journal on Scientific Computing* 17.6 (1996), pp. 1414–1433. DOI: `10.1137/S1064827593251708`.

[60] Geoffrey K. Vallis. *Atmospheric and Oceanic Fluid Dynamics: Fundamentals and Large-Scale Circulation*. Cambridge University Press, 2006. ISBN: 978-0521-84969-2.

[61] Larry Wasserman. *All of Statistics: A Concise Course in Statistical Inference*. Springer Publishing Company, Incorporated, 2010. ISBN: 9781441923226.

[62] J.A.C. Weideman and S.C. Reddy. In: *Transactions on Mathematical Software* 26.4 (2000), pp. 465–519.

[63] Nathaniel Whitaker and Bruce Turkington. “Maximum entropy states for rotating vortex patches”. In: *Physics of Fluids* 6 (12 1994), pp. 3963–3973. DOI: `10.1063/1.868386`.

[64] Robert Zwanzig. *Nonequilibrium Statistical Mechanics*. Oxford University Press, 2001. ISBN: 978-0195140187.